Generalized Dynamic Phasor-Based Simulation for Power Systems

by

Matthew Alexander Kulasza

A Thesis submitted to the Faculty of Graduate Studies of

The University of Manitoba

in partial fulfilment of the requirements of the degree of

MASTER OF SCIENCE

Department of Electrical and Computer Engineering

University of Manitoba

Winnipeg

Abstract

This thesis presents a new general purpose power system simulation technique based on dynamic phasors and conventional power system simulation methods. The method developed in this work converts time-domain circuits to equivalent dynamic phasor representations. These dynamic phasor equivalents are then simulated using nodal analysis and numerical integrator substitution. Simple linear circuit models are presented first in order to demonstrate that the new method is capable of accurately simulating small systems. The method developed in this work is then expanded to include control systems, power electronic converters, and synchronous machines. Visual comparisons with simulation results obtained using time-domain electromagnetic transient simulators demonstrate that the new dynamic phasor-based technique is capable of accurately simulating power system components.

To my family and friends

"A journey of a thousand miles begins with a single step"

— Lao Tzu

Acknowledgements

First and foremost, I would like to thank my advisor, Dr. Shaahin Filizadeh, for his guidance and support throughout this work and for entrusting me with laying the foundation for future work in this area. I would also like to thank my examining committee, Dr. Udaya Annakkage and Dr. David Gunderson, for taking the time to thoroughly read my thesis and offer helpful comments and insight.

I would like to thank my family for their constant support throughout this degree. My parents especially for always encouraging me and providing me with the tools I need to succeed. I would not have been able to manage graduate student life without their constant support, advice, and wisdom. My sister, who constantly reminds me how tough I need to be to face life's challenges, and my brother-in-law, who is always there to listen and offer a different perspective, also deserve a special thank you.

A special thank you goes to Kathryn Marcynuk, for encouraging me to pursue a graduate degree, listening to my frustrations and complaints, and celebrating all accomplishments, both big and small, with me. You inspire me everyday to reach higher and try harder, push me beyond my limits, and pick me up when I stumble. This work would certainly not exist without your patience and support.

I would also like to thank all of my friends as well, for being there to listen and help, even when I ignored them to work. In particular, I would like to thank Ian Deniset and Matthew McQuaker for believing in me and Steven Howell for sharing his own experiences as a graduate student as well as the insight that comes with those experiences.

This work was funded by the National Science and Engineering Research Council of Canada (NSERC) and the University of Manitoba.

Contents

List of Figures

List of Tables

List of Acronyms

EMT electromagnetic transient

FACTS flexible ac transmission systems

HVDC high voltage direct current

KCL Kirchoff's current law

KVL Kirchoff's voltage law

LCC line-commutated converter

NIS numerical integrator substitution

ODE ordinary differential equation

PI proportional-integral

PLL phase-locked loop

RMS root mean square

SSR subsynchronous resonance

SVC static VAR compensator

Chapter 1

Introduction

Power systems are large and complex systems with a wide variety of components that are continuous or discrete and linear or nonlinear. As a result, transient dynamics of power systems range in timescale from hundreds of nanoseconds to days [1]. Standard power system simulation techniques tend to be focused on a specific subset of transient dynamics. While this focus has lead to powerful simulation tools, it also restricts them to the timescales for which they were designed. Recent developments in power system modeling and simulation has given rise to new techniques that are capable of targeting the entire range of power system dynamics. The objective of this thesis is to develop a new general purpose simulation method based on these techniques, which is capable of simulating a wide range of power system dynamics.

1.1 Problem Definition

Figure 1.1 illustrates a general set of categories that represent different dynamics in the power system along with their approximate timescales [1]. Transients associated with the exchange of energy stored in electric and magnetic fields throughout the system are known as electromagnetic transients (EMTs). These types of transients are characterized by small timescales and high frequency content in the range of 50 Hz to 100 kHz. As a result, computer simulations of EMTs must be carried out using small time steps and highly detailed models. Therefore, simulation of EMTs is best suited to models of small subsystems and short time durations [2].

On the other end of the timescale spectrum shown in Figure 1.1 are electromechanical transients, which are associated with the exchange of energy stored in the electrical network and the rotating masses throughout the system [1]. These types of transients are characterized by large timescales and low frequency oscillations in the range of 1 Hz to 3 Hz [3]. Simulators designed for electromechanical transients ignore electrical network dynamics in order to reduce computational load and enable simulation of large systems for long durations [4]. However, this assumption also restricts electromagnetic transient simulators to low frequency phenomena.

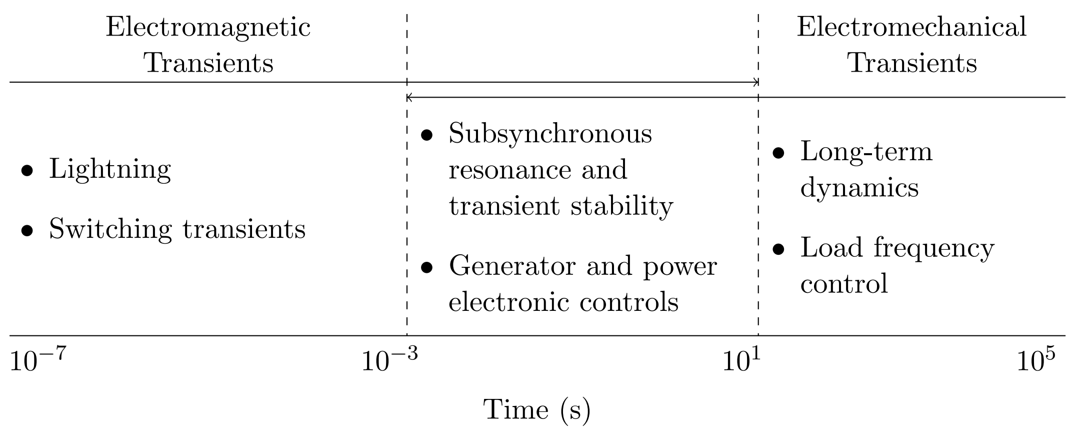

Figure 1.1: Timescale of transient dynamics in power systems

Simulators designed for EMTs and electromechanical transients are effective for handling their respective types of simulation. However, these subclasses do not effectively address the center of the timescale range, where the transient dynamics of a power system is a result of both its electrical network and mechanical subsystems. This portion of the dynamics spectrum is associated with phenomena such as subsynchronous resonance (SSR) and transient stability [1]. Furthermore, simulators designed for either EMTs or electromechanical transients are confined to the task for which they are designed. Therefore, it is not possible to use the same model to accomplish different simulation tasks.

The problem that this thesis will address is the lack of flexibility in conventional power system simulation techniques. This thesis will address this problem through the development of a new simulation technique based on dynamic phasors. Previous research has shown that dynamic phasors are highly flexible and are capable of targeting a wide range of power system dynamics. The following section will give a brief introduction to dynamic phasors, including its mathematical framework.

1.2 Dynamic Phasors

Phasor analysis involves representing sinusoidal quantities in steady state as complex numbers using only their magnitude and phase [5]. This type of analysis shifts the frequency spectra of the original system such that constant complex numbers represent real sinusoidal quantities [6]. Standard phasor analysis is used in conventional electromechanical transient simulators to represent the electrical network [4].

Dynamic phasors were introduced as a means of extending the bandwidth of electromechanical transient simulation to include the dynamics introduced by equipment such as power electronic converters [6, 7]. A dynamic phasor is simply a phasor where the magnitude and phase angle are allowed to change over time. This method allows electromechanical transient simulations to retain some of the dynamics associated with the electrical network without significantly increasing the computational load of the simulations. Previous work has demonstrated that dynamic phasors significantly improve the accuracy of electromechanical simulations involving power electronic converters [3].

The primary limitation of this dynamic phasors formulation is that the analysis is still limited to the base operating frequency of a power system. This dynamic phasors formulation does not provide any means of capturing the behaviour of higher order harmonics, which are defined in this work as all harmonics whose frequency is greater than the fundamental component. Harmonics are produced by nonlinear devices such as power electronic converters and saturating transformers. In a seemingly unrelated area of research, the generalized state space averaging method was introduced as a means of producing dynamic average value models of a wide variety of power electronic converters [8]. Generalized state space averaging accomplishes this by assuming that all quantities in a system model may be represented as a Fourier series with time-varying coefficients. However, examination of this method reveals that the Fourier coefficients are actually dynamic phasors themselves.

Except the dynamic phasors of this formulation are defined for the fundamental frequency as well as all of its harmonics. Therefore, models developed using generalized state space averaging may be used to simulate the entire range of dynamics shown in Figure 1.1, including the middle range between EMTs and electromechanical transients.

The main idea behind the generalized state space averaging method is that any arbitrary waveform, $x(t)$, may be approximated by a Fourier series with time-dependent coefficients [8]. The complete Fourier series of $x(t)$ is defined on the interval from $t - T_0$ to t by

$$x(t - T_0 + s) = \sum_{k=-\infty}^{\infty} \langle x \rangle_k (t) \, e^{jk\omega_0 (t - T_0 + s)}, \tag{1.1}$$

where ω_0 and T_0 are the base frequency and period of the series, respectively, and s is a parameter defined between 0 and T_0. The kth time-dependent Fourier coefficient in (1.1), $\langle x \rangle_k (t)$, is given by

$$\langle x \rangle_k (t) = \frac{1}{T_0} \int_0^{T_0} x(t - T_0 + s) \, e^{-jk\omega_0 (t - T_0 + s)} ds. \tag{1.2}$$

In practice, the series given by (1.1) must be truncated to a subset of harmonics, K, that includes all significant harmonics for a system model. The level of detail of a model may be adjusted by including or omitting harmonics, depending on the requirements of the model. Furthermore, only positive harmonics are required for systems that consist entirely of real-valued quantities.

Equation (1.2) demonstrates that for T_0-periodic functions, the time-dependent coefficients, $\langle x \rangle_k (t)$, reduce to the Fourier coefficients of $x(t)$. The time-dependent Fourier coefficients given by (1.2) are dynamic phasors, defined at the fundamental frequency and all of its harmonics. As this formulation serves as the basis for the remainder of this work, dynamic phasors from this point forward will strictly refer to the coefficients given by (1.2).

Figure 1.2 illustrates a graphical interpretation of the dynamic phasors method given by (1.1) and (1.2). The idea behind the dynamic phasors method is that the series uses a window of length T_0 to capture a portion of $x(t)$ [8]. The dynamic phasors of $x(t)$ are calculated based on the portion captured by the window. This window then slides across the waveform, calculating a new set of dynamic phasors at each point in time. Figure 1.2 illustrates this concept for the average value or dc component ($k = 0$) of the waveform.

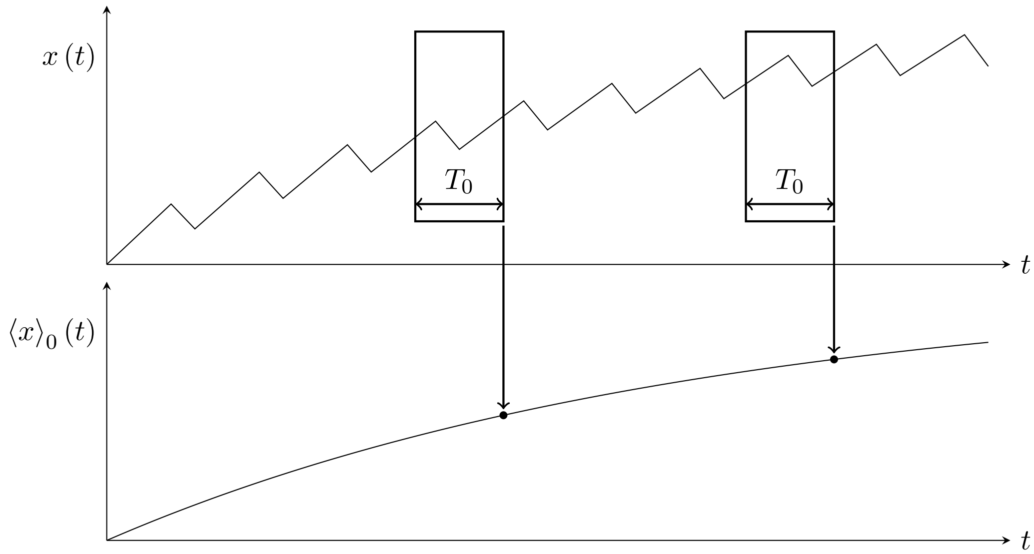

Figure 1.2: Visualization of the dynamic phasors method

The dynamic phasors method shown in Figure 1.2 is useful for situations where the waveform is known at every point in time. However, simulation is concerned with generating the waveforms for a system based on the inputs and characteristics of the elements contained in the system [7]. Instead, (1.2) may be viewed as the definition of an operator known as the dynamic phasor operator, $\langle \cdot \rangle_k$ [8]. This operator may then be applied to a set of time-domain equations, transforming them into a new set of equations in terms of dynamic phasors. Consider a set of nonlinear state equations given by

$$\frac{d\mathbf{x}}{dt} = \mathbf{f}\left(t, \mathbf{x}, \mathbf{u}\right), \tag{1.3}$$

where $\mathbf{x}(t)$ is an $n \times 1$ vector of state variables and $\mathbf{u}(t)$ is an $m \times 1$ vector of input variables. Applying the dynamic phasor operator to (1.3) yields the dynamic phasor form of the state equations, which is given by

$$\left\langle \frac{d\mathbf{x}}{dt} \right\rangle_k = \left\langle \mathbf{f}\left(t, \mathbf{x}, \mathbf{u}\right)\right\rangle_k . \tag{1.4}$$

The left hand side of (1.4) may be evaluated using the dynamic phasor differentiation property [8], which is given by

$$\left\langle \frac{dx}{dt} \right\rangle_k = \frac{d \langle x \rangle_k}{dt} + jk\omega_0 \langle x \rangle_k . \tag{1.5}$$

A general form for the right hand side of (1.4) does not exist as each individual system is different and requires special consideration. Furthermore, in general it is not possible to obtain a closed-form expression for the right hand side of (1.4) when the system is nonlinear [8]. Therefore, approximations are required to model nonlinear systems using dynamic phasors. An important exception is polynomial nonlinearities, where dynamic phasors may be obtained analytically using the convolution property given by

$$\langle xy \rangle_k = \sum_{l=-\infty}^{\infty} \langle x \rangle_{k-l} \langle y \rangle_l . \tag{1.6}$$

The final dynamic phasor form of (1.3) may be derived using (1.4) and (1.5) and is given by

$$\frac{d \langle \mathbf{x} \rangle_k}{dt} = -jk\omega_0 \langle \mathbf{x} \rangle_k (t) + \langle \mathbf{f} (t, \mathbf{x}, \mathbf{u}) \rangle_k . \tag{1.7}$$

This equation demonstrates that the dynamic phasor operator transforms a set of equations in terms of time-domain quantities into a new set of equations in terms of dynamic phasors [8]. Dynamic phasors have been used in a wide variety of areas to demonstrate their capabilities in power system design and simulations. Previous research in dynamic phasors has been primarily focused in the following areas:

1. **Power electronics** [8–14]: Modeling and simulation of power electronics has received a significant amount of attention in dynamic phasor research. The original generalized state space averaging method was introduced as a means of expanding the range of power electronic converters that could be modeled using average value techniques [8]. Generalized state space has been used to model dc/dc converters [9–11], resonant converters [8, 13], and dc/ac bridge topologies [11, 12]. An interesting application of dynamic phasors for modern power systems is in the area of microgrids [14]. Previous research has shown that dynamic phasors may be used to improve model accuracy and determine properties such as controller stability.

2. **HVDC and FACTS** [15–25]: High voltage direct current (HVDC) and flexible ac transmission systems (FACTS) have also received a significant amount of attention in dynamic phasor research. It has been shown that dynamic phasor models may be used for advanced applications, such as controller design focused on damping and removing instability in power systems [25].

3. **Machines** [26–30]: A particularly important area of research in dynamic phasors has been in the modeling of machines. Previous research has demonstrated that conventional machine modeling techniques may be enhanced using dynamic phasors [26, 28]. Dynamic phasors are capable of identifying the influence of harmonics and ac system imbalance and characterizing their impact on both electrical and mechanical quantities. Furthermore, machine models may be developed that incorporate effects of higher order harmonics using dynamic phasors.

4. **SSR and Hybrid simulation** [16, 22, 24, 31]: Previous research has demonstrated that dynamic phasors may be incorporated into electromechanical simulations to enhance the accuracy of power electronic models [24].

1.3 Thesis Motivation

The majority of previous research in dynamic phasors has been focused on illustrating its advantages and capabilities for specific subsystems. The state space models developed and used in literature are valuable for demonstrating properties of the researched systems. However, the programs used to simulate these models are also limited to the specific subsystems for which they were developed. Therefore, investigating new configurations requires either direct modification of program code or development of new programs.

Another major advantage of dynamic phasors that has not received much attention is the ability to select the level of detail in a system model by including or excluding harmonics [8, 27]. The majority of previous research has been focused on averaged or low frequency modeling using dynamic phasors. Previous research has demonstrated that dynamic phasors may be used in power electronic models to simulate the effects of higher order harmonics and obtain a more complete picture of the converter dynamics [8–10]. In some cases, additional harmonic detail is essential to ensure that simulations are accurate, particularly when parts of the system are dominated by harmonics. Furthermore, previous research has also demonstrated that higher order harmonics may be used to characterize component behaviour during adverse conditions [27, 28, 32].

General purpose simulation that includes higher order harmonics has been largely ignored in research. A state space-based general purpose simulator has been developed in literature [2]; however, this work primarily focused on the unification of EMT and electromechanical transient simulation. While some higher harmonic behaviour was included in specific models, the method developed did not include provisions for automatically including or excluding harmonics based on the level of detail required. General purpose discrete Norton equivalents that are based on the fundamental frequency form of dynamic phasors discussed in Section 1.2 have also been explored in research [33]. However, there is no possibility for inclusion of higher order harmonics as these models are based on the fundamental frequency dynamic phasors formulation.

The focus of this thesis is to present the development of a new general purpose simulation method based on dynamic phasors. The new method must be systematic and modular such that a wide variety of system configurations may be simulated using the same method and models. Furthermore, the new method must be capable of automatically adjusting the harmonics included in simulation such that a single model may be used to simulate both averaged behaviour and higher order harmonics.

1.4 Thesis Organization

This thesis presents a new general purpose simulation method using conventional power system simulation methods along with the dynamic phasors formulation discussed in Section 1.2. Background information on power system simulation and the methods used by general purpose EMT simulators is presented in Chapter 2.

A discussion of the general purpose simulation method developed in this work for dynamic phasor-based models is presented in Chapter 3. This chapter includes derivations of basic circuit models, such as capacitors and voltage sources, that form the building blocks for larger and more complex power system models.

The methods used in this work to simulate control and measurement systems is presented in Chapter 4. This chapter includes a discussion on the different modeling techniques available for control systems. The methods used to integrate control system models into the simulation method presented in Chapter 3 are also presented in this chapter.

Chapter 5 presents the line-commutated converter (LCC) model developed for use in the general purpose simulation method discussed in Chapter 3. This chapter includes a discussion on the methods used in literature to model power electronic converters. This chapter also includes a detailed derivation of the LCC model as an example of how power electronics may be included in the general purpose simulation method developed in this work.

The synchronous machine model developed for use in the dynamic phasor-based general purpose simulation method is presented in Chapter 6. This chapter includes a review of synchronous machine theory and the methods used in literature to model synchronous machines using dynamic phasors. This chapter also includes the derivation of a dynamic phasor-based synchronous machine model that is compatible with the general purpose simulation method developed in this work.

Conclusions and contributions of this work along with recommendations for future research are presented in Chapter 7.

Chapter 2

Electromagnetic Transient Simulation

Simulation of EMTs in power systems has historically been dominated by state space and nodal analysis-based algorithms [1]. The state space method is used extensively to represent and simulate physical systems. Prior to the introduction of the nodal analysis method, power system simulations were carried out primarily using state space-based algorithms. The popularity of the state space method in the area of dynamic phasors is evident from the wealth of literature and research available on the topic of generalized state space averaging.

The advantage of the state space method is that it naturally represents the dynamics of physical systems. The dynamics of an nth order physical system may be written as a set of n first order differential equations, known as state equations, each representing the dynamics of a variable, known as a state variable [1]. Furthermore, it is possible to represent a wide variety of nonlinearities and discrete elements using state space [2]. Finally, numerical methods for ordinary differential equations (ODEs) are defined in terms of first order differential equations [34]. Therefore, the state space method is particularly well suited to simulation of large systems with a wide variety of different elements such as power systems.

The primary drawback of the state space method for general purpose simulators is that formulation of the state equations is a complicated task. Automatic formulation of the state equations for a system model requires identification of the relationships between state variables and other quantities in the system [1]. This task is difficult to handle computationally and the result is additional complexity in computer software developed to carry out simulations using state space.

The second method uses nodal analysis in conjunction with a method known as numerical integrator substitution (NIS), which has become the most widely used method for EMT simulation in power systems [1]. This method forms the basis for world leading applications in EMT simulation, such as PSCAD/EMTDC, EMTP-RV, and RTDS. The nodal analysis-based approach to general purpose simulation is simple, systematic, and flexible. It is simple and systematic because it relies on a minimal amount of information regarding the system topology to formulate a set of discrete equations that can be used to simulate a power system model. The nodal analysis-based method is also flexible because the only requirement of discrete equivalents is that they must be represented as conductances and current sources.

The basic idea behind the nodal analysis method is that the discrete equivalent of a continuous model is formulated automatically based on the system topology. A set of nodal equations may then be developed from this discrete equivalent, which are used to solve for the network voltages in each time step. Figure 2.1 illustrates a simplified version of the nodal analysis simulation procedure [1]. The simulation procedure begins with an initialization of the system and network voltages. All of the current sources in the system are then updated at the beginning of the simulation loop using the network voltages from the previous time step. The network voltages are then obtained using the nodal equations developed from the discrete system equivalent. This procedure is repeated until the required simulation time has elapsed.

This chapter focuses on providing a brief introduction to the important concepts in power system simulation using the nodal analysis method. Section 2.1 provides background information on nodal analysis and how the network equations are developed. Section 2.2 discusses how the NIS method may be used to extend nodal analysis for simulation of more complex and dynamic circuits. Finally, Section 2.3 concludes the chapter with a discussion on the exponential method for numerical integration.

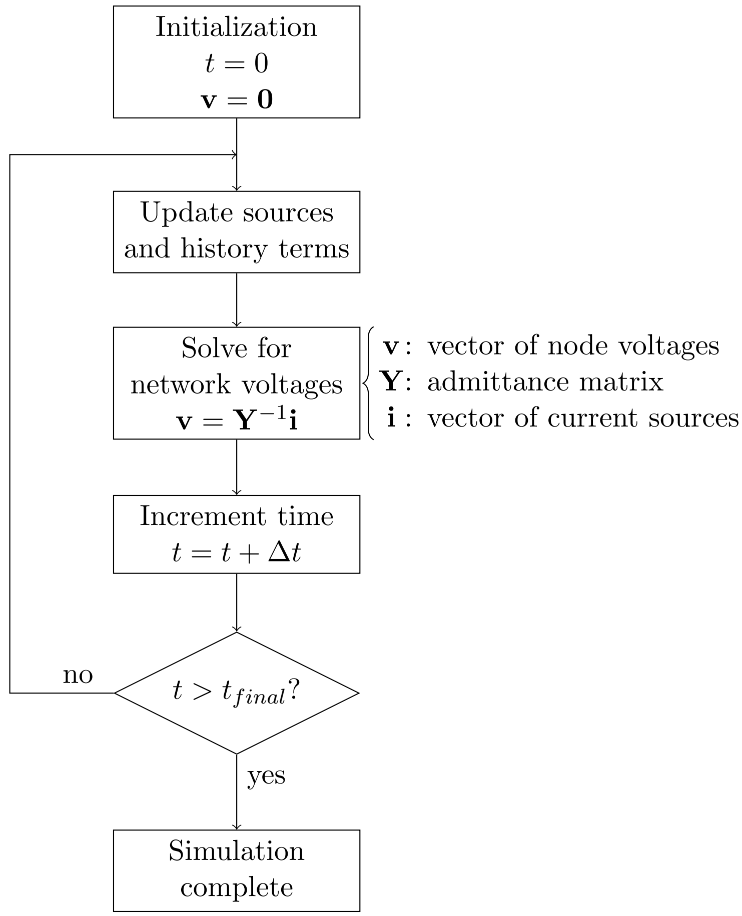

Figure 2.1: Nodal analysis simulation procedure

2.1 Nodal Analysis

Node-voltage or nodal analysis is a type of circuit analysis that uses Kirchoff's current law (KCL) to systematically develop a set of equations that may be used to obtain the solution for a given circuit [5]. The equations developed using this method are known as node-voltage or nodal equations and the unknown variables in these equations are the voltages at each node, which are known as node voltages. The node voltages are measured relative to a single node known as the reference node, which generally corresponds to the ground, i.e. zero voltage, in physical circuits.

Consider an arbitrary circuit with $N + 1$ nodes that consists solely of admittances and current sources. The solution of this circuit would require N KCL equations, since one equation is required for each node except the reference node [5]. Assuming that current is always leaving the present node under consideration, then the general form of the nodal equation at the ith node may be written as follows:

$$y_{i0}v_i + \sum_{\substack{j=1 \\ i\neq j}}^{N} y_{ij}\left(v_i - v_j\right) = I_i, \tag{2.1}$$

where node 0 is the reference node and the reference node voltage, v_0, is equal to zero [35]. The total admittance connecting node i to node j is represented by y_{ij} in (2.1). This term accounts for the net effect of all the branches connecting node i to node j and is equal to zero when there is no connection between the two nodes. The right hand side of (2.1) represents the net effect of all the current sources incident on node i, where positive values indicate current is injected into the node. The leading term in (2.1), y_{i0}, represents the admittance between node i and the reference node. Alternatively, (2.1) may be written in the form given by

$$Y_{ii}v_j + \sum_{\substack{j=1 \\ i\neq j}}^{N} Y_{ij}v_j = I_i, \tag{2.2}$$

where Y_{ii} and Y_{ij} are the self and mutual admittances, respectively [35] and are given by

$$Y_{ii} = \sum_{\substack{j=0 \\ i\neq j}}^{N} y_{ij}; \text{ and} \tag{2.3}$$

$$Y_{ij} = -y_{ij}. \tag{2.4}$$

Assembling the nodal equations from each node in a circuit into a single matrix equation yields:

$$\begin{bmatrix} Y_{11} & Y_{12} & \cdots & Y_{1N} \\ Y_{21} & Y_{22} & \cdots & Y_{2N} \\ \vdots & \vdots & \ddots & \vdots \\ Y_{N1} & Y_{N2} & \cdots & Y_{NN} \end{bmatrix} \begin{bmatrix} v_1 \\ v_2 \\ \vdots \\ v_N \end{bmatrix} = \begin{bmatrix} I_1 \\ I_2 \\ \vdots \\ I_N \end{bmatrix} \tag{2.5a}$$

$$\mathbf{Y}\mathbf{v} = \mathbf{i}, \tag{2.5b}$$

where $\mathbf{Y} = [y_{ij}]$ is known as the admittance matrix [35]. The diagonal elements of the admittance matrix are equal to the self admittance terms given by (2.3) and the off-diagonal elements are equal to the mutual admittance terms given by (2.4). The node voltages, $\mathbf{v}$, may be obtained by assembling the admittance matrix and current source vector, $\mathbf{i}$, based on the circuit topology and solving (2.5b).

The primary advantage of the nodal analysis method for circuit analysis is that assembly of the admittance matrix and source vector is systematic. The equations for the elements of the admittance matrix illustrate that they are calculated entirely based on the admittance and topology information of the circuit. Similarly, the elements of the current source vector are based entirely on the topology of the circuit and the parameters of each source in the circuit. Therefore, the nodal equations may be systematically developed by hand for small circuits or using computer algorithms for large networks based on a list of nodes and circuit elements.

2.2 Numerical Integrator Substitution

Nodal analysis is useful for analysis of circuits that consist solely of current sources and admittances. However, the nodal analysis method discussed in the previous section cannot directly handle elements that have differential or complex nonlinear relationships between the voltage and current. For example, simple linear elements, such as capacitors and inductors, or more complex nonlinear elements, such as saturating transformers, cannot be included in the admittance matrix or source vector in their original time-domain continuous form. Therefore, adjustments to the nodal analysis method are required in order to use it in the analysis of more complex and realistic networks.

The NIS method is used in many EMT simulators to convert continuous circuit models to discrete equivalents for simulation [1]. This method is based on numerical methods for solving ODEs, which is also known as numerical integration. Numerical integration methods are used to solve the majority of ODEs that arise from physical systems since they are generally complex and impossible to solve using analytical methods [34]. These methods involve converting continuous ODEs into discrete representations known as a difference equation [34]. The primary goal in numerical analysis of ODEs is to obtain difference equations that accurately capture the continuous behaviour of the modeled system [1].

There are a number of numerical integration methods that fall into distinct categories, and selection of an appropriate method involves consideration into the characteristics of the application. The NIS method for power system simulation was originally introduced using the trapezoidal integration method due to its accuracy, simplicity, and stability [36]. The stability of the trapezoidal method is particularly useful for general purpose simulation of any system because it is A-stable [34]. This property ensures that simulations of stable continuous systems carried out using the trapezoidal method will be numerically stable. The trapezoidal method for an arbitrary first order ODE of the form

$$\frac{dx}{dt} = f\left(t, x\right) \tag{2.6}$$

is defined by the following difference equation:

$$x\left[n\right] = x\left[n-1\right] + \frac{\Delta t}{2}\left(f\left(t_n, x\left[n\right]\right) + f\left(t_{n-1}, x\left[n-1\right]\right)\right), \tag{2.7}$$

where Δt is the time step, t_n is the time at the nth time step, and $x\left[n\right]$ is the discrete form of $x\left(t\right)$ shown in (2.6). Assuming that the initial conditions (t_0 and $x\left[0\right]$) of the system are known, the difference equation given by (2.7) may be solved at each time step using the information from the previous time step. This process is repeated until the simulation time, t_n, is greater than the desired duration, t_{final}.

The NIS method was originally developed to obtain discrete models for linear lumped elements with dynamic behaviour described by ODEs [36]. The main idea behind this method is that a numerical method such as the trapezoidal method may be applied to any element where the terminal voltage across and current through the device are related by an ODE to obtain a discrete difference equation. The difference equation may then be rearranged to reveal a discrete relationship between the voltage and current [1]. This relationship may be used to express the element as a discrete Norton equivalent, which can be used in conjunction with nodal analysis. As an example, consider an inductor, whose voltage and current are related through the following differential equation:

$$\frac{di_L}{dt} = \frac{1}{L} v_L. \tag{2.8}$$

Applying the trapezoidal method to (2.8) yields a difference equation for the inductor given by

$$i_L[n] = i_L[n-1] + \frac{\Delta t}{2L} \left(v_L[n] + v_L[n-1] \right). \tag{2.9}$$

The discrete Norton equivalent of the inductor may be obtained by rearranging the terms in (2.9) as follows:

$$i_L[n] = y_L v_L[n] + I_h[n-1], \tag{2.10}$$

where y_L and $I_h[n-1]$ are the discrete equivalent admittance and current source for the inductor, respectively, and are given by

$$y_L = \frac{\Delta t}{2L}; \text{ and} \tag{2.11}$$

$$I_h[n-1] = i_L[n-1] + y_L v_L[n-1]. \tag{2.12}$$

The current source in (2.10) is also known as the inductor's history current term [1]. This element represents the past information of the inductor and its influence on the present time step. Figure 2.2 illustrates the discrete Norton equivalent of the inductor. This example illustrates how the discrete equivalents produced by the NIS method may be used in circuit simulations. First of all, the discrete equivalent shown in Figure 2.2 is substituted into a continuous circuit in the place of each inductive element. The history current is updated at the beginning of each time step, using the network voltages obtained from the previous time step. The history current is then used in the present time step to obtain a new set of network voltages.

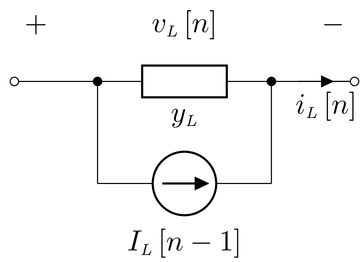

Figure 2.2: Discrete Norton equivalent of an inductor

2.3 Exponential Method for Numerical Integration

The previous section demonstrated how the trapezoidal method is used to convert continuous elements with dynamic behaviour into discrete elements that appear as Norton equivalents. The trapezoidal method is sufficient for many situations due to the properties discussed in Section 2.2. However, it has been shown that the difference equations that result from networks constructed using the trapezoidal method appear as a truncated Taylor series of the exponential function, e^x [37]. These truncated terms may result in numerical inaccuracies and oscillations, which are particularly noticeable when systems are simulated using large time steps.

The concept of using exponential integrator methods was first introduced in nodal analysis-based simulators for control systems and has been integrated into the control simulation models in programs such as PSCAD/EMTDC [1]. However, exponential methods are not limited to control system simulation and may be used to derive Norton equivalents using the NIS method discussed in the previous section [37]. Previous work has shown that the accuracy of power system simulation using the nodal analysis method may be improved if the difference equations for the network include complete exponential forms.

Exponential integrator methods have been used extensively in mathematics in order to solve specific forms of ODEs [38]. These methods are defined for nonlinear systems, and a wide range of different exponential integrator techniques may be obtained by considering different Taylor series approximations to the nonlinear system of equations. The method used in this work is restricted to linear systems and therefore, may be considered as a subset of the exponential integrator methods used in mathematics. Firstly, consider a linear nth order system whose state equations are given by

$$\frac{d\mathbf{x}}{dt} = \mathbf{Ax}\left(t\right) + \mathbf{Bu}\left(t\right), \tag{2.13}$$

where $\mathbf{x}$ is a $n \times 1$ vector of state variables, $\mathbf{u}$ is an $m \times 1$ vector of input variables, and $\mathbf{A}$ and $\mathbf{B}$ are $n \times n$ and $n \times m$ matrices of constants, respectively [39]. The general solution to (2.13) for $t \geq t_0$ is given by

$$\mathbf{x}\left(t\right) = e^{\mathbf{A}(t-t_0)}\mathbf{x}\left(t_0\right) + \int\limits_{t_0}^{t} e^{\mathbf{A}(t-\tau)}\mathbf{Bu}\left(\tau\right) d\tau, \tag{2.14}$$

where $\mathbf{x}\left(t_0\right)$ are the initial conditions of the system. This expression may be used to simulate the system given by (2.13) by setting the initial time, t_0, to $t - \Delta t$ as follows:

$$\mathbf{x}\left(t\right) = e^{\mathbf{A}\Delta t}\mathbf{x}\left(t - \Delta t\right) + \int\limits_{t-\Delta t}^{t} e^{\mathbf{A}(t-\tau)}\mathbf{Bu}\left(\tau\right) d\tau, \tag{2.15}$$

where $e^{\mathbf{A}\Delta t}$ may be calculated using a variety of methods, such as the scaling and squaring method [38].

The expression given by (2.15) requires further modification for the purposes of simulation as it includes an integral containing the input variables, which may be unknown quantities prior to the execution of simulations. The approach used in previous research is to assume a certain form of the input variables, which is based on their values at the present and previous time steps [40]. Based on previous research, the approach used in this work involves assuming that the input variables vary linearly between time steps. Under this assumption, the input variables in (2.15) may be written as follows:

$$\mathbf{u}\left(\zeta\right) = \frac{\mathbf{u}\left(t\right) - \mathbf{u}\left(t - \Delta t\right)}{\Delta t}\left(\zeta - t\right) + \mathbf{u}\left(t\right), \tag{2.16}$$

where ζ is defined between $t - \Delta t$ and t. Substituting (2.16) into (2.15) and solving yields the general form of the exponential integrator method used in this work, which is given by

$$\mathbf{x}(t) = e^{\mathbf{A}\Delta t}\mathbf{x}(t-\Delta t) + \mathbf{M}_0\mathbf{u}(t) + \mathbf{M}_1\mathbf{u}(t-\Delta t), \tag{2.17}$$

where $\mathbf{M}_0$ and $\mathbf{M}_1$ are the numerical integration coefficients and are given by

$$\mathbf{M}_0 = \frac{\mathbf{A}^{-2}}{\Delta t}\left(\mathbf{I} - e^{\mathbf{A}\Delta t} - \Delta t\mathbf{A}\right)\mathbf{B}; \text{ and} \tag{2.18}$$

$$\mathbf{M}_1 = \frac{\mathbf{A}^{-2}}{\Delta t}\left(e^{\mathbf{A}\Delta t}(\mathbf{I} + \Delta t\mathbf{A}) - \mathbf{I}\right)\mathbf{B}. \tag{2.19}$$

Alternatively, (2.17) may be written in terms of discrete quantities as follows:

$$\mathbf{x}[n] = e^{\mathbf{A}\Delta t}\mathbf{x}[n-1] + \mathbf{M}_0\mathbf{u}[n] + \mathbf{M}_1\mathbf{u}[n-1]. \tag{2.20}$$

The integration coefficients given by (2.18) and (2.19) indicate that $\mathbf{A}$ must be invertible to use the exponential method defined by (2.20). A special case for this method occurs when $\mathbf{A}$ is equal to the zero matrix, i.e. $\mathbf{A} = \mathbf{0}$. For example, the inductor from the previous section satisfies this condition. It can be shown that the exponential method derived in this section reduces to the trapezoidal method when $\mathbf{A} = \mathbf{0}$. Therefore, the exponential integrator method does not replace the trapezoidal method, but instead may be incorporated alongside the trapezoidal method to improve the nodal analysis method for certain subsystems of a large electrical system [37].

2.4 Summary

This chapter presented a brief introduction to the nodal analysis method used extensively to simulate EMTs in power systems. The primary advantages of the nodal analysis method for power system simulation is that it is simple, systematic, and flexible. This method is based on nodal analysis, which is a systematic technique for developing a system of equations that may be used to solve for the node voltages in a power system network. However, this method is limited to systems consisting of admittances and current sources.

The NIS method was introduced as a means of extending nodal analysis for the purposes of EMT simulation in power systems. This method uses numerical integration methods to convert continuous elements into discrete Norton equivalents. The NIS method was first introduced using the trapezoidal method due to its accuracy and stability. However, previous work has shown that systems simulated using the trapezoidal method may exhibit numerical inaccuracies and oscillations. Therefore, the exponential method was introduced to remove these numerical oscillations and improve the accuracy of simulations carried out using the nodal analysis method.

Chapter 3

Simulation Approach and Basic Circuits

The conventional dynamic phasors technique discussed in Section 1.2 is generally used in conjunction with state space representations. The dynamic phasor operator and associated properties are applied to the state equations for a given system to derive a set of differential equations in terms of dynamic phasors. This procedure is known as state space averaging [41] and is useful for dynamic phasor based modeling of independent subsystems. However, it is difficult to use this approach to develop a general purpose dynamic phasors-based simulation method as it relies on state equations. As discussed in Chapter 2, general purpose simulation using state space is a complex task as the state equations and relationships between different system variables must be identified. Furthermore, dynamic phasor-based simulation includes the additional complexity of identifying approximations to handle nonlinearities.

An alternative approach is to use a combination of the nodal analysis method discussed in Chapter 2 along with a modeling approach known as in-place circuit averaging [42]. Figure 3.1 illustrates the main idea behind the in-place circuit averaging approach for dynamic phasors. A circuit model in terms of time-domain quantities is shown on the left in Figure 3.1, which is converted directly to an equivalent dynamic phasor representation on the right. The time-domain quantities in the circuit, such as voltage and current, are replaced by their dynamic phasors and each element is replaced by its equivalent dynamic phasor model. Therefore, the in-place method differs from conventional methods as it operates on circuits models instead of state equations.

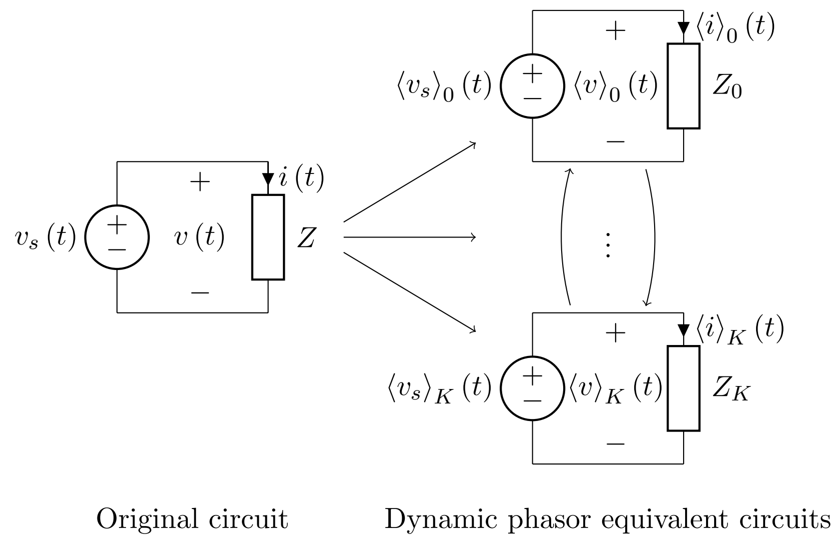

Figure 3.1: In-place circuit averaging using dynamic phasors

Nodal equations must be developed for the set of dynamic phasor equivalent circuits in order to simulate the circuit using the nodal analysis method. Figure 3.1 illustrates that the result of converting a circuit model using the in-place approach is K equivalent dynamic phasor circuits, where K is the number of harmonics included in the dynamic phasor simulations. These circuits may be coupled, depending on the presence of nonlinear devices such as power electronic converters [42]. A set of N nodal equations is required for each equivalent circuit to simulate a circuit with $N+1$ nodes. Therefore, the entire system requires $K \times N$ nodal equations for simulation. These equations may be written in block diagonal form as follows:

$$\begin{bmatrix} \mathbf{Y}_0 & \mathbf{C}_{01} & \cdots & \mathbf{C}_{0K} \\ \mathbf{C}_{10} & \mathbf{Y}_1 & \cdots & \mathbf{C}_{1K} \\ \vdots & \vdots & \ddots & \vdots \\ \mathbf{C}_{K0} & \mathbf{C}_{K1} & \cdots & \mathbf{Y}_K \end{bmatrix} \begin{bmatrix} \langle \mathbf{v} \rangle_0 \\ \langle \mathbf{v} \rangle_1 \\ \vdots \\ \langle \mathbf{v} \rangle_K \end{bmatrix} = \begin{bmatrix} \langle \mathbf{i} \rangle_0 \\ \langle \mathbf{i} \rangle_1 \\ \vdots \\ \langle \mathbf{i} \rangle_K \end{bmatrix}, \tag{3.1}$$

where $\langle \mathbf{v} \rangle_k$ and $\langle \mathbf{i} \rangle_k$ are the kth dynamic phasors of the node voltages and current sources respectively. The diagonal matrices, $\mathbf{Y}_k$, represent the admittance matrices for the individual dynamic phasor equivalent circuits, including the effects of any harmonic coupling present in the circuit. The off-diagonal matrices, $\mathbf{C}_{ij}$, represent the coupling terms between different harmonic equivalent circuits.

The entire set of nodal equations required to simulate a circuit using dynamic phasors illustrates that the computational burden is increased with each harmonic included in the simulations. This behaviour is not surprising since the computational burden of the generalized state space averaging method also increases as the number of harmonics increases. However, (3.1) also demonstrates that the system of nodal equations has properties that may be used to carry out simulations in an efficient manner. The coupling matrices in (3.1) will be zero if the system is completely decoupled. This situation occurs in linear systems and may also occur in discrete representations of nonlinear systems, depending on the methods used to model the nonlinear components. The equations will be in block diagonal form when the coupling matrices are zero. Therefore, each equivalent circuit may be solved independently in this situation. Furthermore, computational methods such as parallel processing may also be used when the harmonic equivalent circuits are decoupled.

As discussed in Section 2.2, all components must be converted to discrete Norton equivalents in order to use the nodal analysis method for simulations. This chapter focuses on developing discrete Norton equivalents for basic circuit components, which constitute the building blocks of larger and more complex circuits. Section 3.1 develops the discrete equivalents for resistors, capacitors, and inductors. Following this, Section 3.2 develops a method for modeling combinations of simple components. Finally, the Norton equivalents for voltage source models are discussed in Section 3.3.

3.1 Simple Components

Resistors, capacitors, and inductors are defined as simple components in this work. These basic elements form the building blocks for larger and more complex circuits [5], and can be used to approximate behaviour of complex systems such as transmission lines [35]. The relationship between voltage and current in these elements is simple and will be used to demonstrate the simulation procedure in detail. The discrete dynamic phasor equivalent models for the resistor, capacitor, and inductor are derived in Sections 3.1.1 to 3.1.3, respectively. This section concludes with a detailed example of a simple circuit in Section 3.1.4.

3.1.1 Resistors

Resistors are used in circuits to model components that consume energy [5]. For example, resistors are used in power systems to model active power loads and transmission line losses [35]. Figure 3.2 illustrates a resistor in terms of continuous time-domain quantities, where R is the resistance of the resistor. The current through and terminal voltage across a resistor are related as follows:

$$i_R\left(t\right) = \frac{v_R\left(t\right)}{R}. \tag{3.2}$$

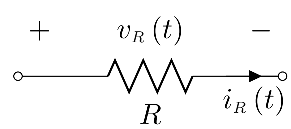

Figure 3.2: A resistor in terms of continuous time-domain quantities

The relationship between the resistor voltage and current dynamic phasors may be derived by applying the dynamic phasor operator to (3.2) and is given by

$$\left\langle i_R\right\rangle_k\left(t\right) = \frac{\left\langle v_R\right\rangle_k\left(t\right)}{R}. \tag{3.3}$$

The expression given by (3.3) shows that the dynamic phasor operator does not affect the relationship between voltage and current in a resistor. This result is expected since the relationship between voltage and current in a resistor is algebraic and the dynamic phasor operator is linear [42]. Figure 3.3 illustrates the resistor in terms of continuous dynamic phasors.

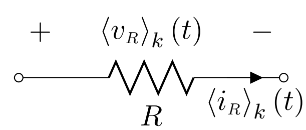

Figure 3.3: A resistor in terms of continuous dynamic phasors

The discrete relationship between the resistor voltage and current dynamic phasors may be obtained by substituting discrete quantities for continuous quantities in (3.3) as follows:

$$\begin{aligned} \langle i_R \rangle_k [n] &= \frac{\langle v_R \rangle_k [n]}{R} \\ &= G \langle v_R \rangle_k [n] , \end{aligned} \tag{3.4}$$

where G is the conductance of the resistor. Figure 3.4 illustrates the resistor in terms of discrete dynamic phasors.

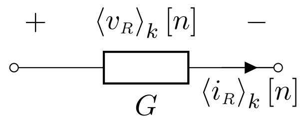

Figure 3.4: A resistor in terms of discrete dynamic phasors

3.1.2 Capacitors

Capacitors are used in circuits to model components in which energy is stored in an electric field and naturally arises when two charged components are separated by a medium [5]. For example, part of the interaction between a transmission line with another line or the ground may be modeled using a capacitor [35]. Figure 3.5 illustrates a capacitor in terms of continuous time-domain quantities, where C is the capacitance of the capacitor. The current through a capacitor is linearly related to the first derivative of the terminal voltage across the capacitor as follows:

$$i_C = C \frac{dv_C}{dt}. \tag{3.5}$$

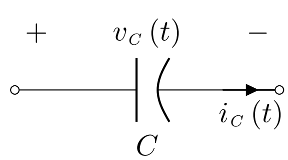

Figure 3.5: A capacitor in terms of continuous time-domain quantities

The relationship between the capacitor voltage and current dynamic phasors may be derived by applying the dynamic phasor operator and differentiation property to (3.5) [42] and is given by

$$\langle i_C \rangle_k (t) = C \frac{d \langle v_C \rangle_k}{dt} + jk\omega_0 C \langle v_C \rangle_k (t) . \tag{3.6}$$

The expression given by (3.6) implies that the capacitor appears as a capacitor in parallel with a susceptance to dynamic phasors, which is illustrated by Figure 3.6 [42]. The value of the parallel susceptance suggests that this branch appears as a short circuit as the harmonic, k, approaches infinity. This observation is consistent with circuit theory, as the impedance of capacitors approach zero as frequency approaches infinity [5]. Furthermore, the parallel branch in the dynamic phasor capacitor model disappears for the dc component as the susceptance of the parallel branch is zero when the harmonic is equal to zero. Therefore, the dynamic phasor operator does not affect the relationship between voltage and current in a capacitor for the dc component.

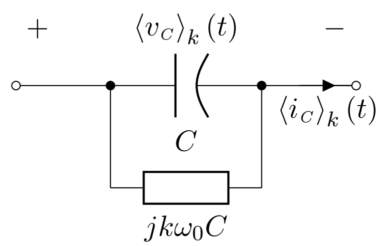

Figure 3.6: A capacitor in terms of continuous dynamic phasors

The relationship between the dynamic phasors of voltage and current in a capacitor given by (3.6) may be rewritten as follows:

$$\frac{d \langle v_C \rangle_k}{dt} = -jk\omega_0 \langle v_C \rangle_k (t) + \frac{\langle i_C \rangle_k (t)}{C}, \tag{3.7}$$

which is in the form of a first order linear state equation where

$$\mathbf{x} = \left[\langle v_C \rangle_k \right]; \quad \mathbf{u} = \left[\langle i_C \rangle_k \right]; \quad \mathbf{A} = \left[-jk\omega_0 \right]; \text{ and } \quad \mathbf{B} = \left[\tfrac{1}{C} \right].$$

Therefore, the exponential integrator method discussed in Section 2.3 may be used to derive a discrete dynamic phasor Norton equivalent for the capacitor. Applying the exponential integrator method to (3.7) yields the difference equation for the dynamic phasor form of the capacitor, which is given by

$$\langle v_C \rangle_k [n] = e^{-jk\omega_0 \Delta t} \langle v_C \rangle_k [n-1] + m_{0k} \langle i_C \rangle_k [n] + m_{1k} \langle i_C \rangle_k [n-1], \tag{3.8}$$

where

$$m_{0k} = \begin{cases} \dfrac{\Delta t}{2C} & k = 0 \\ \dfrac{1 - jk\omega_0 \Delta t - e^{-jk\omega_0 \Delta t}}{\Delta t C (k\omega_0)^2} & \text{otherwise; and} \end{cases} \tag{3.9}$$

$$m_{1k} = \begin{cases} \dfrac{\Delta t}{2C} & k = 0 \\ \dfrac{e^{-jk\omega_0 \Delta t} (1 + jk\omega_0 \Delta t) - 1}{\Delta t C (k\omega_0)^2} & \text{otherwise} \end{cases} \tag{3.10}$$

and Δt is the simulation time step. Rearranging the terms in (3.8) gives the discrete dynamic phasor Norton equivalent for the capacitor defined by

$$\langle i_C \rangle_k [n] = y_{Ck} \langle v_C \rangle_k [n] + I_{Ck} [n-1], \tag{3.11}$$

where y_{Ck} and $I_{Ck} [n-1]$ are the discrete admittance and history current for the capacitor, respectively, and are given by

$$y_{Ck} = \frac{1}{m_{0k}}; \text{ and} \tag{3.12}$$

$$I_{Ck} [n-1] = -\left(\frac{e^{-jk\omega_0 \Delta t}}{m_{0k}} \langle v_C \rangle_k [n-1] + \frac{m_{1k}}{m_{0k}} \langle i_C \rangle_k [n-1] \right). \tag{3.13}$$

Figure 3.7 illustrates the discrete Norton equivalent for the capacitor in terms of discrete dynamic phasors.

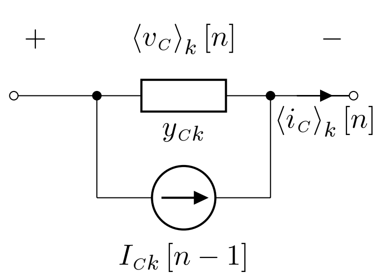

Figure 3.7: A capacitor in terms of discrete dynamic phasors

3.1.3 Inductors

Inductors are used in circuit models to represent components in which energy is stored in a magnetic field and naturally arises in current carrying conductors [5]. Inductors may be used to model the transformer windings and the armatures of electric machines [43]. Figure 3.8 illustrates an inductor in terms of continuous time-domain quantities, where L is the inductance of the inductor. The terminal voltage across an inductor is linearly related to the first derivative of the current through an inductor as follows:

$$v_L(t) = L\frac{di_L}{dt}. \tag{3.14}$$

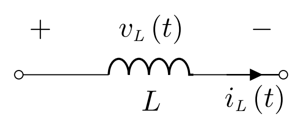

Figure 3.8: An inductor in terms of continuous time-domain quantities

The relationship between the inductor voltage and current dynamic phasors may be derived by applying the dynamic phasor operator and differentiation property to (3.14) [42] and is given by

$$\langle v_L \rangle_k(t) = L\frac{d\langle i_L \rangle_k}{dt} + jk\omega_0 L\langle i_L \rangle_k(t). \tag{3.15}$$

The relationship given by (3.15) implies that the inductor model appears as an inductor in series with a reactance to dynamic phasors, which is illustrated by Figure 3.9 [42]. The value of the series impedance suggests that the branch in series with the inductor appears as an open circuit as the harmonic, k, approaches infinity. This observation is consistent with circuit theory, as the impedance of inductors approach infinity as frequency approaches infinity [5]. Furthermore, the series impedance in the dynamic phasor inductor model disappears for the dc component as its impedance is zero when the harmonic is equal to zero. Therefore, the dynamic phasor operator does not affect the relationship between voltage and current in an inductor for the dc component.

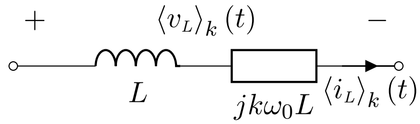

Figure 3.9: An inductor in terms of continuous dynamic phasors

The relationship between the dynamic phasors of voltage and current in an inductor given by (3.15) may be rewritten as follows:

$$\frac{d \langle i_L \rangle_k}{dt} = -jk\omega_0 \langle i_L \rangle_k (t) + \frac{\langle v_L \rangle_k (t)}{L}, \tag{3.16}$$

which is in the form of a first order state equation where

$$\mathbf{x} = \begin{bmatrix} \langle i_L \rangle_k \end{bmatrix}; \quad \mathbf{u} = \begin{bmatrix} \langle v_L \rangle_k \end{bmatrix}; \quad \mathbf{A} = \begin{bmatrix} -jk\omega_0 \end{bmatrix}; \text{ and } \quad \mathbf{B} = \begin{bmatrix} \frac{1}{L} \end{bmatrix}.$$

Therefore, the exponential integrator method discussed in Section 2.3 may be used to derive a discrete dynamic phasor Norton equivalent for the inductor. Applying the exponential integrator method to (3.16) yields the difference equation for the dynamic phasor form of the inductor, which is given by

$$\langle i_L \rangle_k [n] = e^{-jk\omega_0 \Delta t} \langle i_L \rangle_k [n-1] + m_{0k} \langle v_L \rangle_k [n] + m_{1k} \langle v_L \rangle_k [n-1], \tag{3.17}$$

where

$$m_{0k} = \begin{cases} \dfrac{\Delta t}{2L} & k = 0 \\ \dfrac{1 - jk\omega_0 \Delta t - e^{-jk\omega_0 \Delta t}}{\Delta t L \left(k\omega_0\right)^2} & \text{otherwise; and} \end{cases} \tag{3.18}$$

$$m_{1k} = \begin{cases} \dfrac{\Delta t}{2L} & k = 0 \\ \dfrac{e^{-jk\omega_0 \Delta t} \left(1 + jk\omega_0 \Delta t\right) - 1}{\Delta t L \left(k\omega_0\right)^2} & \text{otherwise} \end{cases} \tag{3.19}$$

and Δt is the simulation time step. Rearranging the terms in (3.17) gives the discrete dynamic phasor Norton equivalent for the inductor defined by

$$\langle i_L \rangle_k [n] = y_{Lk} \langle v_L \rangle_k [n] + I_{Lk} [n-1], \tag{3.20}$$

where y_{Lk} and $I_{Lk}[n-1]$ are the discrete admittance and history current for the inductor, respectively, which are given by

$$y_{Lk} = m_{0k}; \text{ and} \tag{3.21}$$

$$I_{Lk}[n-1] = m_{1k} \langle v_L \rangle_k [n-1] + e^{-jk\omega_0 \Delta t} \langle i_L \rangle_k [n-1]. \tag{3.22}$$

Figure 3.10 illustrates the discrete Norton equivalent for the inductor in terms of discrete dynamic phasors.

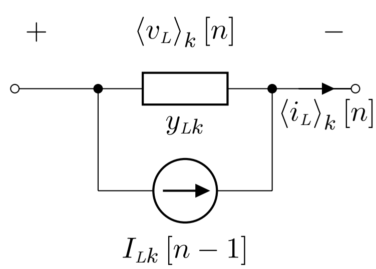

Figure 3.10: An inductor in terms of discrete dynamic phasors

3.1.4 Simulation Results

Figure 3.11 illustrates a simple circuit that will be used to demonstrate the method and models developed for simple passive components. The dynamics of the output voltage, $v_2(t)$, are described by the second order differential equation given by

$$\frac{R_s}{LC} i_s(t) = \frac{d^2 v_2}{dt^2} + \left(\frac{R_s}{L} + \frac{1}{RC} \right) \frac{dv_2}{dt} + \frac{R_s + R}{RLC} v_2(t). \tag{E3.1}$$

Figure 3.12 illustrates the equivalent dynamic phasor circuit for the kth harmonic, which may be derived by substituting the dynamic phasor equivalents defined in Sections 3.1.1 to 3.1.3 for each component in Figure 3.11.

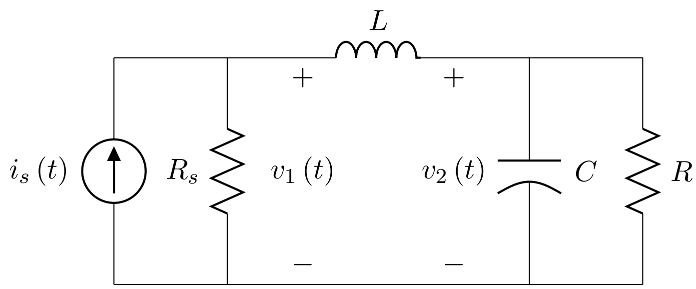

Figure 3.11: RLC example circuit in terms of continuous time-domain quantities

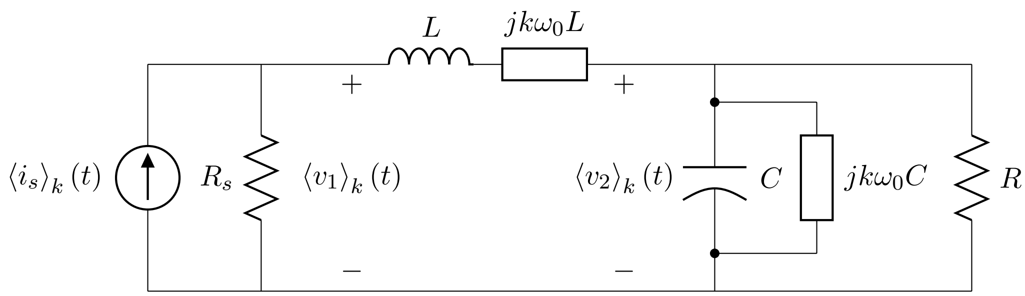

Figure 3.12: RLC example circuit in terms of continuous dynamic phasors

The dynamics of the kth output voltage dynamic phasor, $\langle v_2 \rangle_k (t)$, are described by the second order differential equation given by

$$\frac{R_s}{LC} \langle i_s \rangle_k (t) = \frac{d^2 \langle v_2 \rangle_k}{dt^2} + a_{1k} \frac{d \langle v_2 \rangle_k}{dt} + a_{2k} \langle v_2 \rangle_k (t) , \tag{E3.2}$$

where

$$a_{1k} = \frac{1}{RC} + \frac{R_s}{L} + j2k\omega_0; \text{ and} \tag{E3.3}$$

$$a_{2k} = \frac{R_s + R}{RLC} + jk\omega_0 \left(\frac{1}{RC} + \frac{R_s}{L} \right) + (jk\omega_0)^2 . \tag{E3.4}$$

The analytical solution for the output voltage dynamic phasors may be derived by solving (E3.2) and is given by

$$\langle v_2 \rangle_k (t) = \frac{R_s I_{sk}}{\lambda_{1k} \lambda_{2k} LC} \left(1 + \frac{\lambda_{2k} e^{\lambda_{1k} t} - \lambda_{1k} e^{\lambda_{2k} t}}{\lambda_{1k} - \lambda_{2k}} \right) \tag{E3.5}$$

assuming that the circuit parameters are chosen such that the eigenvalues, λ_{1k} and λ_{2k}, given by

$$\lambda_{1k}, \lambda_{2k} = -\frac{a_{1k}}{2} \pm \sqrt{\left(\frac{a_{1k}}{2}\right)^2 - a_{2k}} \tag{E3.6}$$

are distinct. Furthermore, (E3.5) was derived assuming that the current source dynamic phasors, $\langle i_s \rangle_k (t)$, are step functions of the form given by

$$\langle i_s \rangle_k (t) = \begin{cases} 0 & t < 0 \\ I_{sk} & t \geq 0, \end{cases} \tag{E3.7}$$

where I_{sk} is a real number for $k = 0$ and a complex number otherwise.

Figure 3.13 illustrates the discrete form of the example RLC circuit, which may be derived by substituting the discrete equivalents discussed in Sections 3.1.1 to 3.1.3 for each component in Figure 3.11.

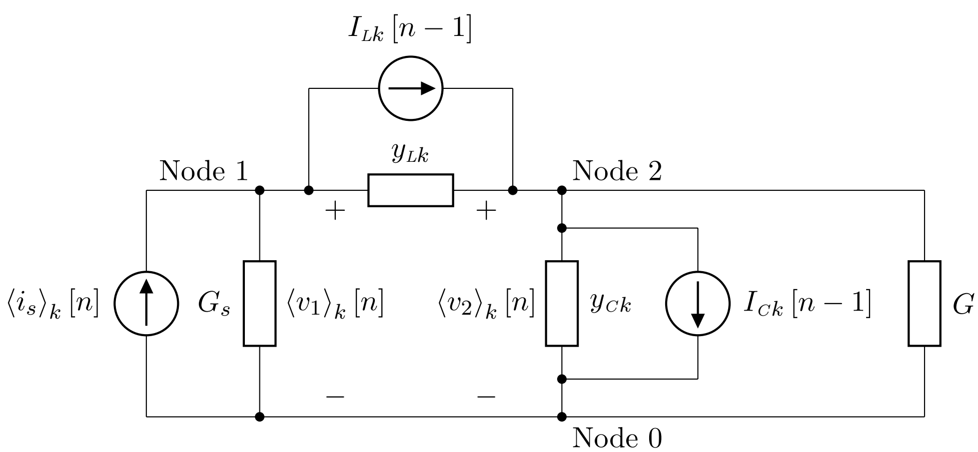

Figure 3.13: RLC example circuit in terms of discrete dynamic phasors

Figure 3.13 illustrates that there are two nodes (1 and 2) and one reference node (0) in the example circuit. Therefore, two nodal equations are required to simulate the example circuit, which are given by

$$(G_s + y_{Lk}) \langle v_1 \rangle_k - y_{Lk} \langle v_2 \rangle_k = \langle i_s \rangle_k - I_{Lk}; \text{ and} \tag{E3.8}$$

$$-y_{Lk} \langle v_1 \rangle_k + (G + y_{Ck} + y_{Lk}) \langle v_2 \rangle_k = I_{Lk} - I_{Ck}, \tag{E3.9}$$

where the discrete indexes (n and $n-1$) have been dropped from these equations for brevity and match those included in Figure 3.13. Alternatively, the nodal equations may be written in matrix format as follows:

$$\begin{bmatrix} G_s + y_{Lk} & -y_{Lk} \\ -y_{Lk} & G + y_{Ck} + y_{Lk} \end{bmatrix} \begin{bmatrix} \langle v_1 \rangle_k \\ \langle v_2 \rangle_k \end{bmatrix} = \begin{bmatrix} \langle i_s \rangle_k - I_{Lk} \\ I_{Lk} - I_{Ck} \end{bmatrix}. \tag{E3.10}$$

Simulations of the example RLC circuit were carried out using the dc ($k = 0$) and fundamental ($k = 1$) components to compare the simulated and analytical results. Assembling the nodal equations for both of these components into a single system yields:

$$\begin{bmatrix} G_s + y_{L0} & -y_{L0} & 0 & 0 \\ -y_{L0} & G + y_{C0} + y_{L0} & 0 & 0 \\ 0 & 0 & G_s + y_{L1} & -y_{L1} \\ 0 & 0 & -y_{L1} & G + y_{C1} + y_{L1} \end{bmatrix} \begin{bmatrix} \langle v_1 \rangle_0 \\ \langle v_2 \rangle_0 \\ \langle v_1 \rangle_1 \\ \langle v_2 \rangle_1 \end{bmatrix} = \begin{bmatrix} \langle i_s \rangle_0 - I_{L0} \\ I_{L0} - I_{C0} \\ \langle i_s \rangle_1 - I_{L1} \\ I_{L1} - I_{C1} \end{bmatrix}. \tag{E3.11}$$

The admittance matrix in (E3.11) shows that the two harmonics are completely decoupled, which is expected for a circuit comprised entirely of linear components. The component values and parameters used to obtain simulation results for the output voltage dynamic phasors are listed in Table 3.1. Furthermore, it is assumed that the all of the capacitor voltage and inductor current dynamic phasors were initially zero. Figures 3.14 and 3.15 illustrate the analytical and simulated output voltage waveforms for the dc and fundamental components respectively. The results show that the simulated quantities are in good agreement with the analytical waveforms.

Table 3.1: RLC example circuit simulation parameters

Parameter	**Value**
f_0	60 Hz
I_{s0}	10 A
I_{s1}	10 A
R_s	1 Ω
R	25 Ω
L	11.0 mH
C	0.11 mF

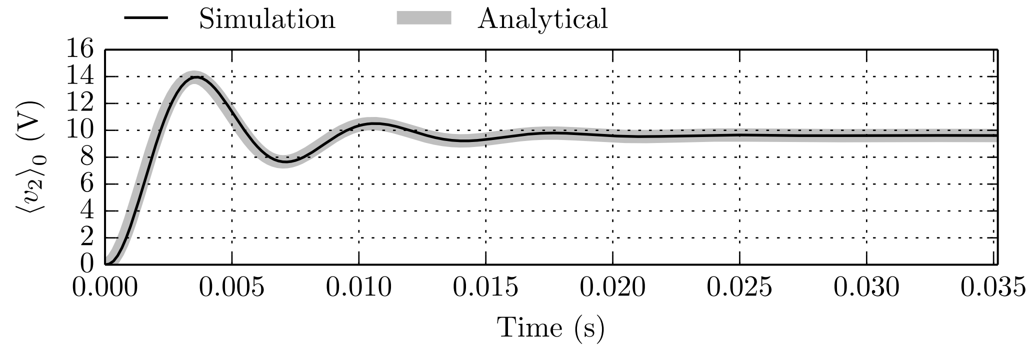

Figure 3.14: Comparison of the output voltage dynamic phasors for the dc component

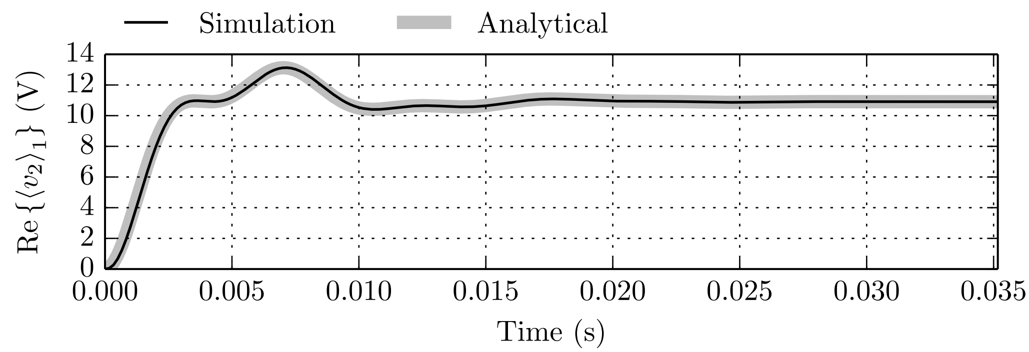

(a) Real

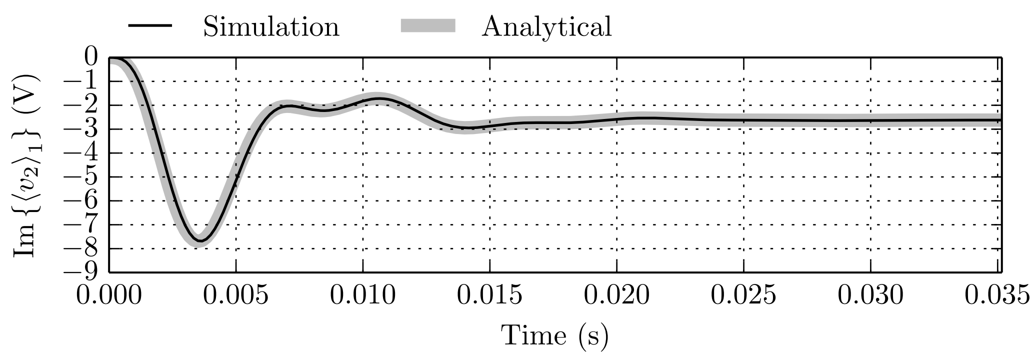

(b) Imaginary

Figure 3.15: Comparison of the output voltage dynamic phasors for the fundamental component

A valuable property of dynamic phasor-based simulation is that it is possible to use the simulation results to obtain an estimate of the frequency domain characteristics for continuous systems. This property can be used to investigate the frequency characteristics of a system and validate dynamic phasor models. Applying the Laplace transform to (E3.1) yields a transfer function that describes the relationship between the output voltage of the example circuit and the input current source, which is given by

$$T(s) = \frac{V_2(s)}{I_s(s)} = \frac{{}^{R_s}/_{LC}}{s^2 + \left({}^{R_s}/_{L} + {}^{1}/_{RC}\right)s + {}^{(R_s+R)}/_{RLC}}. \tag{E3.12}$$

An estimate of the transfer function given by (E3.12) may be obtained by simulating the example circuit using the step functions for $\langle i_s \rangle_k (t)$ given by (E3.7). Estimated values for (E3.12) may then be calculated using the following expression

$$T(jk\omega_0) \approx \frac{\langle v_2 \rangle_k}{I_s(k)}, \tag{E3.13}$$

where $\langle v_2 \rangle_k$ are the output voltage dynamic phasors after the circuit has reached steady state. Figure 3.16 illustrates the simulation results for first nine harmonics along with the continuous frequency response produced by (E3.12) with $s = j\omega$. These results show that the simulated values and the analytical response are in good agreement.

3.2 Composite Components

In the previous section, individual Norton equivalents were derived for the resistor, capacitor, and inductor. These equivalents are versatile and may be used in any configuration to simulate arbitrary circuits. However, certain combinations of the independent components are found more frequently than others. For example, a series RLC branch may be used as a filter and is found in a number of power system applications, including HVDC transmission systems and resonant converters [44]. These combinations may be grouped together to form composite components.

Grouping elements together into composite components offers a number of advantages to simulations carried out using the nodal analysis method. From a modeling perspective, composite element often has defining characteristics that only exist due to the combination of elements. It is often advantageous to model composite elements based on these characteristics rather than the component values of the simple elements. For example, a series tuned RLC filter may be specified by either the resistance, capacitance, and inductance of the individual components or, more frequently, the resonant frequency and bandwidth of the filter [45].

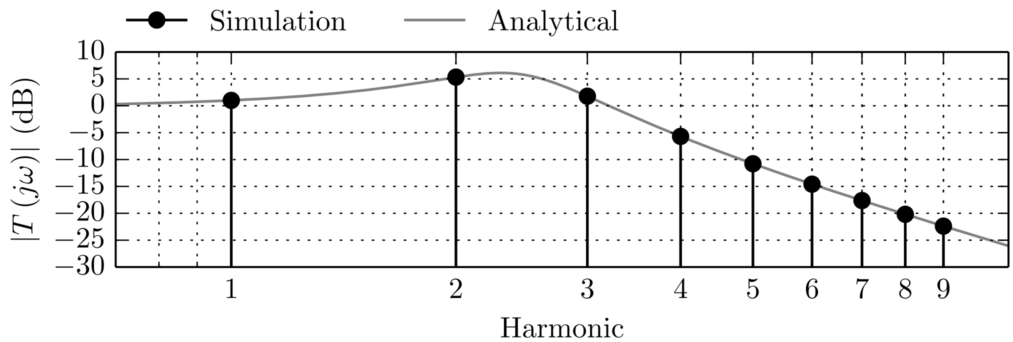

(a) Magnitude

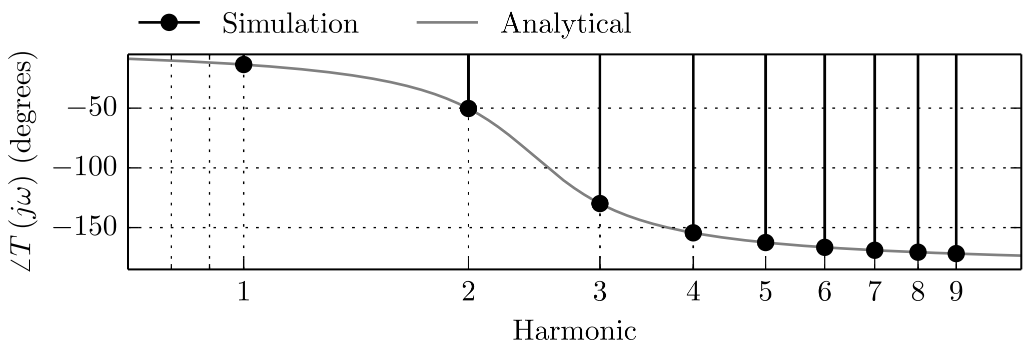

(b) Angle

Figure 3.16: Comparison of the analytical and estimated transfer functions

There are also computational advantages to using composite elements. Interior nodes are defined as the nodes that form the connection between the constituent elements in a composite component. Exterior nodes are defined as the nodes that are used to connect a composite component to an electrical network. Figure 3.17 illustrates a series RLC circuit in which its four nodes have been marked and numbered. In this circuit, nodes 2 and 3 are the interior nodes while nodes 1 and 4 are the exterior nodes.

Composite component models offer a computational advantage over individual component models because they remove all of the interior nodes from the system model. The total effect of a composite element is captured using a single Norton equivalent, which is connected to the system model using the exterior nodes. The interior node voltages may be obtained using mathematical relationships between constituent elements and exterior node voltages. For example, only nodes 1 and 4 in Figure 3.17 must be included in the node-voltage formulation when a composite component equivalent is used to simulate the series RLC circuit. However, all four nodes in the circuit must be included in the formulation when the series RLC circuit shown in Figure 3.17 is simulated using the individual equivalents derived in the Section 3.1.

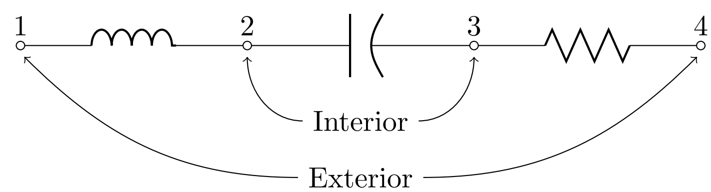

Figure 3.17: Series RLC circuit with interior and exterior nodes marked

The reduction in the number of nodes required for circuit simulation is a particularly important advantage for dynamic phasor-based simulation. As previously discussed, a dynamic phasor equivalent circuit must be included for each harmonic in the set selected for simulations. This property greatly increases the number of nodes and equations required to carry out the simulations. Therefore, a reduction in the number of nodes required for simulation offers significant benefits in terms of simulation speed for dynamic phasor-based simulation.

Composite components also improve the accuracy of simulations carried out using the nodal analysis method. The primary motivation for previous research into composite components in EMT simulation was to reduce the numerical inaccuracies and oscillations introduced by the trapezoidal method. Simulation accuracy may be improved using difference equations that are in exponential form since composite components often exhibit exponential transient behaviour [37]. Previous research has demonstrated that the accuracy of EMT simulations may be significantly improved using composite components, particularly for large values of the simulation time step.

The root matching method is a simple and systematic method for deriving Norton equivalents for composite components [37]. However, it lacks generality and must be repeated for each new circuit configuration. A new method was derived in this work using the exponential integrator method discussed in Section 2.3 that only requires a state space representation for each new composite component. Figure 3.18 illustrates a general composite component in terms of time-domain quantities. The first step in obtaining a generalized composite component Norton equivalent is to assume that the dynamics of any composite component may be represented as a set of linear state and output equations in the following form:

$$\frac{d\mathbf{x}}{dt} = \mathbf{A}\mathbf{x}\,(t) + \mathbf{B}v\,(t)\,; \text{ and} \tag{3.23}$$

$$i\,(t) = \mathbf{C}\mathbf{x}\,(t) + Dv\,(t)\,. \tag{3.24}$$

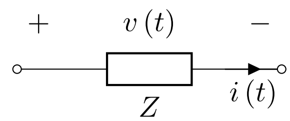

Figure 3.18: General form of a composite component in terms of time domain quantities

The most important aspect in the general equations given by (3.23) and (3.24) is that the terminal voltage across the composite component must be selected as the input variable and the current through the component must be selected as the output variable. The state and output equations given by (3.23) and (3.24) may be converted to dynamic phasors using the differentiation property as follows:

$$\frac{d\,\langle\mathbf{x}\rangle_k}{dt} = \mathbf{A}_k\,\langle\mathbf{x}\rangle_k\,(t) + \mathbf{B}\,\langle v\rangle_k\,(t)\,; \text{ and} \tag{3.25}$$

$$\langle i\rangle_k\,(t) = \mathbf{C}\,\langle\mathbf{x}\rangle_k\,(t) + D\,\langle v\rangle_k\,(t)\,, \tag{3.26}$$

where

$$\mathbf{A}_k = \mathbf{A} - jk\omega_0\mathbf{I}. \tag{3.27}$$

The discrete form of the state and output equations may be derived using the exponential integrator discussed in Section 2.2, which are given by

$$\langle\mathbf{x}\rangle_k\,[n] = e^{\mathbf{A}_k\Delta t}\,\langle\mathbf{x}\rangle_k\,[n-1] + \mathbf{M}_{0k}\,\langle v\rangle_k\,[n] + \mathbf{M}_{1k}\,\langle v\rangle_k\,[n-1]\,; \text{ and} \tag{3.28}$$

$$\langle i\rangle_k\,[n] = \mathbf{C}\,\langle\mathbf{x}\rangle_k\,[n] + D\,\langle v\rangle_k\,[n]\,, \tag{3.29}$$

where

$$\mathbf{M}_{0k} = \begin{cases} \dfrac{\Delta t \mathbf{B}}{2} & \text{if } \mathbf{A}_k = \mathbf{0} \\ \dfrac{\mathbf{A}_k^{-2}}{\Delta t}\left(e^{\mathbf{A}_k \Delta t} - \mathbf{A}_k \Delta t - \mathbf{I}\right)\mathbf{B} & \text{otherwise; and} \end{cases} \tag{3.30}$$

$$\mathbf{M}_{1k} = \begin{cases} \dfrac{\Delta t \mathbf{B}}{2} & \text{if } \mathbf{A}_k = \mathbf{0} \\ \dfrac{\mathbf{A}_k^{-2}}{\Delta t}\left(\mathbf{I} - \left(\mathbf{I} - \mathbf{A}_k \Delta t\right) e^{\mathbf{A}_k \Delta t}\right)\mathbf{B} & \text{otherwise.} \end{cases} \tag{3.31}$$

The general Norton equivalent for composite components may be derived by substituting (3.28) into (3.29), which is given by

$$\langle i \rangle_k [n] = y_k \langle v \rangle_k [n] + I_k [n-1], \tag{3.32}$$

where y_k and $I_k [n-1]$ are the discrete admittance and history current for the generic composite component, respectively, which are given by

$$y_k = \mathbf{C}\mathbf{M}_{0k} + D; \text{ and} \tag{3.33}$$

$$I_k [n-1] = \mathbf{C} e^{\mathbf{A}_k \Delta t} \langle \mathbf{x} \rangle_k [n-1] + \mathbf{C}\mathbf{M}_{1k} \langle v \rangle_k [n-1]. \tag{3.34}$$

3.2.1 Simulation Results

The RLC example circuit used in Section 3.1.4 will be used in this section to demonstrate how composite components are constructed and incorporated into the general purpose simulation method developed in this work. Figure 3.19 illustrates the load portion of the RLC example circuit, which may be represented in terms of the state and output equations given by

$$\frac{di_L}{dt} = \frac{v - v_C}{L}; \tag{E3.14}$$

$$\frac{dv_C}{dt} = \frac{i_L}{C} - \frac{v_C}{RC}; \text{ and} \tag{E3.15}$$

$$i = i_L. \tag{E3.16}$$

The state and output equations given by (E3.14) to (E3.16) may be written as a set of matrix equations of the form given by (3.23) and (3.24) where

$$\mathbf{x} = \begin{bmatrix} i_L \\ v_C \end{bmatrix}; \quad \mathbf{A} = \begin{bmatrix} 0 & -\frac{1}{L} \\ \frac{1}{C} & -\frac{1}{RC} \end{bmatrix}; \quad \mathbf{B} = \begin{bmatrix} \frac{1}{L} \\ 0 \end{bmatrix}; \quad \mathbf{C} = \begin{bmatrix} 1 & 0 \end{bmatrix}; \text{ and } \quad D = 0.$$

These equations are sufficient for generating a discrete dynamic phasor Norton equivalent for the circuit illustrated by Figure 3.19. Figure 3.20 illustrates the discrete equivalent model of the example RLC circuit, in which the load is modeled using a single discrete Norton equivalent with parameters defined by (3.33) and (3.34).

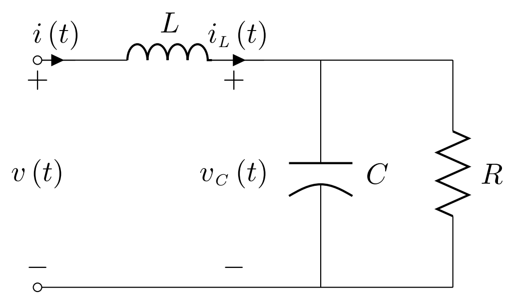

Figure 3.19: RLC load circuit in terms of continuous time-domain quantities

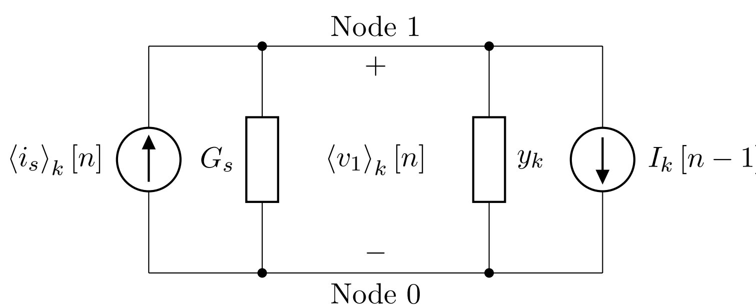

Figure 3.20: RLC example circuit in terms of discrete dynamic phasors and a composite component load model

Figure 3.20 illustrates that there is one node (1) and one reference node (0) in this discrete equivalent form of the example RLC circuit. Therefore, one nodal equation for each harmonic is required to simulate this circuit, which is given by

$$(G_s + y_k) \langle v_1 \rangle_k [n] = \langle i_s \rangle_k [n] - I_k [n-1]. \tag{E3.17}$$

An additional equation is required to obtain the output voltage dynamic phasors,

$\langle v_2 \rangle_k [n]$, since they are embedded within the composite component equivalent. The output voltage dynamic phasors are given in terms of the composite component states as follows:

$$\langle v_2 \rangle_k [n] = \langle v_C \rangle_k [n], \tag{E3.18}$$

where $\langle v_C \rangle_k [n]$ are the dynamic phasors of the capacitor voltage. Simulations were carried out for the dc ($k = 0$) and fundamental ($k = 1$) components using the initial conditions and parameters listed in Section 3.1.4. Figures 3.21 and 3.22 illustrates the simulated and analytical output voltage waveforms for the dc and fundamental components respectively. The results show that the simulated and analytical waveforms are in good agreement.

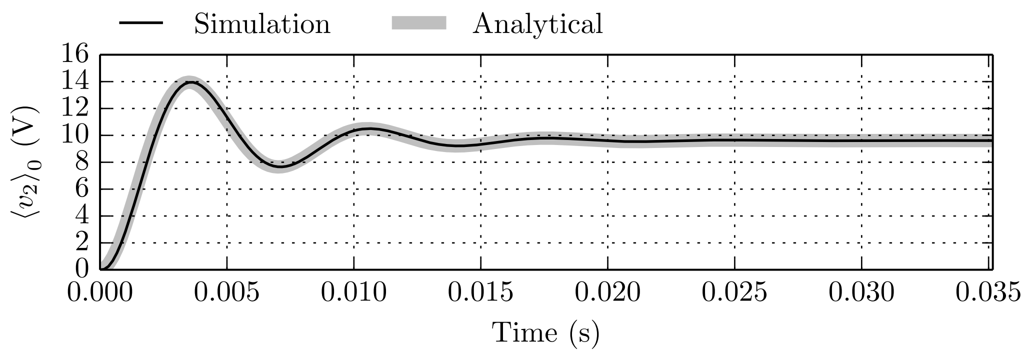

Figure 3.21: Comparison of the output voltage dynamic phasors for the dc component

3.3 Voltage Sources

Figure 3.23 illustrates the general form of a voltage source where an ideal source, $v_s(t)$, is connected to an electrical network through an impedance, Z_s. In general, the ideal voltage source is either a periodic ac source or a dc source in power system models. For example, a sinusoidal source may be used to model the ac system in an HVDC transmission system model while a square wave source may be used to represent the input in a resonant converter model [44]. The impedance block in Figure 3.23 is a placeholder representing any passive elements that are used to model the impedance of the source. For example, a resistor in series with an inductor may be used to represent the equivalent impedance of the ac system in an HVDC transmission system model [4].

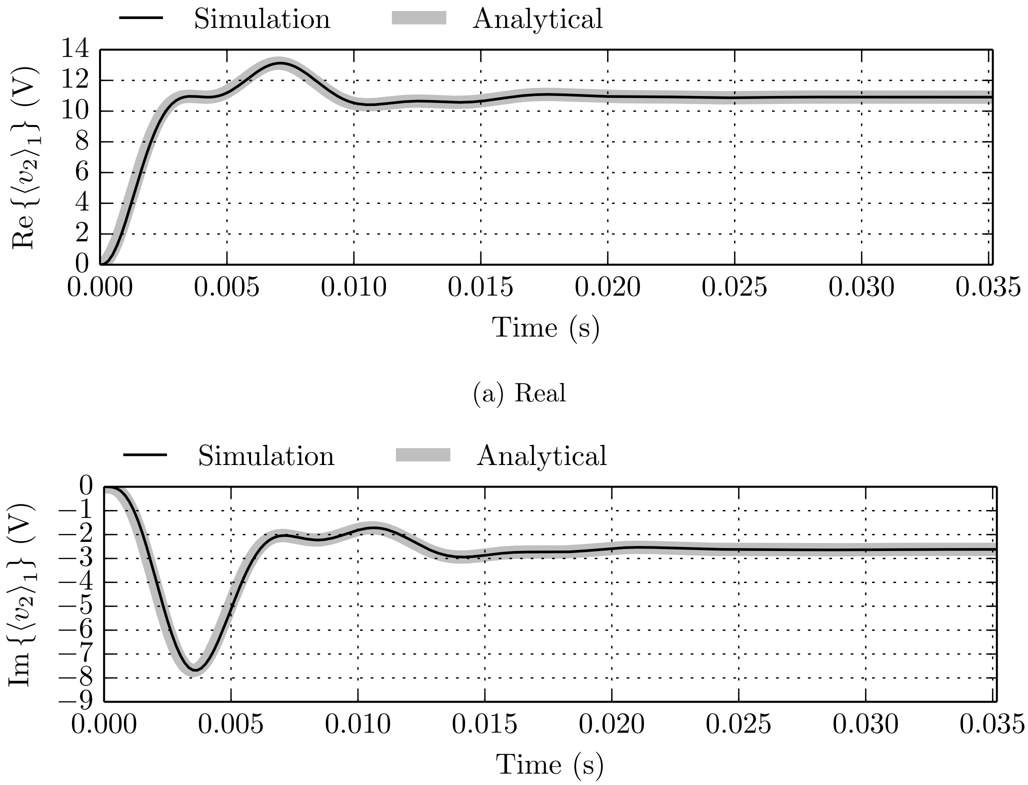

(a) Real

(b) Imaginary

Figure 3.22: Comparison of the output voltage dynamic phasors for the fundamental component

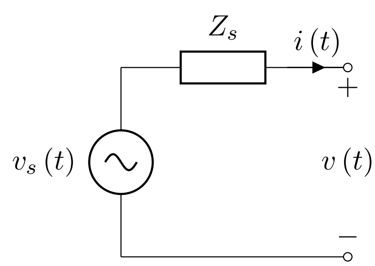

Figure 3.23: General form of a voltage source in terms of continuous time-domain quantities

Figure 3.24 illustrates the general form of a voltage source in terms of dynamics phasors. This form may be derived by applying the dynamic phasor operator to $v_s(t)$ and replacing all of the elements in Z_s with their dynamic phasor equivalents. The equivalent circuit illustrated by Figure 3.24 suggests that there are two requirements for modeling sources using dynamic phasors. The first requirement is that the original source waveform, $v_s(t)$, must be represented in terms of its dynamic phasors, $\langle v_s \rangle_k(t)$, which will be discussed in Section 3.3.1. The second requirement is that the source impedance network must be converted to a discrete Norton equivalent for simulation, which will be discussed in Section 3.3.2.

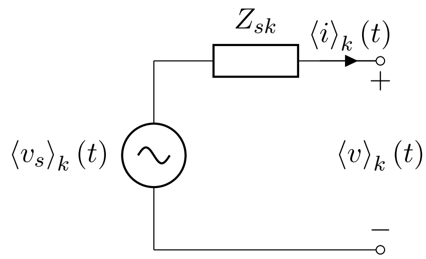

Figure 3.24: General form of a voltage source in terms of continuous dynamic phasors

3.3.1 Waveform Modeling

The dynamic phasors for source waveforms may be derived by first assuming that the waveforms have constant parameters, such as magnitude and phase, and are T_0-periodic. The dynamic phasors of a given waveform are equal to its Fourier series coefficients as discussed in Section 1.2 under this assumption. As an example, consider a square wave defined by

$$x(t) = \begin{cases} A & 0 \le t < T_0/2 \\ -A & T_0/2 \le t < T_0, \end{cases} \tag{3.35}$$

where A is the magnitude of the waveform. The dynamic phasors of this waveform are equal to the Fourier coefficients of a square wave and are given by

$$\langle x \rangle_k (t) = \begin{cases} 0 & k \text{ even} \\ \dfrac{2A}{jk\pi} & k \text{ odd.} \end{cases} \tag{3.36}$$

It is sufficient to model a source using constant parameters for many simulation cases. However, it is advantageous to model sources using variable parameters in certain situations. For example, PSCAD/EMTDC sources include a mechanism for slowly increasing the magnitude of sinusoidal waveforms upon initialization of a simulation case [45]. This feature is valuable for sensitive cases where a sudden step change may cause instability. The method used in this work to model these changes was to use the dynamic phasors of the constant parameter form of the source and simply allow the parameters of the source to change. For example, suppose the the square waveform given by (3.35) must be modeled with a variable magnitude. The dynamic phasors for the square waveform may be modeled with a time-dependent magnitude as follows:

$$\langle x \rangle_k (t) = \begin{cases} 0 & k \text{ even} \\ \dfrac{2A(t)}{jk\pi} & k \text{ odd.} \end{cases} \tag{3.37}$$

Figure 3.25 illustrates the square waveform defined by (3.35) where the amplitude undergoes a step change from A to $2A$ at time t_s. The dynamic phasor waveform reconstructed using the first 20 harmonics is also included in Figure 3.25. The results show that the dynamic phasor waveform accurately reconstructs and represents the time-domain waveform.

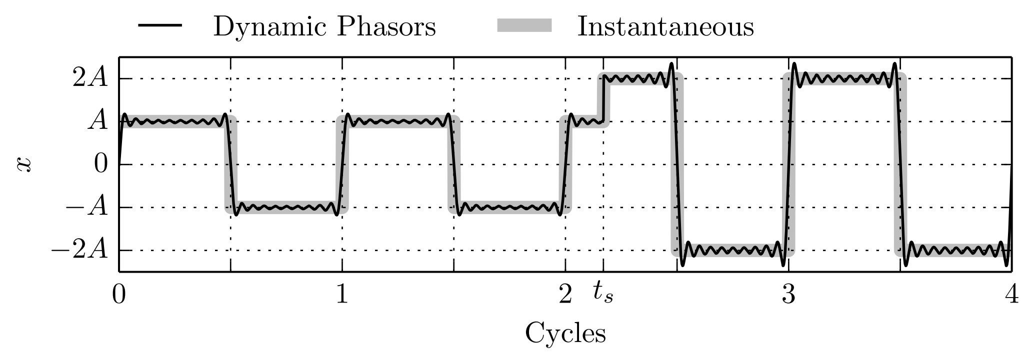

Figure 3.25: Comparison of a variable amplitude square wave

A special case that cannot be handled using the variable parameter technique previously discussed are waveforms with a variable frequency. The frequency of a source may change in certain circumstances, such as variable frequency control of resonant converters [13]. Variable frequency waveforms are a special case because the technique previously discussed requires that the waveforms be T_0-periodic. The dynamic phasors of the source waveform are not equal to its Fourier coefficients without this assumption.

There has been limited research into simulating variable frequency systems using dynamic phasors. In fact, the requirement of using a fixed base frequency has been listed as a limitation of dynamic phasor based simulations [30]. The original dynamic phasors formulation includes adjustments to incorporate a variable base frequency [8]. However, the adjustments introduce significant complexity to the method in the form of implicit integral and differential equations. A different approach has also been explored, which involves assuming that each variable in a system may be written in the form of a set of complex exponentials with time-varying magnitudes [29]. The complex exponentials for each variable are in terms of a phase angle that describes its oscillatory characteristics. These variables are then substituted into the system state equations and simplified to reveal a set of differential equations in terms of the time-varying coefficients. This method results in a system of equations that properly capture the dynamics of variable frequency systems. However, the state equations are formulated by hand and require insight and intuition. Therefore, this method is poorly suited for a general purpose simulator.

The approach used in this work to model variable frequency sources involves a modification to the assumed state variable approach. The equations and variables of a system are also written in terms of a phase angle that describes their oscillatory characteristics. However, instead of directly substituting these variables into the system equations, their dynamic phasors are derived by expanding the variables into a Fourier series and applying a simple transformation. The dynamic phasors of variable frequency sources may be derived by considering sources as 2π-periodic functions of instantaneous phase angle rather than time and frequency. The Fourier series for source waveforms using this method is given by

$$x\left(t\right) = \sum_{k=-\infty}^{\infty} X_k e^{jk\theta(t)}, \tag{3.38}$$

where X_k and $\theta\left(t\right)$ are the Fourier coefficients and instantaneous phase angle of $x\left(t\right)$, respectively. The instantaneous phase angle of a waveform is related to its angular frequency through the relationship given by

$$\frac{d\theta}{dt} = \omega\left(t\right), \tag{3.39}$$

where $\omega\left(t\right)$ is the time-dependent angular frequency of the waveform. The dynamic phasors for variable frequency sources may be derived using the Fourier series given by (3.38) and a simple transformation. Adding and subtracting the product of the dynamic phasors base angular frequency and time, $\omega_0 t$, from the exponential term in (3.38) yields:

$$x(t) = \sum_{k=-\infty}^{\infty} \langle x \rangle_k (t)\, e^{jk\omega_0 t}, \tag{3.40}$$

where the dynamic phasors of $x(t)$ are given by

$$\langle x \rangle_k (t) = X_k e^{jk(\theta(t) - \omega_0 t)}. \tag{3.41}$$

As an example of this method, consider once again the square wave given by (3.35) with a constant magnitude and a step change in the frequency defined by

$$\omega = \begin{cases} \omega_0 & t \leq t_s \\ 2\omega_0 & t > t_s. \end{cases} \tag{3.42}$$

The instantaneous phase angle may be obtained by substituting (3.42) into (3.39) and assuming that $\theta(0) = 0$, which yields:

$$\theta(t) = \begin{cases} \omega_0 t & t \leq t_s \\ \omega_0 (2t - t_s) & t > t_s. \end{cases} \tag{3.43}$$

Figure 3.26 illustrates the square wave defined by (3.35) with the step change in frequency defined by (3.42). The dynamic phasor waveform reconstructed using the first 20 harmonics is also included in Figure 3.26. The results show that the dynamic phasor waveform accurately captures the step change in frequency and is in good agreement with the time-domain waveform.

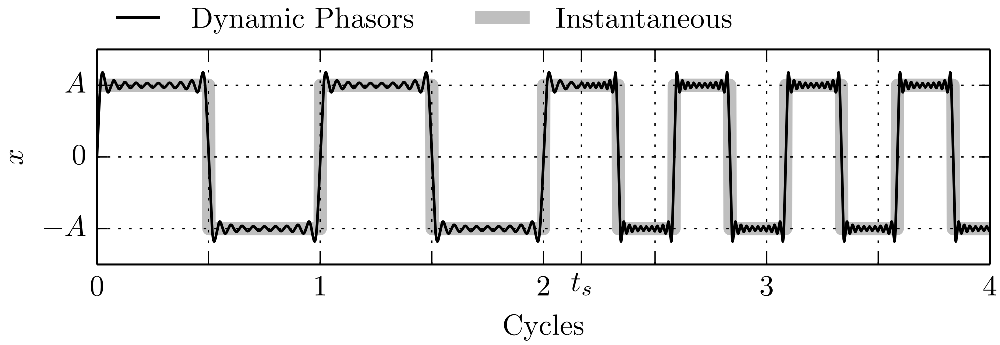

Figure 3.26: Comparison of a variable frequency square wave

3.3.2 Impedance Modeling

The dynamic phasor voltage source model illustrated by Figure 3.24 must be converted to a discrete Norton equivalent so that it may be included in the nodal analysis-based simulation method. First of all, consider the situation when the source impedance is completely resistive. The relationship between the ideal voltage source, terminal voltage, and current leaving the source in Figure 3.23 is given by

$$\langle v_s \rangle_k (t) = \langle v \rangle_k (t) + R_s \langle i \rangle_k (t), \tag{3.44}$$

where R_s is the equivalent source resistance. Rearranging the terms in (3.44) yields:

$$\langle i \rangle_k (t) = \langle i_s \rangle_k (t) - G_s \langle v \rangle_k (t), \tag{3.45}$$

which gives the dynamic phasors of the current leaving the source in terms of an equivalent current source, $\langle i_s \rangle_k (t)$, the terminal voltage dynamic phasors, and the equivalent source conductance, G_s. The expression given by (3.45) may be converted directly to the discrete form by replacing the continuous quantities with discrete quantities as follows:

$$\langle i \rangle_k [n] = \langle i_s \rangle_k [n] - G_s \langle v \rangle_k [n]. \tag{3.46}$$

The expression given by (3.46) defines the discrete dynamic phasor Norton equivalent for the voltage source with a resistive source impedance model, which is illustrated by Figure 3.27.

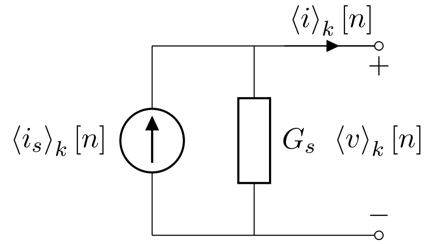

Figure 3.27: A voltage source and resistive impedance in terms of discrete dynamic phasors

Numerical integration is required to derive discrete Norton equivalents for voltage source models where the source impedance includes dynamic elements, such as inductors. The simple component equivalents discussed in Section 3.1 may be used to derive a discrete Norton equivalent for voltage sources where the impedance may be represented by a single capacitor or inductor. The composite element method discussed in Section 3.2 may be used to derive a discrete Norton equivalent for voltage sources where the impedance cannot be modeled using a single circuit element. Assuming that the dynamics of the source impedance illustrated in Figure 3.23 may be written as a set of state and output equations of the form given by

$$\frac{d\mathbf{x}}{dt} = \mathbf{A}\mathbf{x}(t) + \mathbf{B}v_z(t); \text{ and} \tag{3.47}$$

$$i(t) = \mathbf{C}\mathbf{x}(t) + Dv_z(t), \tag{3.48}$$

then the discrete dynamic phasor Norton equivalent may be derived using the technique demonstrated in Section 3.2 as follows:

$$\langle i\rangle_k[n] = y_{sk}\langle v_z\rangle_k[n] + I_{hk}[n-1], \tag{3.49}$$

where y_{sk} and $I_{hk}[n-1]$ are the discrete admittance and history current for the generic voltage source, respectively, and are given by

$$y_{sk} = \mathbf{C}\mathbf{M}_{0k} + D; \text{ and} \tag{3.50}$$

$$I_{hk}[n-1] = \mathbf{C}e^{\mathbf{A}_k\Delta t}\langle\mathbf{x}\rangle_k[n-1] + \mathbf{C}\mathbf{M}_{1k}\langle v_z\rangle_k[n-1]. \tag{3.51}$$

The voltage across the source impedance is related to the ideal voltage source and the terminal voltage of the device in terms of discrete dynamic phasors as follows:

$$\langle v_z \rangle_k [n] = \langle v_s \rangle_k [n] - \langle v \rangle_k [n] \, . \tag{3.52}$$

Substituting (3.52) into (3.49) and simplifying gives the general form of the discrete Norton equivalent for voltage source models with dynamic source impedances. The discrete equivalent for the voltage source is given by

$$\langle i \rangle_k [n] = I_{sk} [n] - y_{sk} \langle v \rangle_k [n] + I_{hk} [n-1] \, , \tag{3.53}$$

where $I_{sk} [n]$ is the discrete equivalent current injection of the source model and is defined as follows:

$$I_{sk} [n] = y_{sk} \langle v_s \rangle_k [n] \, . \tag{3.54}$$

Figure 3.28 illustrates the Norton equivalent given by (3.53), which can be substituted directly into dynamic phasor equivalent circuits.

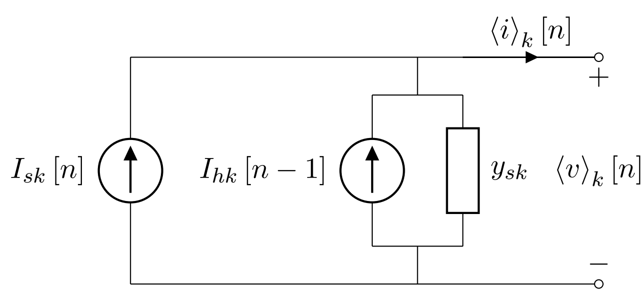

Figure 3.28: A voltage source and dynamic impedance in terms of discrete dynamic phasors

3.3.3 Simulation Results

Simulations were carried out using the example circuit and parameters given in Section 3.1.4. However, the current source and source resistance in Figure 3.11 were replaced by a voltage source and resistance as shown in Figure 3.29. This voltage source model was selected since its discrete dynamic phasor model is equivalent to the current source and resistor parallel combination shown in Figure 3.13. Therefore, the dynamic phasor discrete equivalent circuit shown in Section 3.1.4 may be used once again to simulate the circuit.

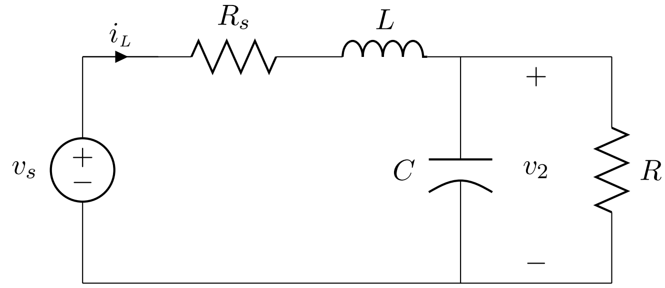

Figure 3.29: RLC example circuit with a square wave voltage source

The voltage source in Figure 3.29 was modeled as a square wave with an amplitude of 100 V and an initial frequency of 60 Hz. At 0.1 s, the frequency of the voltage source is increased to 90 Hz. The frequency domain response of the circuit shown in Figure 3.16 demonstrates that there is significant harmonic content when the source is operated at 60 Hz. Therefore, simulations were carried out for the first, third, and fifth harmonics. Figures 3.30 and 3.31 illustrates the reconstructed output voltage, $v_2(t)$, and inductor current, $i_L(t)$, waveforms simulated using dynamic phasors as well as the simulation results produced by PSCAD/EMTDC. These plots illustrate that the dynamic phasor and PSCAD/EMTDC simulation results are in good agreement.

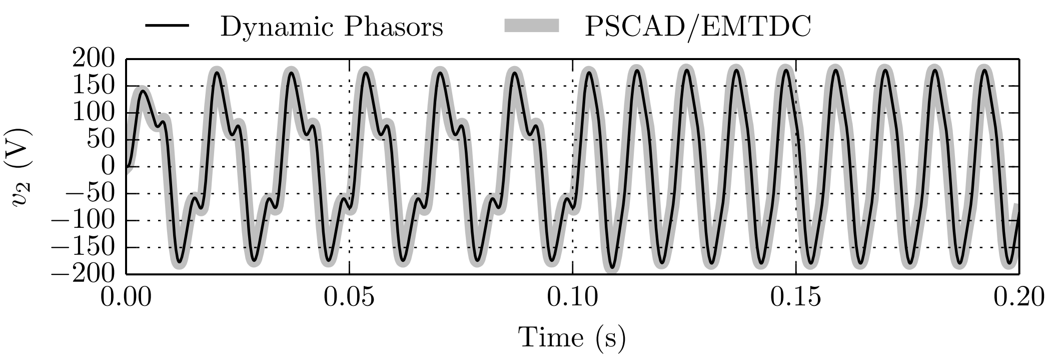

Figure 3.30: Comparison of the output voltage waveforms

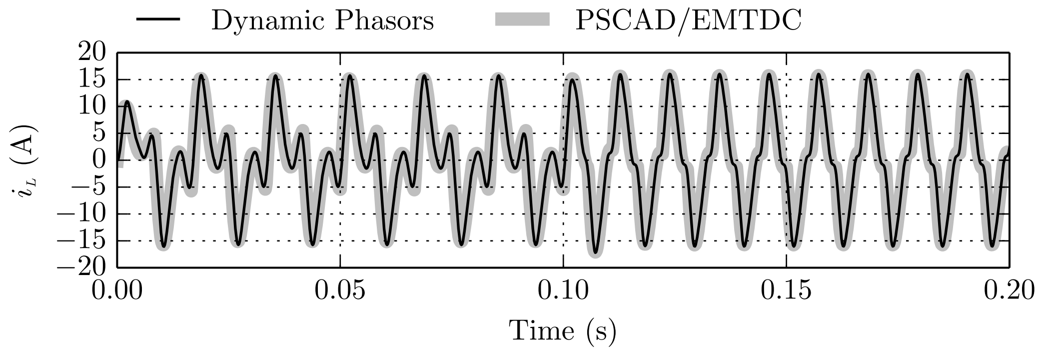

Figure 3.31: Comparison of the inductor current waveforms

3.4 Summary

This chapter presented a new general purpose method for simulating circuits using dynamic phasors based on the nodal analysis method discussed in Chapter 2. Circuits simulated using this method are first converted to their equivalent dynamic phasor based representation using the in-place circuit averaging method. Each element in the circuit is then converted to a discrete Norton equivalent. The discrete equivalents for simple circuit elements were provided in this chapter, which are based on the exponential integration method discussed in Section 2.3. A generalized procedure for creating composite component models was also presented in this chapter, which is based on state space and the exponential integration method. Composite component models are valuable because they remove nodes from the discrete equivalent system, which has a significant impact on the computational burden of dynamic phasor-based simulations. Voltage source models were also presented in this chapter, which included an extension of the composite components method for modeling complex source impedance networks. The voltage sources section in this chapter also presented a new method for modeling variable frequency behaviour. Comparisons with analytical and PSCAD/EMTDC simulation results in this chapter demonstrated that the dynamic phasor method developed in this work accurately captures the behaviour of basic linear circuits.

Chapter 4

Control and Measurement Systems

Control systems are critical components in many fields of engineering and science [39]. Control systems are used to ensure a system remains at the desired operating point when subjected to disturbances, such as variations in the system and faults [46]. There are several control levels in power systems, which are carefully coordinated to maintain the reliability of the system and maximize its efficiency [4]. For example, individual generating units have control systems to regulate the speed and voltage of the machine, while the amount of power output of all units is selected by the system generation controls.

A particularly important subset of control systems are feedback or closed-loop control systems. Feedback control systems are defined as those that use measurements and information about the current state of the system to adjust control parameters and ensure the system operates at the desired operating point [39]. This type of control is generally used in situations where a system is constantly changing and subjected to disturbances. Maintaining the system at the desired operating point would be impossible in these situations without feedback.

Feedback control systems involve measurement and decision making tasks to correct any deviations from a desired operating point [46]. The measurement tasks may involve some form of filtering to remove noise while the decision making tasks are often carried out by controllers with some form of integral or differential behaviour, such as proportional-integral (PI) controllers [39]. As a consequence, control and measurement systems introduce additional dynamic behaviour to physical systems. Therefore, it is essential that these systems are modeled properly to ensure that simulations of physical systems involving controls are accurate and reliable [1].

Control systems are often represented graphically using block diagrams. These diagrams are used to illustrate how different elements in a system are related [39]. Each block represents a different part of the system, where the relationship between the input and output is generally described mathematically using a Laplace transfer function. Figure 4.1 illustrates the block diagram for a simple generic feedback control system, where $r(t)$ is the input or reference signal and $y(t)$ is the output signal. The transfer function $G(s)$ may be used to represent the dynamics of the system and any associated controllers and $H(s)$ may be used to represent the dynamics of any measurement devices.

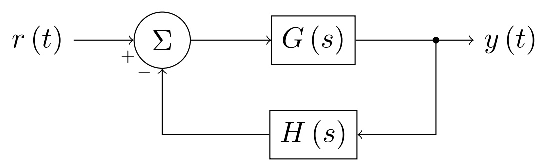

Figure 4.1: Block diagram for a simple generic feedback control system

Laplace transfer functions are convenient for representing the continuous dynamics of control systems. However, the relationship between inputs and outputs in a control system must be represented using differential equations for the purposes of simulation. There are a number of methods for converting Laplace domain transfer functions to state equations [39]. For example, the successive differentiation method is used in PSCAD/EMTDC [1]. The numerical methods discussed in Chapter 2 may be then used to simulate the output variables of a control system in response to its input variables.

This chapter focuses on the methods used in this work to incorporate control system models into the general purpose simulation method discussed in Chapter 3. Section 4.1 examines how control systems may be modeled in the context of dynamic phasors. Following this, Section 4.2 presents the methods used to simulate control system models. Finally, the method used to integrate control systems into the general purpose simulation method is discussed in Section 4.3.

4.1 Control System Modeling

Two methods are considered in this work to model measurement and control systems using dynamic phasors. The first method is a direct application of the dynamic phasor operator to the control system. This method considers both the electrical network and the controls as a single system and converts all system quantities to dynamic phasors. It is possible to use the direct method when the system consists entirely of linear control elements. For example, consider a simple second order linear filter, which may be represented using state equations as follows:

$$\frac{dx_1}{dt} = x_2(t); \tag{4.1}$$

$$\frac{dx_2}{dt} = -\omega_n^2 x_1(t) - 2\zeta\omega_n x_2(t) + \omega_n^2 u(t); \text{ and} \tag{4.2}$$

$$y(t) = x_1(t), \tag{4.3}$$

where ω_n and ζ are the natural frequency and damping factor of the filter, respectively [39]. These equations may be directly written in terms of dynamic phasors without any approximations as follows:

$$\frac{d\langle x_1\rangle_k}{dt} = -jk\omega_0 \langle x_1\rangle_k(t) + \langle x_2\rangle_k(t); \tag{4.4}$$

$$\frac{d\langle x_2\rangle_k}{dt} = -\omega_n^2 \langle x_1\rangle_k(t) - (2\zeta\omega_n + jk\omega_0)\langle x_2\rangle_k(t) + \omega_n^2 \langle u\rangle_k(t); \text{ and} \tag{4.5}$$

$$\langle y\rangle_k(t) = \langle x_1\rangle_k(t). \tag{4.6}$$

The direct method can also handle polynomial nonlinearities using the dynamic phasor multiplication property discussed in Section 1.2. The average power measurement system illustrated by Figure 4.2 [45] is an example of a nonlinear system that may be converted directly to a dynamic phasor representation. In this system, $G(s)$ is an arbitrary linear filter transfer function and $v(t)$ and $i(t)$ are the measured voltage and current waveforms, respectively.

Figure 4.2 illustrates that the meter consists of two distinct stages. The first stage multiplies the voltage and current to produce an intermediate signal, $p(t)$, which is equal to the instantaneous power at the point of measurement. The second stage is a simple linear filter designed to extract the dc component of the instantaneous power waveform generated by the first stage. Figure 4.3 illustrates the dynamic phasor form of the average power measurement system, where $G_k(s)$ is the kth harmonic form of the filter transfer function, $G(s)$, shown in Figure 4.2. The kth dynamic phasor of the instantaneous power waveform, $\langle p \rangle_k(t)$, is given by

$$\langle p \rangle_k(t) = \sum_{l=-\infty}^{\infty} \langle v \rangle_{k-l} \langle i \rangle_l \,, \tag{4.7}$$

which may be derived using the dynamic phasor multiplication property discussed in Section 1.2.

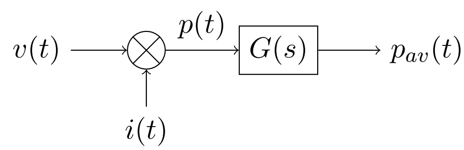

Figure 4.2: Average power meter in terms of time-domain quantities

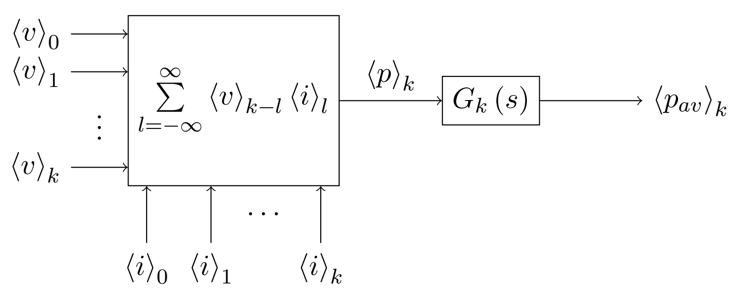

Figure 4.3: Average power meter in terms of dynamic phasors

Direct application of the dynamic phasor transformation to nonlinear systems is generally restricted to systems that exhibit polynomial nonlinearities. In general, it is not possible to obtain closed form dynamic phasor expressions for the majority of nonlinear systems [8]. For example, a system that exhibits saturation cannot be converted to a dynamic phasor representation using the direct method. The second method that was considered in this work addresses the problems associated with modeling nonlinear control systems. This method differs from the direct method as it separates the control system and electrical network into separate entities. The electrical network is modeled using dynamic phasors whereas the control system is modeled using its standard time-domain differential equations. A control system modeled using this method cannot be directly interfaced to the electrical network since the control system quantities are not dynamic phasors. Therefore, assumptions and approximations must be used to interface the electrical network to the control system model.

This method is used extensively in literature to handle complex control systems in power systems modeled using dynamic phasors. An example is the phase-locked loop (PLL), which is an essential control element for power electronic systems. The PLL is a highly nonlinear component used to generate a reference angle for power electronic converters that interface with an ac network [47]. The approximate method has been used in literature to create a PLL model that can be interfaced with a dynamic phasor network model [20, 48].

An example of a measurement system that may be represented using this method is a three phase root mean square (RMS) voltage meter. Figure 4.4 illustrates the RMS voltage meter used in PSCAD/EMTDC for three phase systems, where v_a, v_b, and v_c are the measured ac system voltage and v_{rms} is the measured RMS voltage of the system [45]. The filter in Figure 4.4, $G(s)$, is designed to extract and scale the dc component of v_d such that it is equal to the RMS value of the line-to-line voltage.

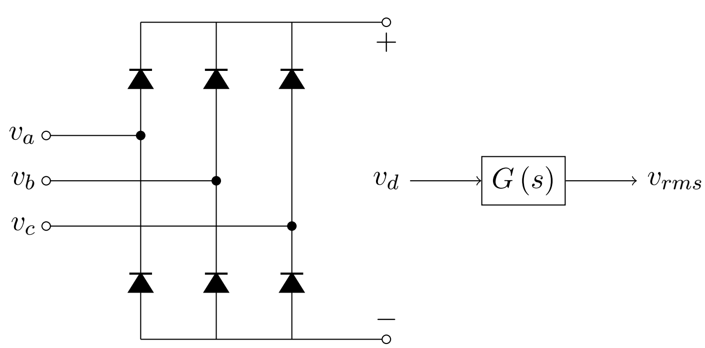

Figure 4.4: Three phase RMS voltage meter model used in PSCAD/EMTDC

While it is possible to model a three phase rectifier using dynamic phasors, a simpler and more efficient approach is to take advantage of the fact that the magnitude of the phase voltages are directly available in dynamic phasors [20]. Assuming that the ac system is balanced, an RMS meter in terms of dynamic phasors may be constructed as shown in Figure 4.5, where $G(s)$ is the low pass filter from Figure 4.4. The intermediate signal, v_x, is equal to the RMS value of the a-phase voltage, which may be calculated as follows [44]:

$$v_x = \sqrt{\langle v_a \rangle_0^2 + 2 \sum_{k=1}^{\infty} |\langle v_a \rangle_k|^2}. \tag{4.8}$$

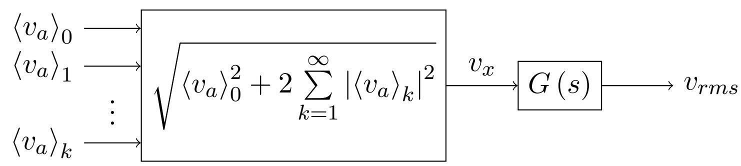

Figure 4.5: Three phase RMS voltage meter in terms of dynamic phasors

The dynamic phasor RMS voltage meter demonstrates the essential components of the approximate modeling method. The first stage of the meter uses the mathematical expression for the RMS quantity of a complex Fourier series given by (4.8) to generate the auxiliary signal v_x. This stage provides the interface between the dynamic phasor network model and the time-domain control system model. The second stage is the filter block, which appears to be an unnecessary component since v_x is equal to the RMS value of the a-phase voltage. However, the dynamics of the filter are particularly important if the meter is used as part of a larger control system. Therefore, this component is essential to ensure that the dynamic phasor RMS voltage meter accurately captures the dynamics of the time-domain quantity meter that would be otherwise omitted if v_x was used as the meter output.

4.2 Simulation of Control Systems

The models obtained using the methods discussed in the previous section must be converted from continuous system representations to discrete difference equations for simulation. The components in a control system were broadly classified as either static or dynamic in this work. Static components are those that relate their inputs and outputs through algebraic relationships. These components may be simulated by simply substituting in the discrete form for each quantity in the component relationship. For example, the convolution component in the average power meter in the previous section is a static component and may be simulated as follows:

$$\langle p\rangle_k[n] = \sum_{l=-\infty}^{\infty} \langle v\rangle_{k-l}[n]\,\langle i\rangle_l[n]\,. \tag{4.9}$$

Dynamic components are those that relate their inputs and outputs through differential equations. The exponential integrator and trapezoidal methods discussed in Chapter 2 are used in PSCAD/EMTDC to simulate dynamic control systems [1]. The same approach was used in this work to obtain difference equations for dynamic control blocks. As an example, consider the case where the filter in the average power meter is a first order system whose transfer function is given by

$$G(s) = \frac{P_{av}(s)}{P(s)} = \frac{1}{1+s\tau}, \tag{4.10}$$

where τ is the time constant of the filter. The input and output of (4.10) are related in the time-domain through the following ODE:

$$\frac{dp_{av}}{dt} = \frac{1}{\tau}\left(p(t) - p_{av}(t)\right). \tag{4.11}$$

Applying the dynamic phasor operator and associated properties to (4.11) yields:

$$\frac{d\langle p_{av}\rangle_k}{dt} = \frac{1}{\tau}\langle p\rangle_k(t) - \left(\frac{1}{\tau} + jk\omega_0\right)\langle p_{av}\rangle_k(t), \tag{4.12}$$

which gives the differential relationship between the meter input and output in terms of dynamic phasors. Applying the exponential integrator to (4.12) yields:

$$\langle p_{av}\rangle_k[n] = e^{(\Delta t/\tau + jk\omega_0\Delta t)}\langle p_{av}\rangle_k[n-1] + m_{0k}\langle p\rangle_k[n] + m_{1k}\langle p\rangle_k[n-1], \tag{4.13}$$

where

$$m_{0k} = \frac{\tau\left(e^{(\Delta t/\tau + jk\omega_0\Delta t)} - 1\right)}{\Delta t\left(1 + jk\omega_0\tau\right)^2} + \frac{1}{1 + jk\omega_0\tau};\ \text{and} \tag{4.14}$$

$$m_{1k} = \frac{\tau\left(1 - e^{(\Delta t/\tau + jk\omega_0\Delta t)}\right)}{\Delta t\left(1 + jk\omega_0\tau\right)^2} - \frac{e^{(\Delta t/\tau + jk\omega_0\Delta t)}}{1 + jk\omega_0\tau}. \tag{4.15}$$

The discrete form of the convolution equation given by (4.9) together with the filter difference equation given by (4.13) may be used to simulate the average power meter. Consider a system in which the voltage and current waveforms measured by the average power meter for $t \geq 0$ are sinusoidal and given by

$$v(t) = V_m \sin(\omega_0 t)\,; \text{ and} \tag{4.16}$$

$$i(t) = I_m \sin(\omega_0 t - \phi)\,, \tag{4.17}$$

respectively. The instantaneous power waveform at the point of measurement is given by

$$p(t) = \frac{V_m I_m}{2} \left(\cos(\phi) - \cos(2\omega_0 t - \phi)\right). \tag{4.18}$$

Equation (4.18) demonstrates that the instantaneous power in an ac system consists of a constant component, which corresponds to the average power at the point of measurement, as well as an oscillatory component whose frequency is double the frequency of the voltage and current [5]. Therefore, the set of harmonics for simulation of the average power meter with sinusoidal inputs must be equal to $\{0, 1, 2\}$ to accurately capture all of the meter dynamics. The dynamic phasors of the voltage and current waveforms for $t \geq 0$ are given by

$$\langle v \rangle_k = \begin{cases} \dfrac{V_m}{2j} & k = 1 \\ 0 & \text{otherwise; and} \end{cases} \tag{4.19}$$

$$\langle i \rangle_k = \begin{cases} \dfrac{I_m}{2j} e^{-j\phi} & k = 1 \\ 0 & \text{otherwise,} \end{cases} \tag{4.20}$$

respectively. The dynamic phasors of the intermediate signal may be derived by substituting (4.19) and (4.20) into (4.9) and are given by

$$\langle p \rangle_k = \langle v \rangle_{k+1} \langle i \rangle_1^* + \langle v \rangle_{k-1} \langle i \rangle_1 \,. \tag{4.21}$$

Equation (4.21) implies that the dynamic phasors of the intermediate signal are only nonzero when $k \pm 1 = \pm 1$. This condition is satisfied by the set $\{0, \pm 2\}$ and therefore, the dc component and second harmonic are required to simulate the average power meter using dynamic phasors. This observation is supported by (4.18), which shows that the only components that appear in the instantaneous power waveform in a purely sinusoidal ac system are the dc component and the second harmonic. The dynamic phasors for the intermediate signal may be derived by evaluating (4.21) at $k = 0$ and $k = 2$ and are given by

$$\langle p \rangle_0 = \frac{V_m I_m}{2} \cos(\phi) \, ; \text{ and} \tag{4.22}$$

$$\langle p \rangle_2 = -\frac{V_m I_m}{4} e^{-j\phi}, \tag{4.23}$$

respectively. Simulations of the average power meter were carried out assuming that all initial conditions are zero and using the parameters listed in Table 4.1. Figures 4.6 and 4.7 illustrate the dc and second harmonic waveforms for the output of the average power meter with sinusoidal input waveforms, respectively. These waveforms show that the analytical and simulation results are in good agreement.

Simulations of the average power meter using the parameters listed in Table 4.1 were also carried out using PSCAD/EMTDC. Figure 4.8 illustrates the PSCAD/EMTDC simulation results along with the meter output waveform reconstructed using the dynamic phasor simulation results. The simulation results demonstrate that the two methods are in good agreement.

Table 4.1: Simulation parameters for the average power meter

Parameter	**Value**
f_0	60 Hz
τ	0.05 s
V_m	100 V
I_m	1 A
ϕ	0°

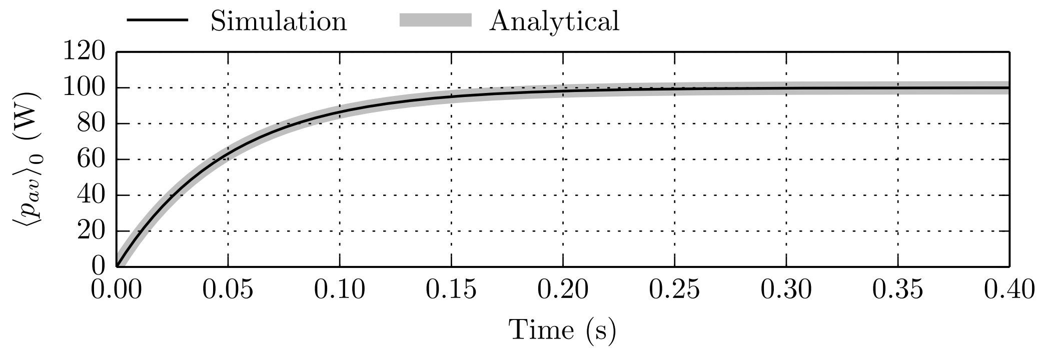

Figure 4.6: Comparison of the average power meter output dynamic phasors for the dc component

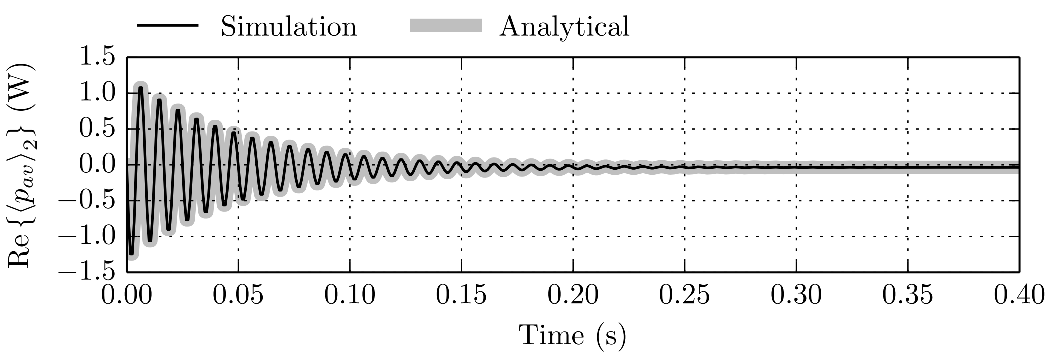

(a) Real

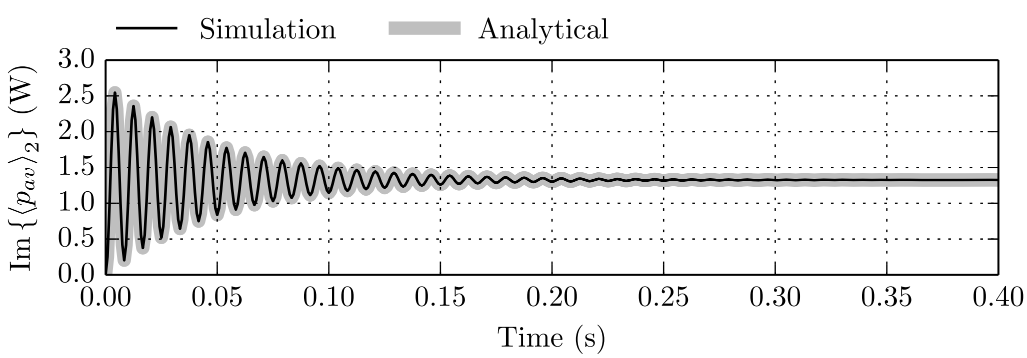

(b) Imaginary

Figure 4.7: Comparison of the average power meter output dynamic phasors for the second harmonic

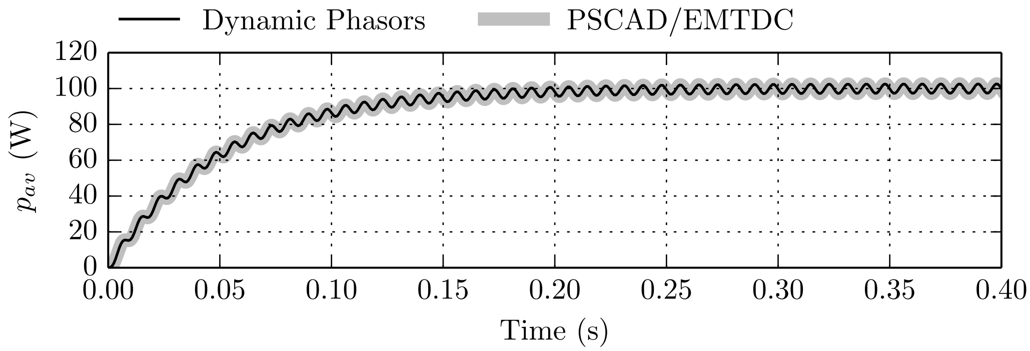

Figure 4.8: Comparison of the average power meter output waveforms

4.3 Integration with Electromagnetic Transient Simulation

The control and measurement system models must be fully integrated into the nodal analysis method for simulation of the entire power system model. The approach used by PSCAD/EMTDC is to decouple and interweave the electrical network and the control system solution through a one time step delay [1]. The first part of each time step advances the electrical network solution using the values calculated by the control system from the previous time step as inputs. The second part then advances the control system solution using the updated values from the electrical network solution in the first part of the time step.

The method used to implement controllers in PSCAD/EMTDC also breaks down control systems into individual blocks [1]. Commonly used control blocks are then provided as part of the control systems model library, such as a PI control block. Each block is responsible for modeling and simulating the output of the block in response to the input variables. For dynamic blocks, this includes obtaining a difference equation and updating all of the internal variables at each time step.

The methods used to implement controllers in PSCAD/EMTDC offer a number of advantages to nodal analysis-based simulation. First of all, this method is highly flexible as it decouples the electrical network from the control system, which allows each to be modeled and simulated independently using methods that are most appropriate to the individual system components. Furthermore, individual blocks in a control system may be modeled independently and used to build large and complex control systems in simulation cases [1].

The decoupled solution method is often viewed as problematic as it artificially introduces a time delay, which may adversely affect the stability of nodal analysis-based simulations [1]. There has been some effort in literature to remove the delay introduced by the decoupled method through modified network solution methods [49]. However, these methods require modifications that increase the computational burden of simulations [1]. Furthermore, the time step delays are commonly viewed as an accurate portrayal of modern digital controllers due to the sampling process used to capture analog inputs, such as voltage and current measurements. Therefore, the same method was used to integrate control systems into the general purpose dynamic phasor simulation method developed in this work.

Figures 4.9 and 4.10 illustrate an example three phase circuit and control system that will be used to demonstrate the integration of controls into the general purpose simulation method. Figure 4.9 illustrates the single line diagram for the electrical network, which consists a three phase load connected to a sinusoidal voltage source. Figure 4.10 illustrates the control system, which uses a PI controller to regulate the RMS line-to-line voltage across the output resistor by adjusting the amplitude of the voltage source. The RMS meter used in this example is illustrated by Figure 4.5 in Section 4.1, where the output filter is the first order transfer function given by [45]

$$G(s) = \frac{1}{T_f s + 1}. \tag{4.24}$$

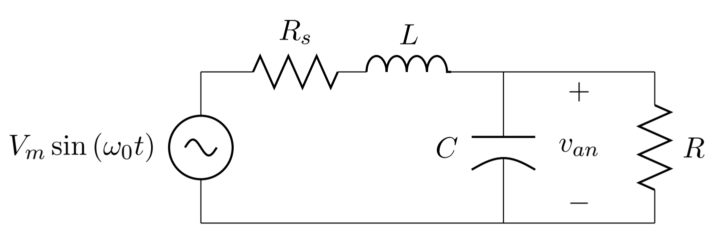

Figure 4.9: Single line diagram of a three phase RLC circuit with a sinusoidal voltage source

Simulations of the system illustrated in Figures 4.9 and 4.10 were carried out assuming that all initial conditions are zero and using the parameters given in Table 4.2. The reference RMS voltage, v_{ref}, was initially set to 10 V, and at 0.2 s is increased to 15 V.

Figure 4.11 illustrates the RMS meter output simulated using both dynamic phasors and PSCAD/EMTDC. Figure 4.12 illustrates the resistor voltage waveform near the moment where the voltage reference, v_{ref}, is stepped up to 15 V. The simulation results show that there is some disagreement near initialization and the reference voltage step change at 0.2 s. This error may be attributed to the modeling differences used to implement the RMS meter as discussed in Section 4.1. However, the simulation results appear to be in good agreement, despite the discrepancies near sudden changes in the reference value.

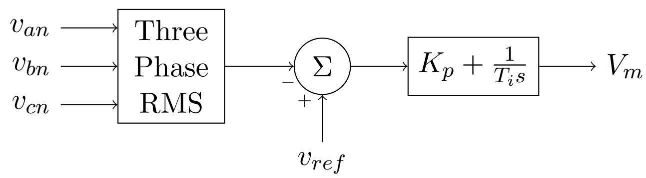

Figure 4.10: Feedback control system for the three phase RLC circuit

Table 4.2: Parameters for the example three phase RLC system with feedback control

Parameter	**Value**	**Parameter**	**Value**
f_0	60 Hz	C	0.796 mF
R_s	1 mΩ	K_p	1.25
R	25 Ω	T_i	2 ms
L	0.318 H	T_f	20 ms

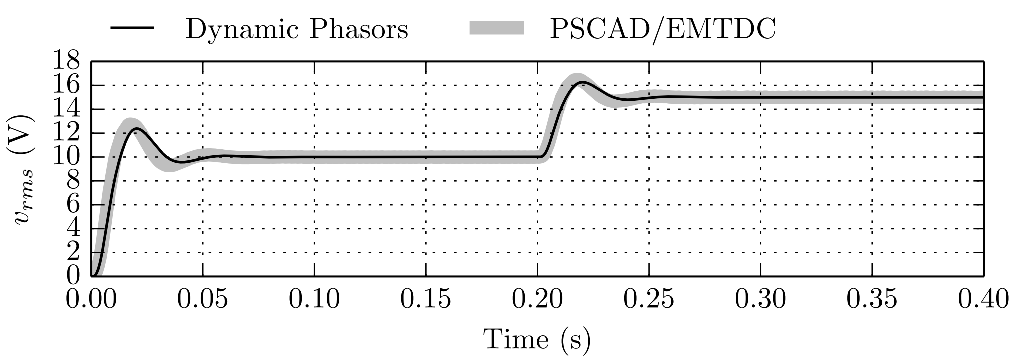

Figure 4.11: Comparison of the RMS meter output waveforms

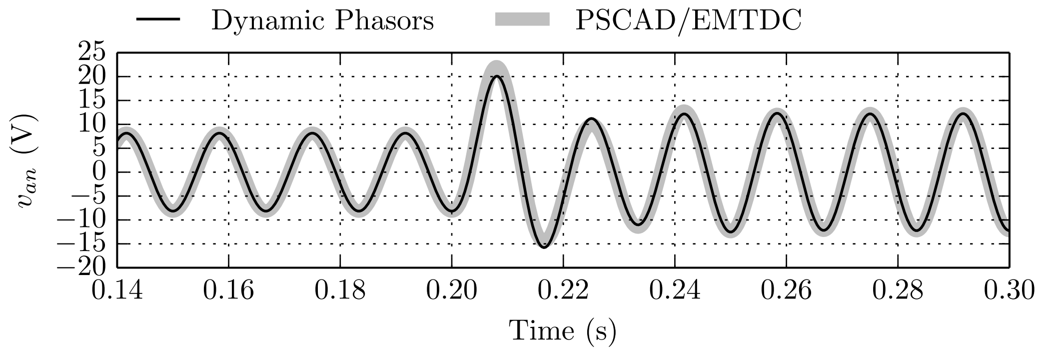

Figure 4.12: Comparison of the resistor voltage waveforms

4.4 Summary

This chapter presented a review of the techniques available for modeling and simulation of control systems using dynamic phasors. Two primary methods are available for modeling control systems in dynamic phasors. The first method involves a direct application of the dynamic phasor operator to the control system model. While this method provides an accurate representation of the control system, it is limited to systems that are either linear or exhibit polynomial nonlinearities. The second method involves separating the control system from the dynamic phasor model of the electrical network and interfacing the two systems using approximations. This control method is widely used as it can handle a wide variety of nonlinearities. A method for integrating control systems into the general purpose dynamic phasor simulation method discussed in Chapter 3 were also presented in this chapter. The method used to integrate control systems involves introducing a time step delay between the electrical network solution and the control solution, which is the method used by programs such as PSCAD/EMTDC. Comparisons with PSCAD/EMTDC simulation results in this chapter demonstrated that the dynamic phasor method developed in this work accurately captures the behaviour of electrical networks that include control system models.

Chapter 5

Power Electronic Converters

Power electronic converters have significantly contributed to the advancement of modern power systems and are found in a number of different applications. The primary goal of converters in industrial settings is to transform power produced by a source to a form that may be used by loads [46]. The adjustable-speed motor drive is an important industrial application of power electronics [44]. Adjustable-speed drives allow motors such as pumps and compressors to operate at their optimal speed, improving the efficiency of the motor. Power electronics are also found in a number of transmission level applications, such as interconnection of renewable resources and reactive power support. For example, the static VAR compensator (SVC) is based on inductors and capacitors controlled by power electronic switches. These devices can either provide or consume reactive power, depending on the requirements of the system. SVCs are also highly controllable and may be used to improve the stability and reliability of transmission systems.

One of the most notable applications of power electronics is the HVDC transmission system. HVDC transmission systems are more efficient and cost effective for long distance overhead power transmission [44]. HVDC transmission systems also offer a number of other benefits, such as improved power system reliability. The controls in an HVDC installation may be used to remove unwanted oscillations in the power system. Furthermore, HVDC systems may be used to connect systems of different operating frequencies, which is impossible with a direct ac connection.

Many HVDC transmission systems are implemented using a power electronic converter known as the LCC [44]. Figure 5.1 illustrates the general circuit for an LCC constructed using thyristors. This circuit also includes an inductance on the ac side, L_s, which is known as the source side inductance. For example, the source side inductance is used to represent the leakage inductance of converter transformers in HVDC applications.

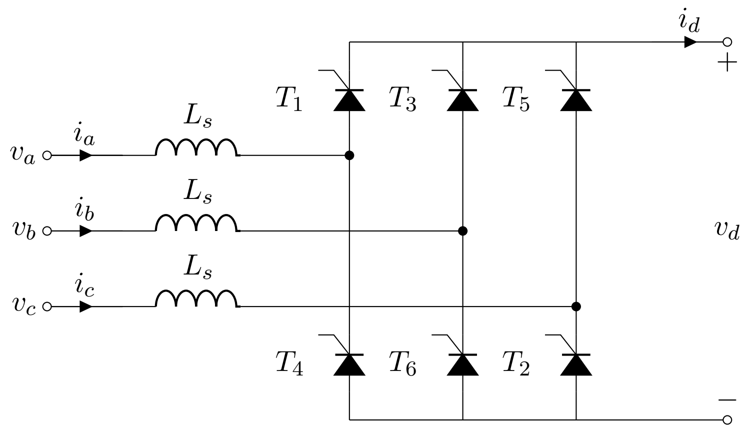

Figure 5.1: General form of the LCC

This type of converter is known as a line-commutated converter because it relies on the ac terminal voltage to turn the switching devices off [44]. The two types of switching devices considered in this work are diodes and thyristors. LCCs constructed using diodes are uncontrolled because the status of the diodes in the bridge is completely reliant on the conditions of the external ac and dc systems. LCCs constructed using thyristors are controlled because the point in time in which conduction beings for each thyristor may be controlled through a gate signal. However, the point in time where conduction ceases for each thyristor is still dependent on the conditions of the external systems.

LCCs operate at the frequency of the ac system they are connected to since they use the ac system for commutation of the dc-side current between phases [44]. The implication of this property for dynamic phasor-based simulation is that knowledge of the system frequency must be available prior to simulation. This knowledge is required to ensure that the LCC model is properly coordinated with the ac system model. In general, it is sufficient to assume that the ac system frequency is equal to the dynamic phasor base frequency such that the fundamental component of the ac system corresponds to the first harmonic of the LCC model. However, this requirement is an important consideration if the LCC is to be used to simulate an HVDC transmission system where the two ac systems have different operating frequencies.

LCC based HVDC systems have garnered a significant amount of attention in dynamic phasor research. A complete model of the CIGRE HVDC benchmark system that uses dynamic phasors for the entire electrical network has been developed in literature [48]. This research includes a detailed derivation of the LCC dynamic phasor model using the switching function approach. Comparisons of simulation results with PSCAD/EMTDC demonstrate that the dynamic phasor model accurately captures the dynamics of the converter for all cases except during commutation failure. Furthermore, this research demonstrated that the dynamic phasor approach also accurately models the converter quantities for higher order harmonics. Other research has also suggested improvements to LCC dynamic phasor models to take into account asymmetrical conditions in the ac system and commutation failure [32, 50] and LCC properties such as thyristor dead time [51]. In particular, it has been shown that asymmetrical conditions in the ac system may be accounted for using higher order harmonics [32].

This chapter begins with a brief introduction into the switching function method in Section 5.1, which is used to model power electronic converters using dynamic phasors. Following this, a basic discrete equivalent is developed for an LCC constructed using diodes and neglecting any source side inductance in Section 5.2. This equivalent is then modified in Section 5.3 to incorporate thyristors. Section 5.4 discusses any final modifications required to include the source side inductance and complete the general discrete dynamic phasor equivalent of the LCC illustrated by Figure 5.1. Finally, simulation results are presented in Section 5.5 comparing the dynamic phasor model with results obtained using PSCAD/EMTDC.

5.1 Switching Function Method

The approach that has been used extensively in literature to model power electronic converters using dynamic phasors is based on the switching function method. Switching devices are generally simulated using a decision-based model in EMT simulators [1]. These models examine the conditions imposed by the external system on the device in each time step and determine its status based on those conditions. This approach, coupled with interpolation to account for discrepancies in the switching instant, results in an accurate switching device model that may be used in any configuration. However, this approach cannot be used in dynamic phasor-based simulation since the instantaneous time-domain waveforms are not available for the device models to make decisions.

Switching functions are normalized piecewise-continuous functions that describe the steady state operation of a power electronic converter or device [52]. For example, consider the simple dc/dc step-down converter illustrated in Figure 5.2 [9]. Suppose that the switch is operated periodically with period T_0 such that it is conducting for first DT_0 seconds and the diode is conducting for the remainder of each period. Furthermore, suppose that the load parameters are selected such that the load current is approximately constant. The filter input voltage and source current in Figure 5.2 are given by

$$v(t) = s(t)\, v_s(t)\,; \text{ and} \tag{5.1}$$

$$i_s(t) = s(t)\, i(t)\,, \tag{5.2}$$

respectively, where $s(t)$ is the converter switching function and is given by

$$s(t) = \begin{cases} 1 & 0 \le t < DT_0 \\ 0 & DT_0 \le t < T_0 \end{cases} \tag{5.3}$$
$$s(t) = s(t + nT_0)\,.$$

The dynamic phasors for the load voltage and source current may be obtained by applying the dynamic phasor operator and multiplication property to (5.1) and (5.2) and are given by

$$\langle v \rangle_k = \sum_{l=-\infty}^{\infty} \langle s \rangle_{k-l} \langle v_s \rangle_l\,; \text{ and} \tag{5.4}$$

$$\langle i_s \rangle_k = \sum_{l=-\infty}^{\infty} \langle s \rangle_{k-l} \langle i \rangle_l\,, \tag{5.5}$$

respectively, where $\langle s \rangle_k$ are the dynamic phasors of the switching function and are given by

$$\langle s \rangle_k = \begin{cases} D & k = 0 \\ \dfrac{1 - e^{-j2Dk\pi}}{j2k\pi} & \text{otherwise.} \end{cases} \tag{5.6}$$

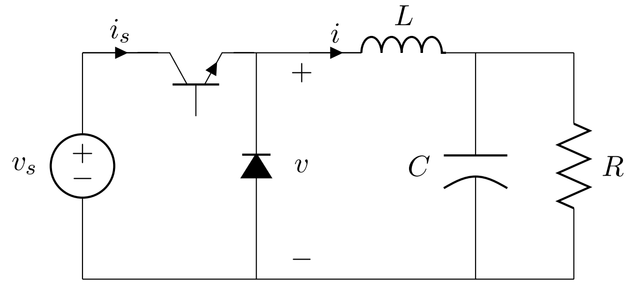

Figure 5.2: dc/dc step-down converter

The discrete dynamic phasor form of the dc/dc converter may be derived by substituting discrete quantities for the continuous quantities in (5.4) and (5.5). The discrete equations may then be used to simulate transient behaviour of the converter by simply allowing the discrete quantities to change over time. Therefore, an approximate discrete dynamic phasor model of the dc/dc converter may be derived using switching functions developed considering the steady state characteristics of the converter.

The switching function method enables dynamic phasor-based modeling of power electronic converters since it removes the decision making process typically used to analyze and simulate converters. Instead, converters are described in terms of periodic functions that may be converted to dynamic phasors. The disadvantage of this method is that the converter models are not as flexible as the decision-based device models. Switching functions are defined assuming that the switching devices in a converter are operated in a specific sequence, known as an operational mode [53]. In general, power electronic converters have a number of operational modes, depending on the conditions of the external system as well as the manner in which the converter is operated. However, the switching function developed for one operational mode may not be valid for any other modes. Therefore, converters modeled using the switching function method must be used in configurations such that they operate in modes that were considered in their development.

The dc/dc step-down converter illustrated in Figure 5.2 has two operational modes [53]. The first operational mode is continuous conduction mode, where either the switch or the diode are conducting at all times. The converter switching function given by (5.3) was developed assuming that the converter is operating in continuous conduction mode. However, it is possible for converter parameters to be selected such that the converter operates in discontinuous conduction mode, which is the second operational mode. A third state is introduced in discontinuous conduction mode where both the switch and diode are simultaneously off for a part of each period. In this situation, a new switching function would be required to reflect the third state introduced by the second operational mode.

5.2 Uncontrolled LCC with No Source Side Inductance

The first converter that will be considered is an LCC bridge constructed using diodes with no inductance on the ac-side of the converter ($L_s = 0$ in Figure 5.1). This topology will be used to demonstrate a number of important concepts in the development of a discrete dynamic phasor equivalent of the LCC for the general purpose simulation method developed in Chapter 3. Furthermore, the basic model developed in this section will be modified in later sections to include the effects of thyristors and source side inductance.

5.2.1 Steady State Operation

Analysis of the steady state characteristics of the LCC requires two primary assumptions. First of all, it is assumed that the dc-side current is approximately constant in steady state. This assumption is required to ensure that at least one device from both the upper (positive) and lower (negative) groups is conducting at all times [44]. Furthermore, it is assumed that both the ac-side voltage and current are balanced three phase quantities. This assumption is generally used to simplify the analysis of the steady state characteristics of the LCC. However, it restricts the dynamic phasor model developed in this work to studies involving balanced ac systems and disturbances.

The LCC shown in Figure 5.1 may be analyzed by considering the positive and negative diode groups separately. Figure 5.3 illustrates the positive dc terminal and diode group.

This circuit acts as a maximum-selection function, where the positive terminal voltage on the dc side is equal to the maximum of the three ac-side phase voltages [44]. The voltage at the positive terminal on the dc side of the converter is given by

$$v_p = \max\left(v_a, v_b, v_c\right) - R_{on} i_d, \tag{5.7}$$

where R_{on} is the on-state resistance of the diodes. Similarly, the negative diode group illustrated by Figure 5.4 selects the minimum of the three ac-side phase voltages. The voltage at the negative terminal on the dc side of the converter is given by

$$v_n = \min\left(v_a, v_b, v_c\right) - R_{on} i_d. \tag{5.8}$$

The terminal voltage on the dc side may be obtained by taking the difference between (5.7) and (5.8) as follows:

$$v_d = \max\left(v_a, v_b, v_c\right) - \min\left(v_a, v_b, v_c\right) - 2R_{on} i_d. \tag{5.9}$$

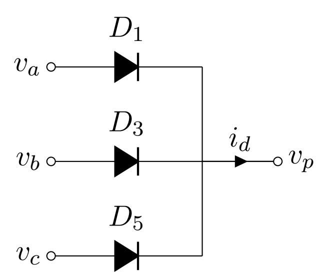

Figure 5.3: Positive group for the three phase LCC constructed using diodes

Figure 5.5 illustrates the dc-side voltages assuming that the ac-side voltages are sinusoidal and the on-state resistance of the diodes is negligible. This figure illustrates that the point at which the a-phase voltage becomes greater than the c-phase voltage is taken to be the reference point for the LCC waveforms [44]. This point in time coincides with the moment where D_1 in the positive diode group begins conduction. This point was taken as the reference because it coincides with the zero crossing of the v_{ac} line voltage, which is readily available in three phase systems. Therefore, this reference point simplifies the implementation of the discrete dynamic phasor LCC equivalent.

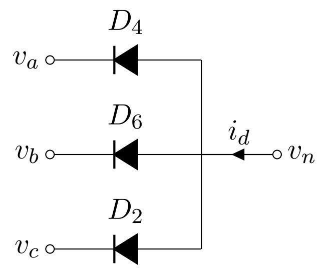

Figure 5.4: Negative group for the three phase LCC constructed using diodes

The dc-side voltage waveform, v_d, in Figure 5.5 illustrates that there are six identical intervals per period of the fundamental. Therefore, the average value of the dc-side voltage may be derived by considering a single interval [44]. The average value of the dc-side voltage is given by

$$V_d = \frac{3\sqrt{2}V_{LL}}{\pi}, \tag{5.10}$$

where V_{LL} is the RMS value of the ac-side line-to-line voltage. Figure 5.5 also includes labels indicating which diodes are conducting during each of the six intervals in the dc-side voltage. The a-phase ac-side line current shown in Figure 5.6 may be derived using the diode conduction information in Figure 5.5 assuming that the current leaving the dc side of the converter is constant and equal to I_d.

5.2.2 Switching Functions

The rectifier switching functions may be derived by considering the conduction patterns and waveforms illustrated in Figures 5.5 and 5.6. Table 5.1 summarizes the values of the dc-side voltages for each of the six intervals shown in Figure 5.5. This table shows that the dc-side voltage at every point in time is equal to a combination of the ac phase voltages, which can be expressed as one of three line voltages [44]. The dc-side voltage may be written as a single equation using the information in Table 5.1, which is given by

$$v_d = s_v\left(\theta\right) v_{ab} + s_v\left(\theta - {}^{2\pi}/_{3}\right) v_{bc} + s_v\left(\theta + {}^{2\pi}/_{3}\right) v_{ca} - R_d i_d, \tag{5.11}$$

where s_v is the dc-side voltage switching function and is given by

$$s_v(\theta) = \begin{cases} 1 & 0 \leq \theta < \pi/3 \\ -1 & \pi \leq \theta < 4\pi/3 \\ 0 & \text{otherwise} \end{cases} \tag{5.12}$$

and R_d is the total resistance between the ac and dc sides of the LCC. The value of this resistance for the diode LCC with no source side inductance is $2R_{on}$ as shown in (5.11).

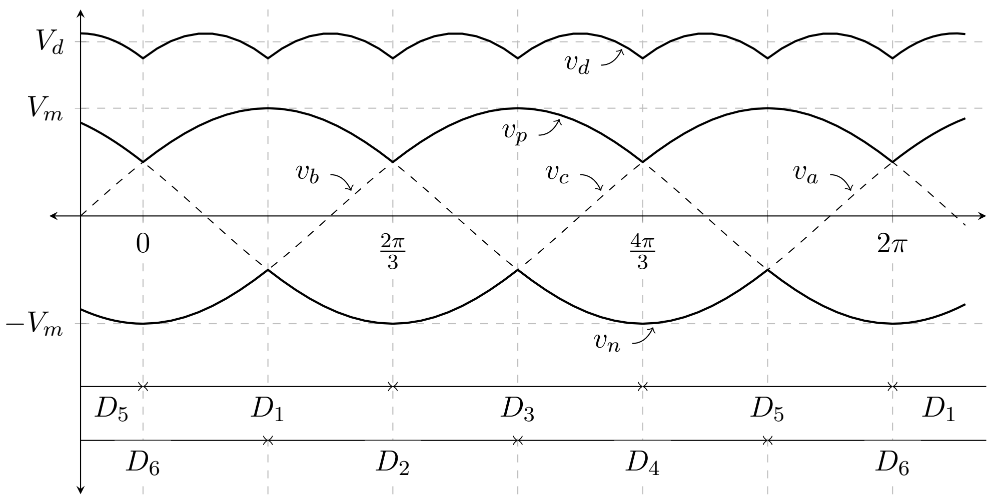

Figure 5.5: Voltage waveforms for the LCC constructed using diodes neglecting any source side inductance

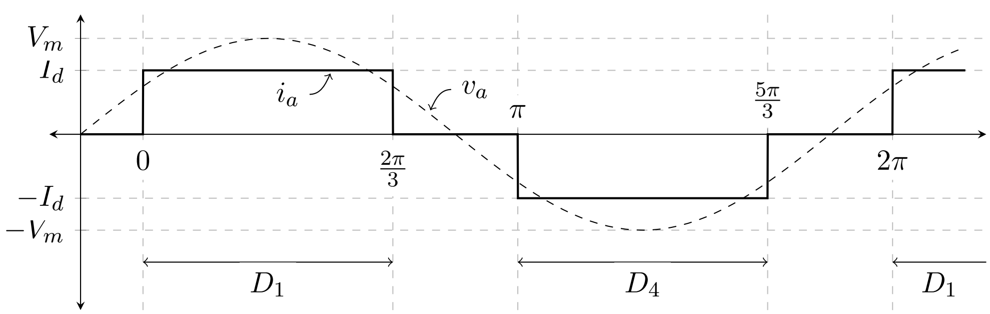

Figure 5.6: Line current waveform for the LCC constructed using diodes neglecting any source side inductance

Table 5.2 contains the values of the ac-side line currents over one period of the ac system fundamental frequency, which may be derived using the conduction information in Figure 5.5. The ac-side line currents may be written as individual expressions using the information in Table 5.2, which are given by

$$i_a = s_i(\theta)\, i_d; \tag{5.13}$$

$$i_b = s_i(\theta - {}^{2\pi}/_3)\, i_d; \text{ and} \tag{5.14}$$

$$i_c = s_i(\theta + {}^{2\pi}/_3)\, i_d, \tag{5.15}$$

where s_i is the ac-side current switching function and is given by

$$s_i(\theta) = \begin{cases} 1 & 0 \le \theta < {}^{2\pi}/_3 \\ -1 & \pi \le \theta < {}^{5\pi}/_3 \\ 0 & \text{otherwise.} \end{cases} \tag{5.16}$$

Table 5.1: dc-side voltages for each interval in the LCC cycle neglecting any source side inductance

Start	**End**	**Positive Diode**	**Negative Diode**	v_p	v_n	v_d
0	$\pi/3$	D_1	D_6	v_a	v_b	v_{ab}
$\pi/3$	$2\pi/3$	D_1	D_2	v_a	v_c	$-v_{ca}$
$2\pi/3$	π	D_3	D_2	v_b	v_c	v_{bc}
π	$4\pi/3$	D_3	D_4	v_b	v_a	$-v_{ab}$
$4\pi/3$	$5\pi/3$	D_5	D_4	v_c	v_a	v_{ca}
$5\pi/3$	2π	D_5	D_6	v_c	v_b	$-v_{bc}$

Table 5.2: ac-side line currents for each interval in the LCC cycle neglecting any source side inductance

Start	**End**	**Positive Diode**	**Negative Diode**	i_a	i_b	i_c
0	$\pi/3$	D_1	D_6	i_d	$-i_d$	0
$\pi/3$	$2\pi/3$	D_1	D_2	i_d	0	$-i_d$
$2\pi/3$	π	D_3	D_2	0	i_d	$-i_d$
π	$4\pi/3$	D_3	D_4	$-i_d$	i_d	0
$4\pi/3$	$5\pi/3$	D_5	D_4	$-i_d$	0	i_d
$5\pi/3$	2π	D_5	D_6	0	$-i_d$	i_d

5.2.3 Dynamic Phasor Model

The dynamic phasor form of the dc-side voltage equation may be derived by applying the dynamic phasor operator and multiplication property to (5.11), which yields:

$$\langle v_d \rangle_k = V_{dk} - R_d \langle i_d \rangle_k \,, \tag{5.17}$$

where V_{dk} is the equivalent dynamic phasor dc-side voltage source and is given by

$$V_{dk} = \sum_{l=-\infty}^{\infty} \langle s_v \rangle_{k-l} \left(\langle v_{ab} \rangle_l + e^{-j2(k-l)\pi/3} \langle v_{bc} \rangle_l + e^{j2(k-l)\pi/3} \langle v_{ca} \rangle_l \right) \tag{5.18}$$

The dynamic phasors of the dc-side voltage switching function, $\langle s_v \rangle_k$, are given by

$$\langle s_v \rangle_k = \begin{cases} 0 & k \text{ even} \\ \dfrac{e^{jk\phi}\left(1 - e^{-jk\pi/3}\right)}{jk\pi} & k \text{ odd,} \end{cases} \tag{5.19}$$

where ϕ is the phase angle of v_{ac}. The switching functions in Section 5.2.1 were derived using the point at which D_1 begins conduction as the reference point in the converter cycle. This point in time coincides with the positive zero crossing of v_{ac}. However, v_{ac} may be shifted relative to a universal reference point when the converter is interfaced to an ac system. The value of this shift is equal to the phase angle of v_{ac}, ϕ. Therefore, the switching functions and their dynamic phasors must also be shifted by ϕ as well to ensure that they coincide with the ac-side voltages.

Similarly, the dynamic phasor form of the ac side may be derived by applying the dynamic phasor operator and multiplication property to (5.13) to (5.15), which yields:

$$\langle i_a \rangle_k = I_{ak}; \tag{5.20}$$

$$\langle i_b \rangle_k = I_{bk}; \text{ and} \tag{5.21}$$

$$\langle i_c \rangle_k = I_{ck}, \tag{5.22}$$

where I_{ak}, I_{bk}, and I_{ck} are the equivalent dynamic phasor ac-side current sources and are given by

$$I_{ak} = \sum_{l=-\infty}^{\infty} \langle s_i \rangle_{k-l} \langle i_d \rangle_l \,; \tag{5.23}$$

$$I_{bk} = \sum_{l=-\infty}^{\infty} e^{-j2(k-l)\pi/3} \langle s_i \rangle_{k-l} \langle i_d \rangle_l \,; \text{ and} \tag{5.24}$$

$$I_{ck} = \sum_{l=-\infty}^{\infty} e^{j2(k-l)\pi/3} \langle s_i \rangle_{k-l} \langle i_d \rangle_l \,. \tag{5.25}$$

The dynamic phasors of the ac-side current switching function, $\langle s_i \rangle_k$, are given by

$$\langle s_i \rangle_k = \begin{cases} 0 & k \text{ even} \\ \dfrac{e^{jk\phi}\left(1 - e^{-j2k\pi/3}\right)}{jk\pi} & k \text{ odd.} \end{cases} \tag{5.26}$$

The dependence of the LCC switching functions on the angle of v_{ac} poses a problem to the dynamic phasor model since this value is not directly available in dynamic phasor-based simulations. This problem may be solved by assuming that ϕ is well approximated by the phase angle of $\langle v_{ac} \rangle_1$ [8], which may be calculated as follows:

$$\phi \approx \angle \langle v_{ac} \rangle_1 + \frac{\pi}{2}. \tag{5.27}$$

Equation (5.27) is an approximation because the phase angle of the time-domain ac-side voltages may not be equal to the phase angle of the fundamental component depending on the presence of harmonics. Furthermore, the additional $\pi/2$ in (5.27) is required since the phase angle of a dynamic phasor is measured relative to the real axis and as a result, represents the phase of a cosine waveform. However, ϕ was defined as the positive zero crossing of v_{ac}, which corresponds to the phase of a sine waveform. Therefore, the angle calculated from $\langle v_{ac} \rangle_1$ must be shifted by $\pi/2$ such that it represents the positive zero crossing of v_{ac}.

The equations given by (5.17) to (5.22) together with the approximation for ϕ given by (5.27) define the continuous steady state dynamic phasor form of the diode-based LCC. These equations suggest that in terms of dynamic phasors, the LCC appears as a set of coupled voltage and current sources [42]. The final step in obtaining a discrete dynamic phasor LCC model that may be included in the nodal analysis method is to convert the ac and dc equations to discrete Norton equivalents. However, the approximation given by (5.27) poses a significant problem for deriving a discrete form of the LCC. The equations for the switching functions are nonlinear functions of ϕ and as a consequence, they are nonlinear functions of $\langle v_a \rangle_1$ and $\langle v_c \rangle_1$. Therefore, approximations are required to derive a discrete dynamic phasor equivalent for the LCC that can be incorporated into nodal analysis-based simulations.

The method used in this work to derive a discrete dynamic phasor equivalent for the rectifier is to introduce a one time step delay between the LCC and the electrical network. This method is used in PSCAD/EMTDC to model nonlinear devices, such as synchronous machines, which use a time step delay between internal quantities and the network voltages [1]. The discrete dynamic phasor Norton equivalent for the dc side of the rectifier may be derived using (5.17) and the ac-sides voltages from the previous time step as follows:

$$\begin{aligned} \langle i_d \rangle_k [n] &= \frac{1}{R_d} \left(V_{dk} [n-1] - \langle v_d \rangle_k [n] \right) \\ &= I_{dk} [n-1] - G_d \langle v_d \rangle_k [n] , \end{aligned} \tag{5.28}$$

where G_d is the equivalent dc-side conductance. The discrete dc-side current source, $I_{dk} [n-1]$, is given by

$$\begin{aligned} I_{dk} [n-1] = G_d \sum_{l=-\infty}^{\infty} \langle s_v \rangle_{k-l} [n-1] \big(\langle v_{ab} \rangle_l [n-1] + \\ e^{-j2(k-l)\pi/3} \langle v_{bc} \rangle_l [n-1] + e^{j2(k-l)\pi/3} \langle v_{ca} \rangle_l [n-1] \big) , \end{aligned} \tag{5.29}$$

where the discrete form of the dc-side voltage switching function is given by

$$\langle s_v \rangle_k [n-1] = \begin{cases} 0 & k \text{ even} \\ \dfrac{e^{jk\phi[n-1]} \left(1 - e^{-jk\pi/3}\right)}{jk\pi} & k \text{ odd.} \end{cases} \tag{5.30}$$

The discrete form of the ac side of the converter may be derived by substituting the value of the dc-side current from the previous time step as follows:

$$\langle i_a \rangle_k [n] = I_{ak} [n-1] \, ; \tag{5.31}$$

$$\langle i_b \rangle_k [n] = I_{bk} [n-1] \, ; \text{ and} \tag{5.32}$$

$$\langle i_c \rangle_k [n] = I_{ck} [n-1] \, , \tag{5.33}$$

where the equivalent ac-side current sources are given by

$$I_{ak} [n-1] = \sum_{l=-\infty}^{\infty} \langle s_i \rangle_{k-l} [n-1] \langle i_d \rangle_l [n] \, ; \tag{5.34}$$

$$I_{bk} [n-1] = \sum_{l=-\infty}^{\infty} e^{-j2(k-l)\pi/3} \langle s_i \rangle_{k-l} [n-1] \langle i_d \rangle_l [n-1] \, ; \text{ and} \tag{5.35}$$

$$I_{ck} [n-1] = \sum_{l=-\infty}^{\infty} e^{j2(k-l)\pi/3} \langle s_i \rangle_{k-l} [n-1] \langle i_d \rangle_l [n-1] \, , \tag{5.36}$$

and the discrete form of the ac-side current switching function is given by

$$\langle s_i \rangle_k [n-1] = \begin{cases} 0 & k \text{ even} \\ \dfrac{e^{jk\phi[n-1]} \left(1 - e^{-j2k\pi/3}\right)}{jk\pi} & k \text{ odd.} \end{cases} \tag{5.37}$$

The ac side equations demonstrate that in terms of discrete dynamic phasors, the ac side appears as individual current sources for each phase. However, interfacing a current source that is based solely on values from the previous time step with the electrical network can lead to numerical instability, particularly in situations where the terminals of the device are suddenly exposed to an open circuit [1]. The method used in PSCAD/EMTDC to introduce models with this characteristic, such as the synchronous machine, into the electrical network is to include an additional numerical interfacing circuit. This circuit consists of a small conductance, G_a, in parallel with a compensating current source. Figure 5.7 illustrates the interfacing circuit in terms of dynamic phasors for the a-phase terminal of the discrete LCC model.

The value of the parallel conductance, G_a, may be selected as a small value relative to some base impedance associated with the LCC [1]. For example, if the LCC is modeled with a converter transformer, the base impedance of the transformer may be used to select an appropriate value for G_a. A more compact form of the a-phase terminal model illustrated in Figure 5.7 may be derived by combining the compensating source with the LCC source. The two individual current sources may be combined and expressed as a single source, which is given by

$$I'_{ak}[n-1] = I_{ak}[n-1] - G_a \langle v_a \rangle_k [n-1]. \tag{5.38}$$

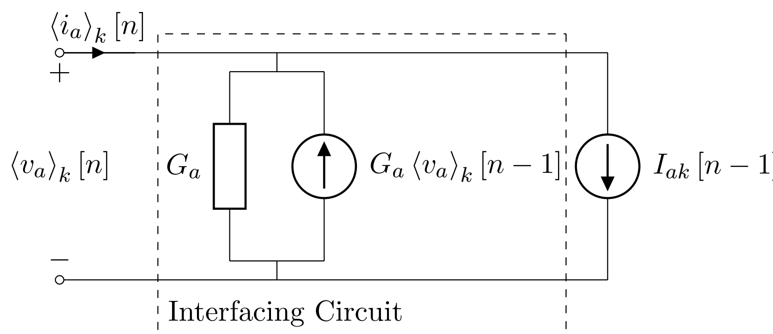

Figure 5.7: Interfacing circuit for the a-phase ac port of the discrete dynamic phasor LCC model

Figure 5.8 illustrates the final form of the discrete dynamic phasor LCC model, including the interfacing requirements for the ac network.

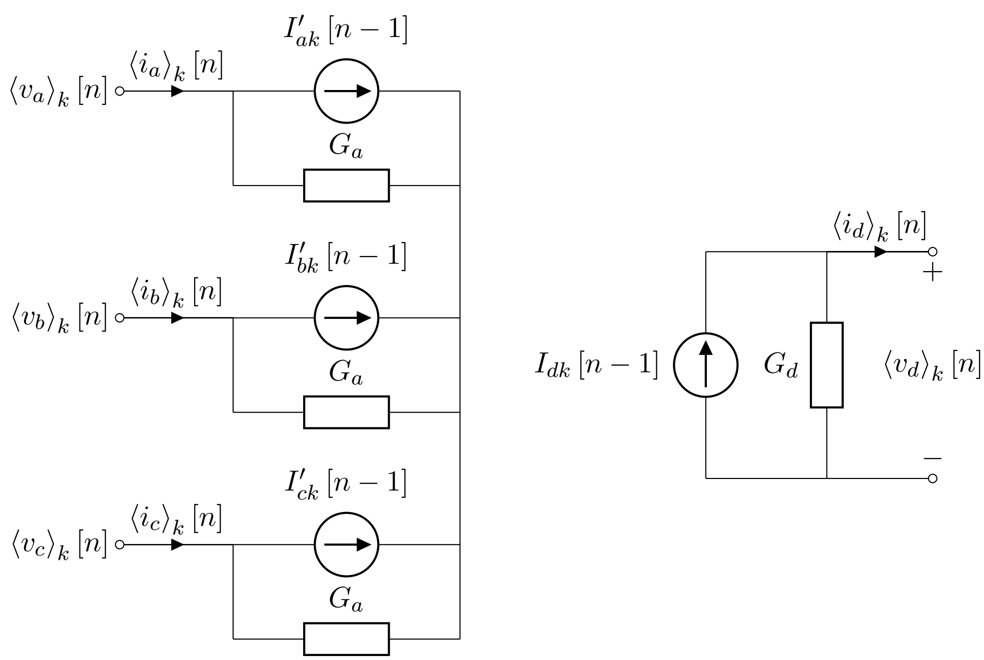

Figure 5.8: Discrete dynamic phasor equivalent model for the LCC

5.3 Controlled LCC with No Source Side Inductance

The second converter that will be considered is an LCC bridge constructed using thyristors with no inductance on the ac side. The following section begins with an examination of the steady state operating characteristics of the thyristor based LCC. Following this, the LCC model developed in Section 5.2.3 will be modified to account for the differences between diode and thyristor based LCCs. This includes a discussion on the modifications of the switching functions to incorporate the effects of the thyristors as well as the addition of two control system models required to properly capture the dynamics of LCCs.

5.3.1 Steady State Operation

The operation of the thyristor-based LCC is similar to the diode-based LCC, except that the point at which conduction begins for each device may be delayed [44]. The amount of time that conduction is delayed may be expressed as an angle and is known as the firing angle, α. Figure 5.9 illustrates the modified positive and negative terminal voltages, along with the total dc-side voltage and the ac-side phase voltages. It is important to note that the reference point has been shifted such that it coincides with the moment where T_1 in the positive group begins conduction.

The plots show that the positive and negative terminal voltages no longer track the maximum and minimum phase voltages. Instead, the dc-side voltages track the phase voltage whose thyristors are involved in conduction of the dc-side current. The average value of the dc-side voltage may once again be determined by examining a single interval of the dc-side voltage waveform shown in Figure 5.9 [44] and is given by

$$V_d = \frac{3\sqrt{2}V_{LL}\cos(\alpha)}{\pi}. \tag{5.39}$$

Figure 5.10 illustrates the a-phase ac-side line current, which is based on the thyristor conduction information in Figure 5.9. This waveform illustrates that the thyristors shift the ac-side line currents to the right due to the delay effect of the firing angle, but do not change the shape of the line current waveforms.

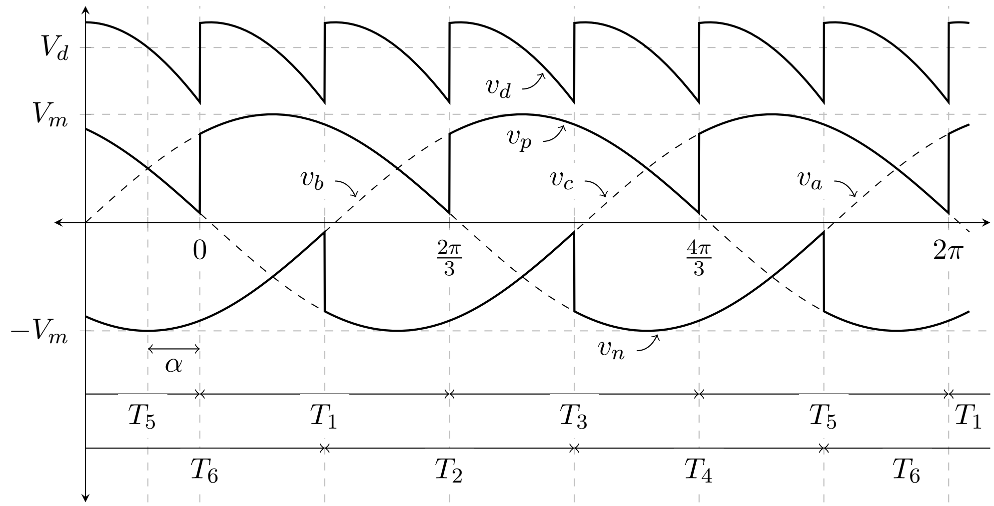

Figure 5.9: Voltage waveforms for the LCC constructed using thyristors neglecting any source side inductance

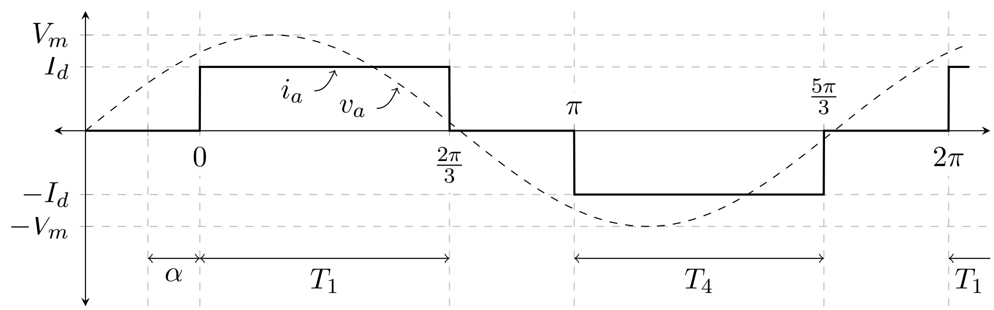

Figure 5.10: Line current waveform for the LCC constructed using thyristors neglecting any source side inductance

5.3.2 Switching Function Modification

The discrete dynamic phasor equivalent for the LCC illustrated by Figure 5.8 may be used to model the thyristor based LCC as well with a few modifications. The waveforms in Figures 5.9 and 5.10 demonstrate that the thyristors delay the conduction patterns of the LCC bridge by the value of the firing angle. The delay introduced by the thyristors was accounted for in Figures 5.9 and 5.10 by a rightward shift of the reference point. The voltage and current switching functions for the diode bridge derived in Section 5.2.3 include a term to account for the phase angle of the ac-side voltages. This term was included to account for the relative shift of the reference point due to the phase shift of the ac terminals to a universal reference point of the entire system. Therefore, the additional phase shift introduced by the the thyristor firing angle may be included in the switching functions using the angle of the ac-side voltages. The discrete dynamic phasors of the dc-side voltage switching function for the thyristor based LCC may be derived by adjusting (5.30) as follows:

$$\langle s_v \rangle_k [n-1] = \begin{cases} 0 & k \text{ even} \\ \dfrac{e^{jk(\phi[n-1]-\alpha[n-1])}\left(1-e^{-jk\pi/3}\right)}{jk\pi} & k \text{ odd.} \end{cases} \tag{5.40}$$

Similarly, the discrete dynamic phasors of the ac-side current switching function for the thyristor based LCC may be derived by adjusting (5.37) as follows:

$$\langle s_i \rangle_k [n-1] = \begin{cases} 0 & k \text{ even} \\ \dfrac{e^{jk(\phi[n-1]-\alpha[n-1])}\left(1-e^{-j2k\pi/3}\right)}{jk\pi} & k \text{ odd.} \end{cases} \tag{5.41}$$

5.3.3 Phase Locked Loop

The value of the firing angle is measured relative to the phase angle of the ac-side voltages. Therefore, a measurement of the ac system angle is required to ensure that the thyristor gate signals are issued at the correct time [47]. The instantaneous angle of the ac system is measured using a PLL. Figure 5.11 illustrates the Transvektor PLL, which is used in PSCAD/EMTDC to model power electronic converters [45, 47]. The output of this device is a sawtooth waveform whose value is equal to the instantaneous angle of the a-phase input signal.

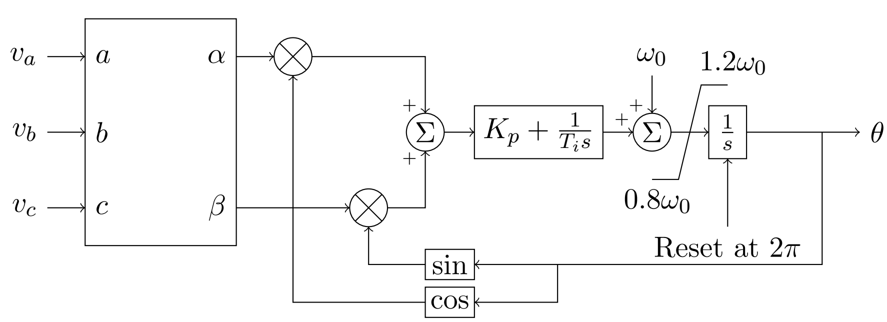

Figure 5.11: Transvektor PLL for time-domain simulation

Diode-based LCCs do not require a PLL since the diodes change status based entirely on the conditions imposed by the external system. As a result, the angle calculated using (5.27) could be used directly by the diode-based LCC switching functions without modification.

However, Figure 5.11 illustrates that the PLL is a dynamic control device with transient characteristics that must be captured to ensure accurate simulation of the thyristor-based PLL. Therefore, additional components are required in the dynamic phasor equivalent of the thyristor-based LCC to properly account for the dynamics introduced by the PLL.

The transient characteristics of the PLL may be captured in the dynamic phasor LCC model using the second control modeling method discussed in Section 4.1. Figure 5.12 illustrates an equivalent control system that may be used to model the dynamic characteristics of the Transvektor PLL [20, 48]. The input to this control system is the phase angle of the ac system, which is calculated using (5.27). The output of this system reflects the transient behaviour of the Transvektor PLL and is used by (5.40) and (5.41) in the thyristor-based LCC model.

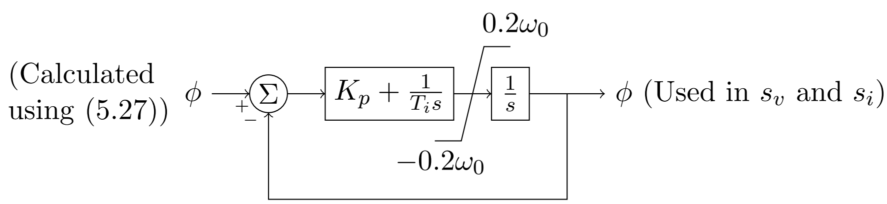

Figure 5.12: Transvektor PLL for dynamic phasor simulation

5.3.4 Thyristor Dead Time

The process of switching devices on and off in power electronic converters takes a finite amount of time. For example, the gate signals for the thyristors in LCCs are issued every $\pi/3$ radians. Furthermore, a thyristor cannot change status until a gate signal is issued to the next thyristor in the conduction sequence [51]. Therefore, any changes in the firing angle are not registered by the LCC until the next possible gate signal is issued. The time delay between a change in the firing angle and when the change is reflected by the LCC output is known as the thyristor dead time.

The dynamic phasor LCC model represents the relationship between the ac and dc sides using continuous switching functions. As a consequence, the effects of the thyristor dead time are not captured in the switching function equations. The thyristor dead time may be included in the dynamic phasor LCC model using a constant time delay block as shown in Figure 5.13. However, the dead time is a random value that depends on the time and value of the change in firing angle [51]. Therefore, an approximation is required to model the thyristor dead time as a constant time delay component.

$$\text{(From external model) } \alpha \longrightarrow \boxed{e^{sT_d}} \longrightarrow \alpha \text{ (Used in } s_v \text{ and } s_i\text{)}$$

Figure 5.13: Time delay system used to model thyristor dead time

A common method for modeling the dead time using a constant time delay is to assume that the dead time is a uniformly distributed random variable [51]. The expected value of the thyristor dead time is then used as the value for the time delay in Figure 5.13. The situation with the shortest delay occurs when a change in firing angle takes place immediately before a gate signal will be issued. In this situation, the thyristor dead time is equal to approximately zero. On the other hand, the situation with the longest delay occurs when a change in firing angle takes place immediately after a gate signal has been issued. In this situation, the thyristor dead time is equal to approximately $\pi/3$ radians. Therefore, the expected value for thyristor dead time in LCCs is $\pi/6$ radians.

5.4 Controlled LCC with a Source Side Inductance

The final converter that will be considered is an LCC bridge constructed using thyristors with an inductance on the ac side, which is the converter topology represented in Figure 5.1. This LCC model is more realistic than the models discussed in previous sections since the ac side generally includes some form of inductance [44]. The ac-side line current waveforms shown in previous sections illustrate that conduction of the dc-side current changes between phases instantaneously when no source side inductance is present. However, any inductance present on the ac side prevents an instantaneous change in the ac-side line currents. Therefore, the source side inductance introduces a finite period of time where conduction of the dc-side current changes between phases, which is known as the commutation or overlap angle, μ. The following section will begin with an examination of the effects of the source side inductance on the steady state operating characteristics. Following this, the switching function modifications required to incorporate the source side inductance will be discussed.

5.4.1 Steady State Operation

Figure 5.14 illustrates the commutation interval where the a-phase positive group thyristor, T_1, is taking over conduction of the dc-side current from the c-phase positive group thyristor, T_5 [44]. The negative group during this interval is conducting normally through the b-phase thyristor, T_6. The reference point from Section 5.3.1 is also used in this section such that this commutation interval begins at $\theta = 0$.

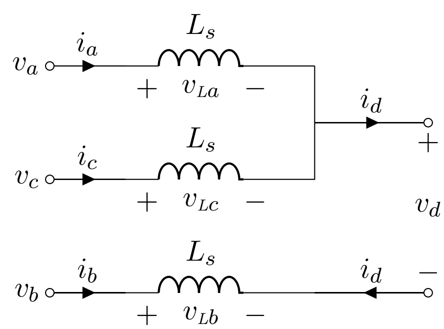

Figure 5.14: Thyristor configuration during commutation of T_5 into T_1

The ac-side line current and dc-side voltage during commutation may be determined using the circuit illustrated by Figure 5.14. The on-state resistance of the thyristors was temporarily neglected to simplify the following analysis of the ac-side line current. The Kirchoff's voltage law (KVL) equation about the loop containing T_1 and T_5 is given by

$$v_a - v_{La} + v_{Lc} - v_c = 0 \tag{5.42}$$

and the a and c-phase line currents are related to the dc-side current as follows:

$$i_a + i_c = i_d. \tag{5.43}$$

Assuming that the dc-side current is approximately constant and taking the derivative of (5.43) yields:

$$\frac{di_a}{d\theta} + \frac{di_c}{d\theta} = 0$$
$$\frac{v_{La}}{X_s} + \frac{v_{Lc}}{X_s} = 0$$

$$v_{La} = -v_{Lc}, \tag{5.44}$$

where X_s is the source side reactance of the converter and is equal to $\omega_0 L_s$. Substituting (5.44) into (5.42) and simplifying yields:

$$\frac{di_a}{d\theta} = \frac{v_{ac}}{2X_s}. \tag{5.45}$$

Assuming that the ac-side voltages are approximately sinusoidal and taking the integral of (5.45) yields:

$$i_a(\theta) = \frac{\sqrt{3}V_m}{2X_s}\left(\cos(\alpha) - \cos(\theta + \alpha)\right). \tag{5.46}$$

An equation for the overlap or commutation angle may be obtained using the fact that the a-phase current must be equal to the dc-side current when the commutation interval is complete [44]. Substituting $i_a(\mu) = i_d$ into (5.46) and solving for μ yields:

$$\mu = \cos^{-1}\left(\cos(\alpha) - \frac{\sqrt{2}X_s i_d}{V_{LL}}\right) - \alpha. \tag{5.47}$$

An alternative form of the a-phase line current equation that is convenient for definition of the ac-side current switching function may be derived by combining (5.46) and (5.47), which is given by

$$i_a(\theta) = i_d \frac{\cos(\alpha) - \cos(\theta + \alpha)}{\cos(\alpha) - \cos(\alpha + \mu)}. \tag{5.48}$$

The c-phase line current may be derived by substituting (5.48) into (5.43), which is given by

$$i_c(\theta) = i_d \frac{\cos(\theta + \alpha) - \cos(\alpha + \mu)}{\cos(\alpha) - \cos(\alpha + \mu)}. \tag{5.49}$$

The dc-side voltage may be derived using the positive and negative terminal voltage method used in Section 5.2.1. The voltage at the positive terminal on the dc side of the converter including the on-state resistance of the thyristors during commutation is given by

$$v_p = \frac{v_a + v_c}{2} - \frac{R_{on}}{2} i_d \tag{5.50}$$

and the voltage at the negative terminal on the dc side of the converter is given by

$$v_n = v_b - R_{on} i_d. \tag{5.51}$$

Taking the difference between (5.50) and (5.51) and simplifying gives the dc-side voltage in terms of the ac-side line voltages [46] as follows:

$$v_d = \frac{1}{2}\left(v_{ab} - v_{bc}\right) - \frac{3}{2} R_{on} i_d. \tag{5.52}$$

Figure 5.15 illustrates the dc-side voltages for the thyristor-based LCC with a nonzero source side inductance. These waveforms illustrate that the source side inductance causes a drop in the positive and negative terminal voltages during commutation, which decreases the effective voltage that appears across the dc terminals of the LCC [44]. This effect may be seen in the expression for the average value of the dc-side voltage, which is given by

$$V_d = \frac{3\sqrt{2} V_{LL} \cos(\alpha)}{\pi} - \frac{3 X_s I_d}{\pi}. \tag{5.53}$$

The magnitudes of the harmonics present in the dc-side voltage may be determined using a single interval of the v_d waveform shown in Figure 5.15 and are given by

$$V_k = \begin{cases} \frac{3\sqrt{2} V_{LL} \left| k \sin(\alpha) - j \cos(\alpha) + e^{-jk\mu}\left(k \sin(\alpha+\mu) - j \cos(\alpha+\mu)\right)\right|}{\pi (k^2 - 1)} & k = 6, 12, 18, \ldots \\ 0 & \text{otherwise.} \end{cases} \tag{5.54}$$

Figure 5.15 illustrates the a-phase ac-side line current over one cycle of the fundamental. This waveform illustrates the overlap effect that is introduced by the source side inductance [44]. The magnitudes of the harmonics in present in the ac-side line currents may be calculated using the waveform shown in Figure 5.15 and are given by

$$I_k = \begin{cases} \dfrac{2\sqrt{3} I_d \left|\beta_{k1} + \beta_{k2}\right|}{\pi\left(\cos(\alpha) - \cos(\alpha + \mu)\right)} & k = 1, 5, 7, 11, 13, \ldots \\ 0 & \text{otherwise,} \end{cases} \tag{5.55}$$

where

$$\beta_{k1} = \frac{\cos(\alpha) - e^{-jk\mu}\cos(\alpha+\mu)}{k}; \text{ and} \tag{5.56}$$

$$\beta_{k2} = \begin{cases} \frac{e^{-j\alpha}\left(e^{-j2\mu}-1\right)-j2\mu e^{j\alpha}}{4} & k=1 \\ \frac{k\cos(\alpha)+j\sin(\alpha)-e^{-jk\mu}(k\cos(\alpha+\mu)+j\sin(\alpha+\mu))}{1-k^2} & \text{otherwise.} \end{cases} \tag{5.57}$$

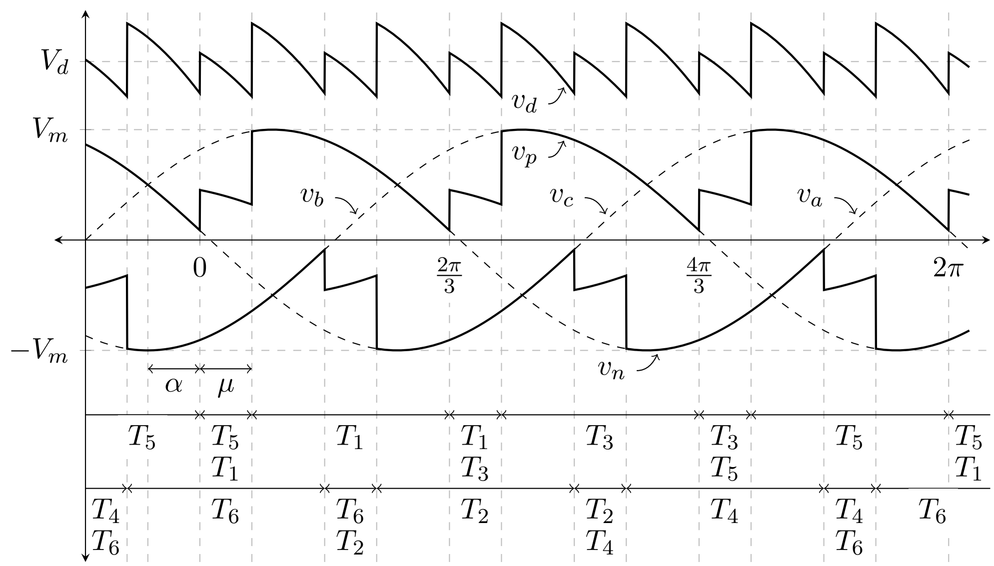

Figure 5.15: Voltage waveforms for the LCC constructed using thyristors including the effect of a source side inductance

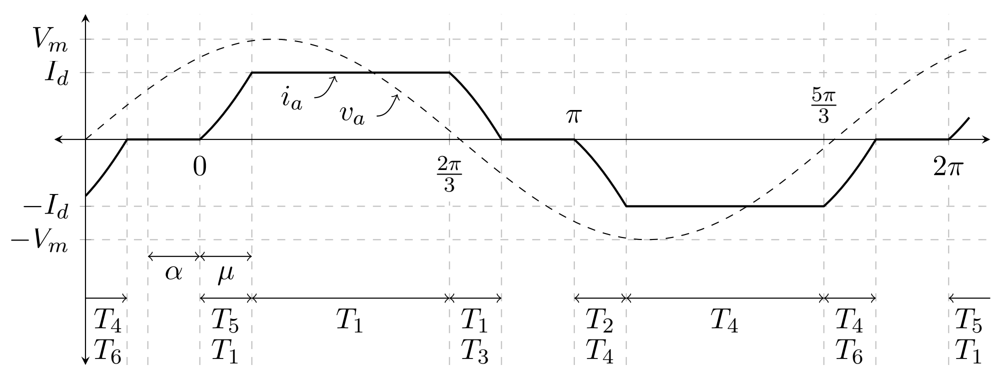

Figure 5.16: Line current waveform for the LCC constructed using thyristors including the effect of a source side inductance

5.4.2 Switching Function Modification

The previous section demonstrated that the presence of a source side inductance changes the conduction pattern of the thyristors. Therefore, the source side inductance may be incorporated into the dynamic phasor LCC model by modifying the voltage and current switching functions. Table 5.3 gives the positive, negative, and dc terminal voltages in terms of the ac-side phase voltages over one period of the ac system fundamental frequency. The modified LCC voltage switching function that includes the effects of an inductance on the ac side of the converter may be derived using the information in Table 5.3, which is given by

$$s_v(\theta) = \begin{cases} \frac{1}{2} & 0 \le \theta < \mu \quad \text{and} \quad \frac{\pi}{3} \le \theta < \frac{\pi}{3} + \mu \\ 1 & \frac{\pi}{3} + \mu \le \theta < \frac{2\pi}{3} \\ -\frac{1}{2} & \pi \le \theta < \pi + \mu \quad \text{and} \quad \frac{4\pi}{3} \le \theta < \frac{4\pi}{3} + \mu \\ -1 & \frac{4\pi}{3} + \mu \le \theta < \frac{5\pi}{3} \\ 0 & \text{otherwise.} \end{cases} \tag{5.58}$$

Table 5.3: dc-side voltages for each interval in the LCC cycle including the effect of a source side inductance

Start	**End**	**Positive Thyristors**	**Negative Thyristors**	v_p	v_n	v_d
0	μ	T_1, T_5	T_6	$(v_a+v_c)/2$	v_b	$(v_{ab}-v_{bc})/2$
μ	$\pi/3$	T_1	T_6	v_a	v_b	v_{ab}
$\pi/3$	$\pi/3+\mu$	T_1	T_2, T_6	v_a	$(v_b+v_c)/2$	$(v_{ab}-v_{ca})/2$
$\pi/3+\mu$	$2\pi/3$	T_1	T_2	v_a	v_c	$-v_{ca}$
$2\pi/3$	$2\pi/3+\mu$	T_1, T_3	T_2	$(v_a+v_b)/2$	v_c	$(v_{bc}-v_{ca})/2$
$2\pi/3+\mu$	π	T_3	T_2	v_b	v_c	v_{bc}
π	$\pi+\mu$	D_3	T_2, T_4	v_b	$(v_a+v_c)/2$	$(v_{bc}-v_{ab})/2$
$\pi+\mu$	$4\pi/3$	T_3	T_4	v_b	v_a	$-v_{ab}$
$4\pi/3$	$4\pi/3+\mu$	T_3, T_5	T_4	$(v_b+v_c)/2$	v_a	$(v_{ca}-v_{ab})/2$
$4\pi/3+\mu$	$5\pi/3$	T_5	T_4	v_c	v_a	v_{ca}
$5\pi/3$	$5\pi/3+\mu$	T_5	T_4, T_6	v_c	$(v_a+v_b)/2$	$(v_{ca}-v_{bc})/2$
$5\pi/3+\mu$	2π	T_5	T_6	v_c	v_b	$-v_{bc}$

The discrete form of the dynamic phasors for the dc-side voltage switching function may be derived by applying the dynamic phasor operator and time step delay method discussed in Section 5.2.3 and are given by

$$\langle s_v \rangle_k [n-1] = \begin{cases} \dfrac{e^{jk(\phi[n-1]-\alpha[n-1])}\left(1-e^{-jk\pi/3}\right)\left(1+e^{-jk\mu[n-1]}\right)}{j2k\pi} & k \text{ odd} \\ 0 & k \text{ even.} \end{cases} \tag{5.59}$$

The expression given by (5.59) shows that the dc-side voltage switching function is dependent on the commutation angle, which may be calculated using (5.47). It was assumed in Section 5.4.1 that the dc-side current is approximately constant and that the ac-side voltages are approximately sinusoidal. In terms of dynamic phasors, these assumptions imply that the dc-side current must be dominated by its dc ($k = 0$) component and that the ac-side voltages must be dominated by their fundamental ($k = 1$) component. Therefore, (5.47) may be expressed in terms of dynamic phasors as follows:

$$\mu [n-1] = \cos^{-1}\left(\cos(\alpha) - \frac{X_s \langle i_d \rangle_0 [n-1]}{|\langle v_{ac} \rangle_1 [n-1]|}\right) - \alpha. \tag{5.60}$$

The expression given by (5.52) reveals that the total resistance between the ac and dc sides (R_d) of the LCC is time dependent when an inductance is present on the ac side of the converter. It was shown in Section 5.2.2 that R_d is equal to $2R_{on}$ when one device in each group is conducting. However, (5.52) illustrates that R_d is equal to $^3/_2 R_{on}$ during commutation. The time dependence of R_d may be modeled using a switching function using the same method as the dc-side voltage and ac-side line currents. However, a switching function for R_d would be a function of the ac system angle, thyristor firing angle, and commutation angle since the values of R_d depend on the configuration of the LCC. The discrete form of a switching function that is dependent on these quantities requires the time delay method discussed in Section 5.2.3. Therefore, the product of R_d and i_d would appear as a current source rather than the equivalent resistance for the dc-side discrete Norton equivalent.

This approach for handling the time dependent dc-side resistance would require modifications to the dc side of the converter model used in the previous sections. Alternatively, the original model may be used if the time dependence of the dc-side resistance is simply ignored. In general, the voltage drop across R_d is negligible compared to the magnitude of the dc-side voltage. Therefore, the change in the voltage drop across R_d may be considered negligible and R_d may be modeled as a constant resistance that is equal to $2R_{on}$. The dc side of the LCC with a nonzero source side inductance may be modeled by simply substituting the dc-side voltage switching function dynamic phasors given by (5.59) into the dynamic phasor LCC model shown in Section 5.2.3 using this assumption.

Table 5.4 gives the ac-side line currents during each conduction interval for the LCC with a nonzero source side inductance. The variables i_{on} and i_{off} were used to denote the current in the thyristors during commutation that are beginning and ceasing conduction, respectively. Expressions for i_{on} and i_{off} during each interval may be derived using the method shown in Section 5.4.1. The LCC ac-side current switching function for the a-phase line current may be derived using the information in Table 5.4, and is given by

$$s_i(\theta) = \begin{cases} \dfrac{\cos(\alpha) - \cos(\theta + \alpha)}{\cos(\alpha) - \cos(\alpha + \mu)} & 0 \le \theta < \mu \\ 1 & \mu \le \theta < 2\pi/3 \\ \dfrac{\cos(\theta - 2\pi/3 + \alpha) - \cos(\alpha + \mu)}{\cos(\alpha) - \cos(\alpha + \mu)} & 2\pi/3 \le \theta < 2\pi/3 + \mu \\ \dfrac{\cos(\theta - \pi + \alpha) - \cos(\alpha)}{\cos(\alpha) - \cos(\alpha + \mu)} & \pi \le \theta < \pi + \mu \\ -1 & \pi + \mu \le \theta < 5\pi/3 \\ \dfrac{\cos(\alpha + mu) - \cos(\theta - 5\pi/3 + \alpha)}{\cos(\alpha) - \cos(\alpha + \mu)} & 2\pi/3 \le \theta < 2\pi/3 \le \theta < 5\pi/3 + \mu \\ 0 & \text{otherwise.} \end{cases} \tag{5.61}$$

Applying the dynamic phasor operator and delay method to (5.61) yields the dynamic phasors of the LCC ac-side current switching function, which are given by

$$\langle s_i \rangle_k [n-1] = \begin{cases} \dfrac{e^{jk(\phi[n-1] - \alpha[n-1])} \left(1 - e^{-j2k\pi/3}\right) \left(\beta_{k1}[n-1] + \beta_{k2}[n-1]\right)}{j\pi \left(\cos(\alpha[n-1]) - \cos(\alpha[n-1] + \mu[n-1])\right)} & k \text{ odd} \\ 0 & k \text{ even,} \end{cases} \tag{5.62}$$

where $\beta_{k1}[n-1]$ and $\beta_{k2}[n-1]$ are the constants given by (5.56) and (5.57), respectively, with discrete variables substituted into the expressions for α and μ. The dynamic phasors given by (5.62) may be used directly in the ac side of the discrete LCC model discussed in Section 5.2.3.

Table 5.4: ac-side line currents for each interval in the LCC cycle including the effect of a source side inductance

Start	**End**	**Positive Thyristors**	**Negative Thyristors**	i_a	i_b	i_c
0	μ	T_1, T_5	T_6	i_{on}	$-i_d$	i_{off}
μ	$\pi/3$	T_1	T_6	i_d	$-i_d$	0
$\pi/3$	$\pi/3+\mu$	T_1	T_2, T_6	i_d	$-i_{off}$	$-i_{on}$
$\pi/3+\mu$	$2\pi/3$	T_1	T_2	i_d	0	$-i_d$
$2\pi/3$	$2\pi/3+\mu$	T_1, T_3	T_2	i_{off}	i_{on}	$-i_d$
$2\pi/3+\mu$	π	T_3	T_2	0	i_d	$-i_d$
π	$\pi+\mu$	T_3	T_2, T_4	$-i_{on}$	i_d	$-i_{off}$
$\pi+\mu$	$4\pi/3$	T_3	T_4	$-i_d$	i_d	0
$4\pi/3$	$4\pi/3+\mu$	T_3, T_5	T_4	$-i_d$	i_{off}	i_{on}
$4\pi/3+\mu$	$5\pi/3$	T_5	T_4	$-i_d$	0	i_d
$5\pi/3$	$5\pi/3+\mu$	T_5	T_4, T_6	$-i_{off}$	$-i_{on}$	i_d
$5\pi/3+\mu$	2π	T_5	T_6	0	$-i_d$	i_d

The modifications developed in this section to include the effects of commutation impose two important constraints on the discrete dynamic phasor equivalent of the LCC. First of all, the switching function modifications were derived assuming that the commutation angle does not exceed $\pi/3$. This assumption restricts the LCC model to a single operational mode in which the converter spends part of each cycle in commutation and the other part conducting normally using one device from each group. However, it can be shown that there are several different operational modes that depend on the size of the source side inductance, the ac-side voltage, and the dc-side current [46, 53]. Therefore, the LCC model developed in this section is restricted to systems where the commutation angle does not exceed $\pi/3$.

The second constraint that the modifications impose on the LCC model is that they limit the size of any additional series inductance on the ac side of the converter. This section demonstrated that the dynamic phasor LCC model including a source side inductance requires knowledge of the size of the inductance to properly incorporate its effects. Therefore, any additional series inductance included on the ac side of the LCC must be small in comparison to the converter source side inductance to ensure that it does not significantly impact the dynamic characteristics of the converter.

5.5 Simulation Results

Figure 5.17 illustrates the example circuit that will be used to demonstrate the dynamic phasor LCC model. The LCC is connected to a strong ac system, which is represented using a sinusoidal source with a small series resistance. The load is modeled using a passive RL circuit, where the resistance and inductance are chosen such that it filters the majority of the dc-side harmonics and appears as a constant current load. Table 5.5 contains all of the circuit parameters for the test system shown in Figure 5.17.

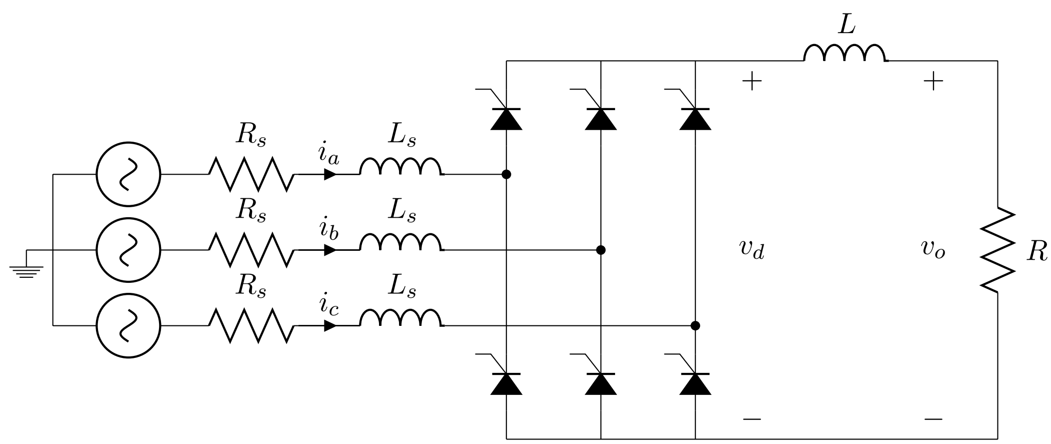

Figure 5.17: LCC connected to a strong ac system and passive dc load

Table 5.5: LCC test system parameters

Parameter	**Value**
f_0	60 Hz
V_{LL}	230 kV
R_{on}	10 mΩ
R_s	1 mΩ
R	10 Ω
L_s	2 mH
L	0.1 H

Tables 5.6 and 5.7 contain the steady state magnitudes of select harmonics for the dc-side voltage, v_d, and the ac-side line current, i_a, respectively. The analytical values

were calculated using (5.53) to (5.55) and the dynamic phasor values were obtained using simulations. The magnitudes of the harmonics obtained from PSCAD/EMTDC simulations were also included for comparison. The firing angle of the thyristors was set to 5° for all of the values shown in Tables 5.6 and 5.7. The data demonstrates that the analytical and simulation results are in good agreement.

Table 5.6: Steady state dc-side voltage harmonics (all values in kV)

Harmonic	**Analytical**	**Dynamic Phasors**	**PSCAD/EMTDC**
0	288.59	288.01	287.77
6	27.02	27.01	25.97
12	13.70	13.67	13.33
18	9.54	9.54	9.14

Table 5.7: Steady state ac-side line current harmonics (all values in kA)

Harmonic	**Analytical**	**Dynamic Phasors**	**PSCAD/EMTDC**
1	31.60	31.54	31.63
5	5.34	5.27	5.35
7	3.20	3.19	3.13
11	1.15	1.13	1.11
13	0.66	0.66	0.65
17	0.36	0.35	0.37
19	0.35	0.35	0.35

Figure 5.18 illustrates the average value and magnitude of the sixth harmonic of the dc-side voltage, v_d, over firing angles from 5° to 85°. These plots include the analytical results along with the dynamic phasor and PSCAD/EMTDC results for comparison. Figure 5.18a illustrates that all three methods are in good agreement for the average value of the load voltage. Figure 5.18b illustrates that all three methods are in good agreement for the sixth harmonic for smaller firing angles. However, the PSCAD/EMTDC results appear to diverge from the analytical and dynamic phasor results as firing angle increases. This error may be attributed to the load used to model the dc side of the test system shown in Figure 5.17. The analytical equations and dynamic phasor model are both based on the assumption that the dc-side current is approximately constant and dominated by its dc component. However, the RL load shown in the test system will respond to the harmonics present in the LCC dc-side voltage. Figure 5.18 demonstrates that the harmonics present in the dc-side voltage

begin to dominate as the firing angle is increased, which in turn increases the harmonics present in the dc-side current. Therefore, the constant dc-side current assumption used to derive the analytical equations and create the dynamic phasor LCC model begins to break down as the firing angle is increased for the test system.

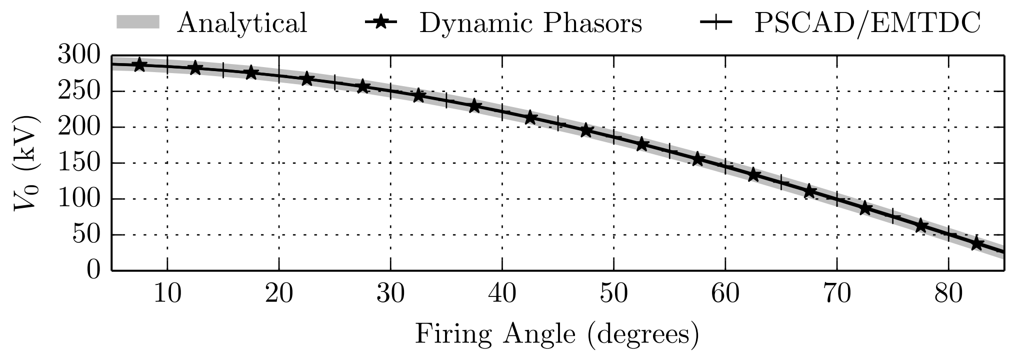

(a) Average value

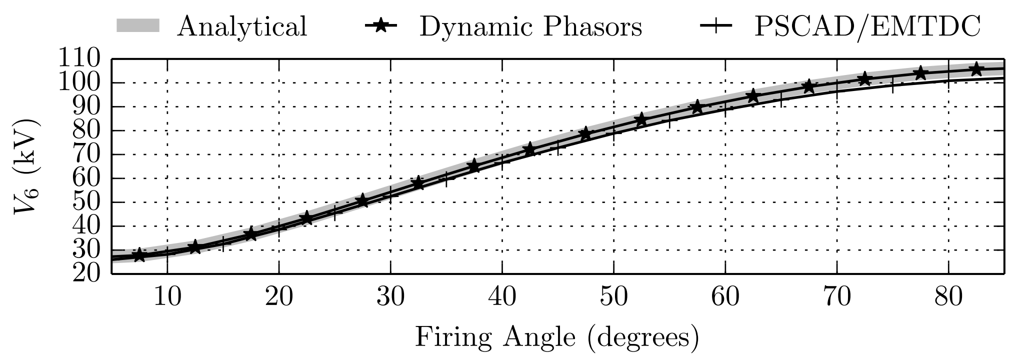

(b) Sixth harmonic

Figure 5.18: Comparison of the dc-side voltage harmonics for various firing angles between 5° to 85°

Figure 5.19 illustrates the magnitude of the fundamental and fifth harmonic of the ac-side line current over firing angles from 5° to 85° respectively. These plots include the analytical results along with the dynamic phasor and PSCAD/EMTDC results for comparison. Figure 5.19a illustrates that the three methods are in good agreement for the fundamental component, with some error between the dynamic phasor and PSCAD/EMTDC results as the firing angle increases. Figure 5.19b illustrates that all three sets of simulation results follow the same trends, with a small amount of error between the methods for all firing angles.

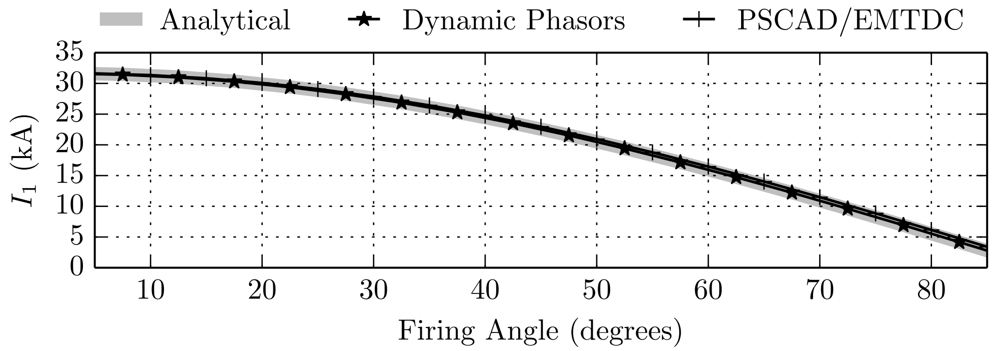

(a) Fundamental

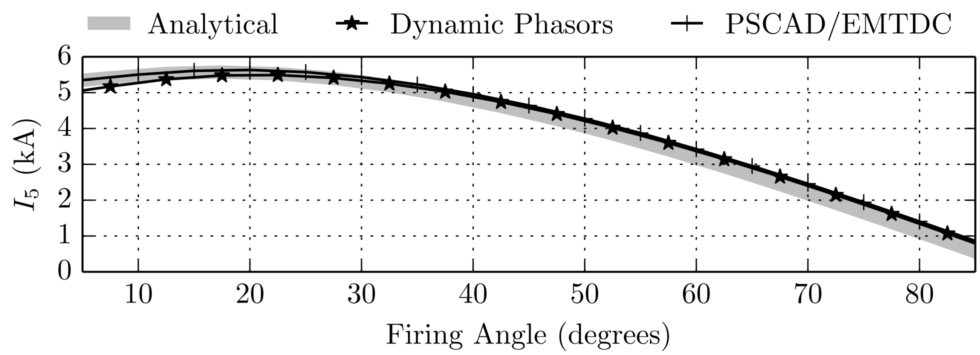

(b) Fifth harmonic

Figure 5.19: Comparison of the ac-side line current harmonics for various firing angles between 5° to 85°

Figures 5.20 and 5.21 illustrate the dynamic characteristics of the load voltage, v_o, and the ac-side line current, i_a, respectively. In this test, the firing angle was initially set to 5°, which was changed to 30° at 0.1 s followed by a second change to 70° at 0.175 s. The set of harmonics used to simulate this system is equal to $\{0, 1\}$ such that these simulations only capture the averaged behaviour of the system. The waveforms illustrate that the dynamic phasor simulation results and in good agreement with the PSCAD/EMTDC results and that the LCC model accurately captures the averaged behaviour of the test system. Figure 5.20 illustrates a minor discrepancy in the dc voltage waveforms at 0.175 s, where the firing angle is changed from 30° to 70°. This error may be attributed to the thyristor dead time problem discussed in Section 5.3.4.

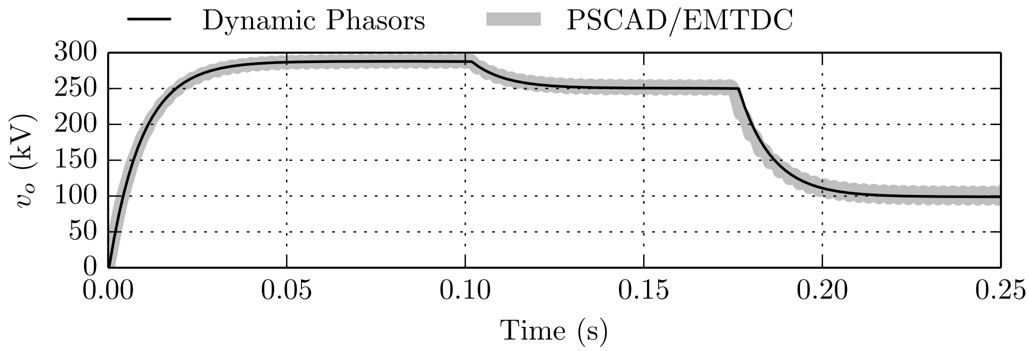

Figure 5.20: Comparison of the load voltage dynamics for various firing angles

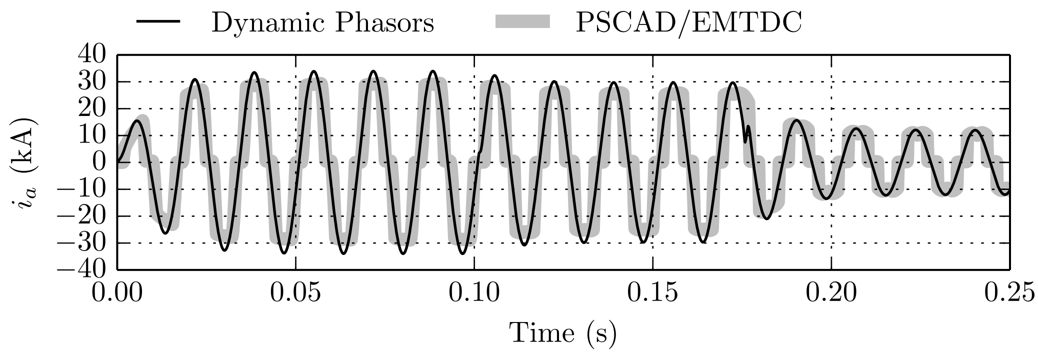

Figure 5.21: Comparison of the ac-side line current dynamics for various firing angles

Figures 5.22 and 5.23 illustrate several cycles of the load voltage and ac-side line current waveforms, respectively. The simulations were carried out using a firing angle of 5° and the set of harmonics given by $\{0, 1, 5, 6, 7, 11, 12, 13\}$ to capture the switching characteristics of the converter. The results show that there is some error near the discontinuities in the PSCAD/EMTDC waveforms, which is expected due to the truncated series used to generate the reconstructed dynamic phasor waveforms. However, the results show that the dynamic phasor simulation results appear to converge to the PSCAD/EMTDC waveforms, indicating good agreement between the two methods.

Figures 5.24 and 5.25 illustrate several cycles of the load voltage and ac-side line current, respectively. The simulations were carried out using a firing angle of 30° and the set of harmonics given by $\{0, 1, 5, 6, 7, 11, 12, 13\}$. The reconstructed ac-side line current waveform shown in Figure 5.25 appears to converge to the PSCAD/EMTDC waveform, indicating good agreement between the two methods.

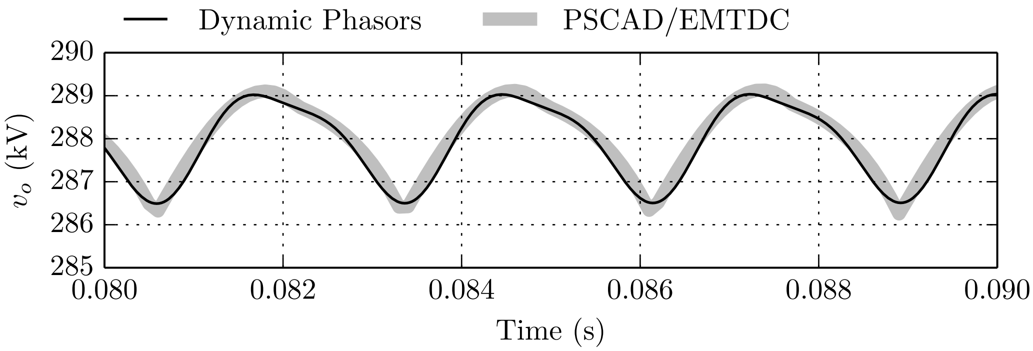

Figure 5.22: Comparison of the load voltage steady state waveforms with a firing angle of $5°$

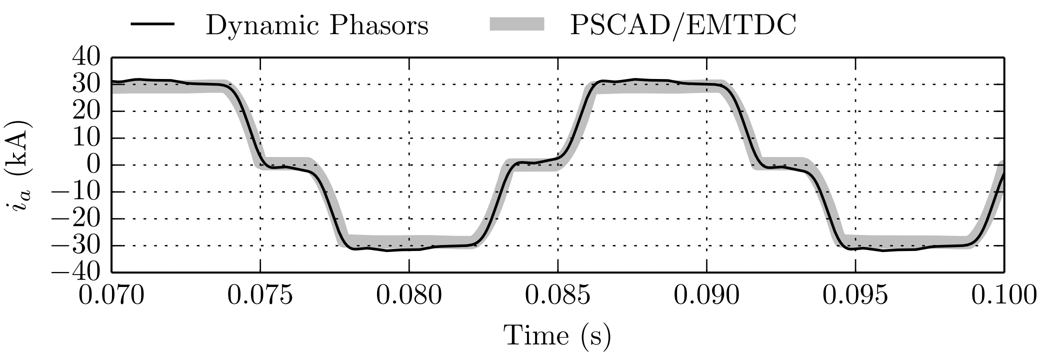

Figure 5.23: Comparison of the ac-side line current steady state waveforms with a firing angle of $5°$

Figure 5.24 illustrates that the reconstructed load voltage waveform is no longer in good agreement with the PSCAD/EMTDC results. The reconstructed waveform produced by the dynamic phasor simulations appears to have the correct shape, but its dc value is offset from the PSCAD/EMTDC waveform. Closer inspection of Figure 5.18a reveals that the disagreement between the average values produced by dynamic phasors and PSCAD/EMTDC increases as firing angle increases. This error may be attributed to the load model problem previously discussed.

Figures 5.27 and 5.28 illustrate the load voltage and ac-side line current following the balanced three phase balanced fault shown in Figure 5.26. The simulations were carried out using a firing angle of $5°$ and the set of harmonics given by $\{0, 1\}$. A fault resistance of $1\,\text{m}\Omega$ was applied at $0.1\,\text{s}$ for $0.05\,\text{s}$. The simulation results demonstrate that the LCC model performs well during the fault and is in good agreement with the PSCAD/EMTDC model. However, there is some error at the moment the fault is cleared, where the dynamic phasor model appears to respond faster than the PSCAD/EMTDC model. This error is due to the fact that the dynamic phasor model is able to respond immediately to the cleared fault and do not capture the discrete switching characteristics of the time-domain converter model.

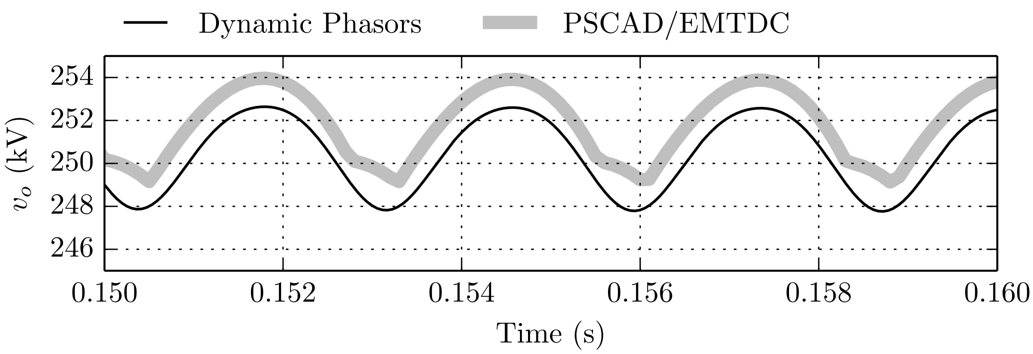

Figure 5.24: Comparison of the load voltage steady state waveforms with a firing angle of 30°

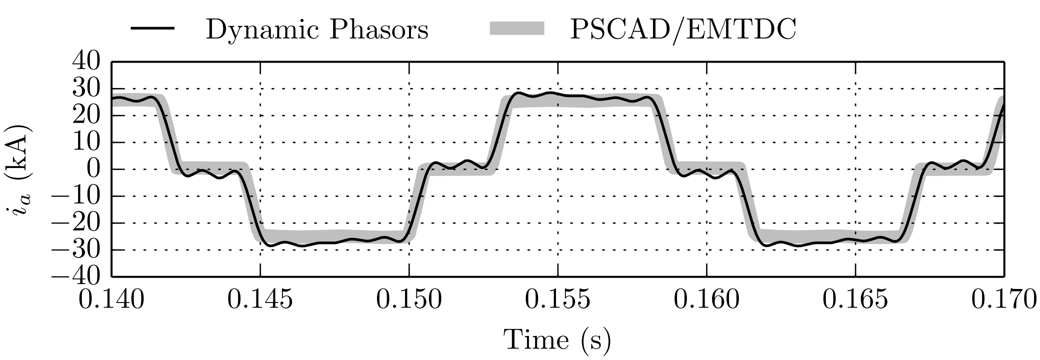

Figure 5.25: Comparison of the ac-side line current steady state waveforms with a firing angle of 30°

Figures 5.30 and 5.31 illustrate the load voltage and ac-side line current following the unbalanced line-to-line fault shown in Figure 5.29. The simulations were carried out using a firing angle of 5° and the set of harmonics given by $\{0, 1\}$. A fault resistance of $1\,\text{m}\Omega$ was applied at 0.1 s for 0.05 s. The simulation results demonstrate that the LCC model is not in good agreement with the PSCAD/EMTDC model. However, these results are expected since the dynamic phasor model was derived under the assumption that the ac system is balanced and the presence of an unbalanced fault on the ac side of the converter violates this assumption. Furthermore, the recovery period also illustrates that the dynamic phasor LCC model requires more time to recover from the fault. This additional recovery time is due to the fact that the dynamic phasor PLL model only uses the angles of v_a and v_c to generate an ac system angle for the LCC. This approach provides an accurate measure of the angle produced by the time-domain PLL during balanced conditions. However, in the presence of any unbalanced conditions, the time-domain and dynamic phasor PLL outputs will no longer be in agreement.

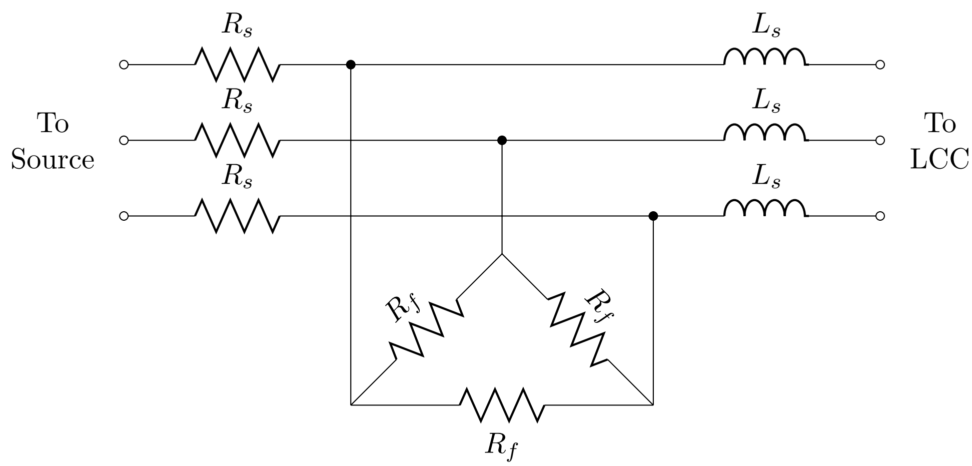

Figure 5.26: Three phase balanced fault

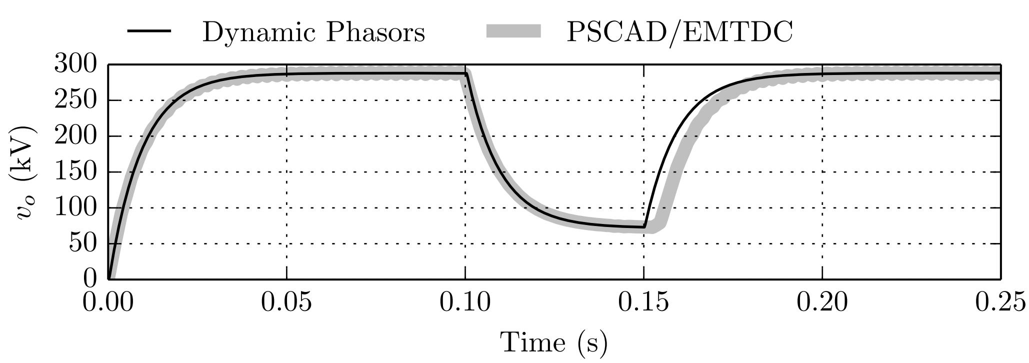

Figure 5.27: Comparison of the load voltage dynamics following a three phase balanced fault

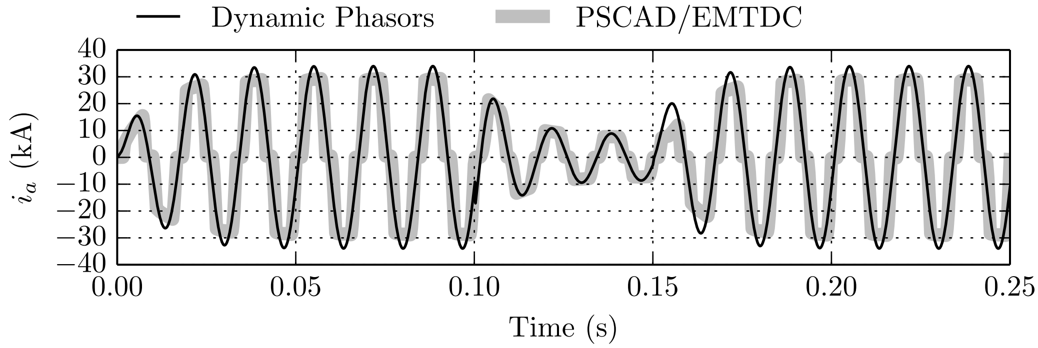

Figure 5.28: Comparison of the ac-side line current dynamics following a three phase balanced fault

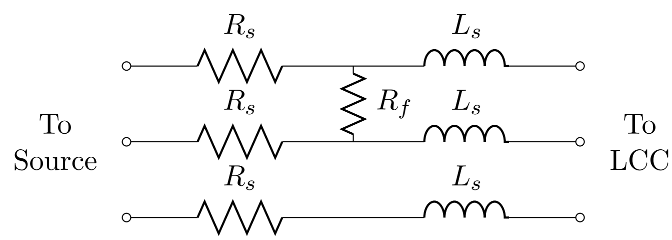

Figure 5.29: Unbalanced line-to-line fault

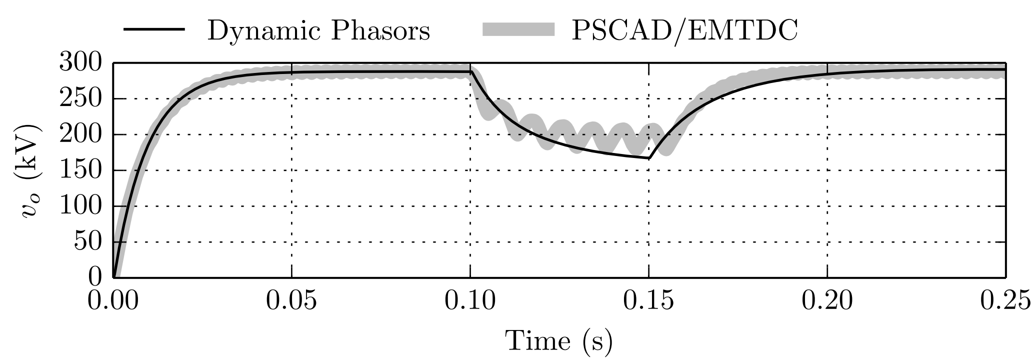

Figure 5.30: Comparison of the load voltage dynamics following an unbalanced line-to-line fault

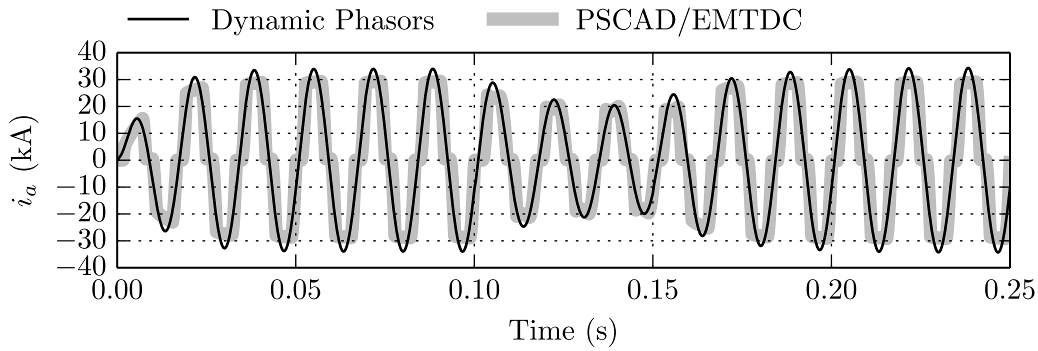

Figure 5.31: Comparison of the ac-side line current dynamics following an unbalanced line-to-line fault

5.6 Summary

This chapter presented an LCC model for use in the general purpose simulation method discussed in Chapter 3. This model was derived using the switching function method, which is commonly used in literature to model power electronic converters using dynamic phasors. The final LCC model includes the effects of source side inductance and the dynamics associated with thyristors. The continuous dynamic phasor model appears as a set of coupled sources for the ac and dc sides of the converter, which is consistent with other models presented in literature. The discrete form of the LCC model uses a time step delay to decouple the ac and dc equations, which allows the LCC model to be included in a set of nodal equations. Comparisons of simulation results produced using dynamic phasors and PSCAD/EMTDC were included in this chapter. The simulation results generally demonstrated good agreement between the two methods. However, the results also identified areas in which the models differ, such as unbalanced faults and significant harmonic content in the dc system. The disagreement between the dynamic phasor and PSCAD/EMTDC simulation results could be attributed to the fact that the test system did not satisfy the requirements of the dynamic phasor LCC model under all operating conditions.

Chapter 6

Synchronous Machines

Synchronous machines are among the most important elements in power systems and are found in a number of applications. A synchronous machine may operate as a synchronous generator, motor, or condenser [4, 43]. Synchronous generators are used to generate the majority of the world's electrical energy and are the primary source of both real and reactive power for loads in ac power systems [43]. Synchronous motors are used to drive large industrial loads, and synchronous condensers are used to provide reactive power support for transmission networks [4].

Synchronous machines differ from the other models considered previously in this work because they consist of both electrical and mechanical subsystems. The synchronous machine consists of a rotating shaft, also known as the rotor, which is generally equipped with the field winding [4]. An external dc source, known as the exciter, provides power to the field winding and establishes a rotating magnetic field within the machine. This field rotates within the stationary part of the machine, also known as the stator, which is generally equipped with the armature windings. The rotating magnetic field induces a voltage on the stator or armature windings, which in turn induces its own magnetic field within the machine [43]. Energy is then transferred between electrical and mechanical subsystems through the electromagnetic fields produced by the stator and rotor. A governor is used to control the amount of energy transferred within these subsystems by controlling the speed of the rotor in synchronous generators [4].

Proper representation of synchronous machines in power system models is required to ensure simulation results are reliable and accurate. The type of studies being performed dictates the synchronous machine model that must be included in simulations. For shorter duration studies that are concerned with high frequency transients, the synchronous machine may be modeled as a voltage source in series with an inductance [1]. However, models that include the mechanical subsystem are required for longer term studies that are concerned with low frequency electromechanical transients. For example, power system stability studies are concerned with the interactions between the electrical network and mechanical subsystems in synchronous machines [4].

Modeling and simulation of synchronous machines has been approached using a number of different methods in literature. The first method takes advantage of space vectors and sequence components to develop a dynamic phasor model of the synchronous machine [27,28]. An advantage of this method is that the effects of imbalance and harmonics in the ac system may be directly observed from the dynamic phasor form of the machine equations. Another approach used in literature to develop a dynamic phasor model of the synchronous machine is to directly convert the three phase model without a change of reference frame [2, 27]. Previous research has demonstrated that these synchronous machine models are capable of accurately modeling the machine dynamics, under both balanced and unbalanced ac system configurations. However, the simulations have focused on demonstrating these models in the context of larger system studies, where an infinite bus is used to model the ac system. In these situations, the frequency of stator quantities is constant and set by the infinite bus.

The method used in this work differs from previous research as it uses conventional reference frame transformation methods to obtain a dynamic phasor-based model of the synchronous machine, including its mechanical subsystem. Section 6.1 outlines the theory of synchronous machines and develops the differential equations describing its dynamic behaviour in terms of time-domain quantities. This model is then converted to a continuous dynamic phasor representation in Section 6.2. A discrete dynamic phasor representation of the synchronous machine is developed in Section 6.3 using the continuous dynamic phasor model. Finally, simulation results for two test systems are provided in Section 6.4.

6.1 Theory

Figure 6.1 illustrates the physical construction of a salient pole synchronous machine [43]. The axis of each phase corresponds to the magnetic axis of its respective winding. The direct (d) axis corresponds to the magnetic axis of the rotor while the quadrature (q) axis leads the d-axis by 90 degrees. The instantaneous rotor angle, θ_r, is defined as the angle of the rotor q-axis measured with respect to the a-phase magnetic axis as shown in Figure 6.1. In the following section, θ_r is assumed to be in electrical radians while the angular frequency of the rotor, ω_r, is assumed to be in per unit.

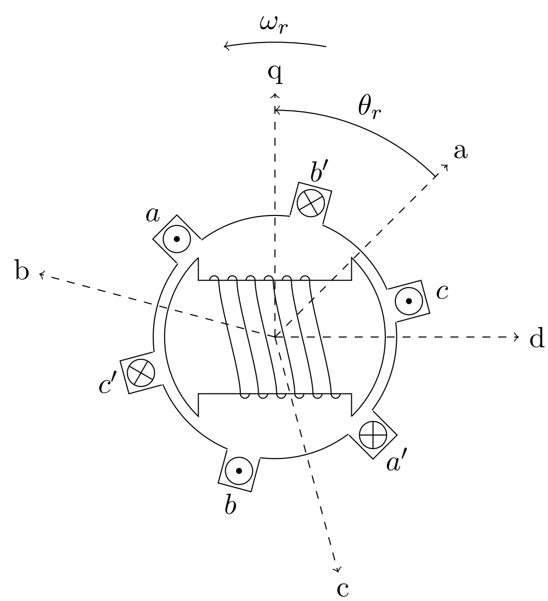

Figure 6.1: Physical construction of a synchronous machine

The electrical model of the stator windings is shown in Figure 6.2, where all quantities are in per unit [43]. A single inductance behind an armature resistance, R_s, is used to model each phase. The magnetic flux linkage, ψ, represents the combined effect of the rotor and other stator windings. The motor convention was used to model synchronous machines in this work and therefore, it was assumed that current entering the stator is positive.

The electrical model of the rotor is shown in Figure 6.3, where all values are in per unit on the stator bases [43]. The first circuit on the d-axis is used to model the effects of the field winding, which is denoted by the subscript fd. The rotor electrical model also includes a single damper circuit on the d-axis, denoted by the subscript $1d$, and two damper circuits on the q-axis, denoted by subscripts $1q$ and $2q$. Damper circuits are used in synchronous machine models to account for the effects of currents induced on the rotor.

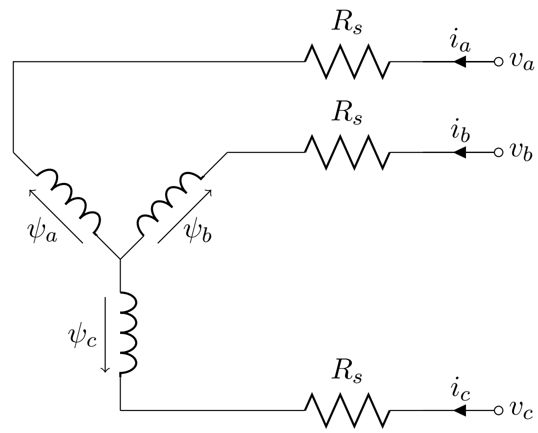

Figure 6.2: Electrical model of the stator

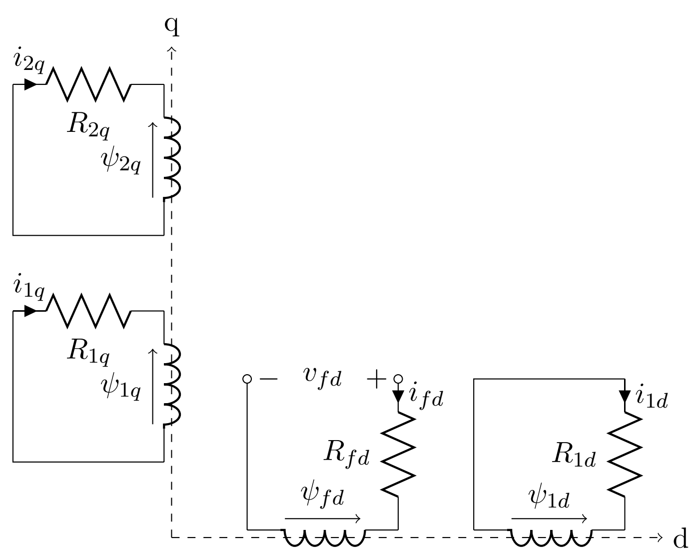

Figure 6.3: Electrical model of the rotor

The currents in the stator and rotor windings are related to the magnetic flux linkages through the machine inductances [43] as follows:

$$\begin{bmatrix} \boldsymbol{\psi}_s \\ \boldsymbol{\psi}_r \end{bmatrix} = \begin{bmatrix} \mathbf{L}_s(\theta_r) & \mathbf{L}_{sr}(\theta_r) \\ \mathbf{L}_{sr}^T(\theta_r) & \mathbf{L}_r \end{bmatrix} \begin{bmatrix} \mathbf{i}_s \\ \mathbf{i}_r \end{bmatrix}, \tag{6.1}$$

where the magnetic flux linkage and current vectors are given by

$$\boldsymbol{\psi}_s = \begin{bmatrix} \psi_a \\ \psi_b \\ \psi_c \end{bmatrix}; \quad \boldsymbol{\psi}_r = \begin{bmatrix} \psi_{1q} \\ \psi_{2q} \\ \psi_{fd} \\ \psi_{1d} \end{bmatrix}; \quad \mathbf{i}_s = \begin{bmatrix} i_a \\ i_b \\ i_c \end{bmatrix}; \text{ and } \quad \mathbf{i}_r = \begin{bmatrix} i_{1q} \\ i_{2q} \\ i_{fd} \\ i_{1d} \end{bmatrix}.$$

The matrix $\mathbf{L}_s(\theta_r)$ in (6.1) is used to represent the stator self and leakage inductances as well as the mutual inductance between different phases [43]. As shown in Figure 6.1, the rotor is not symmetrical with respect to the d and q-axes. As a result, the stator self and mutual inductances vary as the rotor position changes. The elements in $\mathbf{L}_s(\theta_r)$ are given by

$$\mathbf{L}_s(\theta_r) = \begin{bmatrix} L_{ls} + L_{ss}(\theta_r) & -L_{sm}(\theta_r - \pi/3) & -L_{sm}(\theta_r + \pi/3) \\ -L_{sm}(\theta_r - \pi/3) & L_{ls} + L_{ss}(\theta_r - 2\pi/3) & -L_{sm}(\theta_r - \pi) \\ -L_{sm}(\theta_r + \pi/3) & -L_{sm}(\theta_r - \pi) & L_{ls} + L_{ss}(\theta_r + 2\pi/3) \end{bmatrix}, \tag{6.2}$$

where L_{ls} is the leakage inductance of the stator windings. $L_{ss}(\theta)$ and $L_{sm}(\theta)$ are the stator self and mutual inductances, respectively, which are given by

$$L_{ss}(\theta) = L_A - L_B \cos(2\theta); \text{ and} \tag{6.3}$$

$$L_{sm}(\theta) = \frac{1}{2}L_A + L_B \cos(2\theta), \tag{6.4}$$

where L_A and L_B depend on the physical parameters of the machine [43].

The matrix $\mathbf{L}_{sr}(\theta_r)$ in (6.1) is used to represent the mutual inductances between the stator and rotor circuits [43]. The elements in this matrix are given by

$$\mathbf{L}_{sr}(\theta_r) = \begin{bmatrix} L_{mq}\cos(\theta_r) & L_{mq}\cos(\theta_r) & L_{md}\sin(\theta_r) & L_{md}\sin(\theta_r) \\ L_{mq}\cos\left(\theta_r - \frac{2\pi}{3}\right) & L_{mq}\cos\left(\theta_r - \frac{2\pi}{3}\right) & L_{md}\sin\left(\theta_r - \frac{2\pi}{3}\right) & L_{md}\sin\left(\theta_r - \frac{2\pi}{3}\right) \\ L_{mq}\cos\left(\theta_r + \frac{2\pi}{3}\right) & L_{mq}\cos\left(\theta_r + \frac{2\pi}{3}\right) & L_{md}\sin\left(\theta_r + \frac{2\pi}{3}\right) & L_{md}\sin\left(\theta_r + \frac{2\pi}{3}\right) \end{bmatrix}, \tag{6.5}$$

where L_{md} and L_{mq} are the magnetizing inductances of the d and q-axes respectively.

Finally, the matrix $\mathbf{L}_r$ in (6.1) is used to represent the leakage and self inductances of the rotor circuits and any mutual inductance between rotor circuits on the same axis [43]. The elements of $\mathbf{L}_r$ are given by

$$\mathbf{L}_r = \begin{bmatrix} L_{l1q} + L_{mq} & L_{mq} & 0 & 0 \\ L_{mq} & L_{l2q} + L_{mq} & 0 & 0 \\ 0 & 0 & L_{lfd} + L_{md} & L_{md} \\ 0 & 0 & L_{md} & L_{l1d} + L_{md} \end{bmatrix}, \tag{6.6}$$

where L_{l1q}, L_{l2q}, L_{lfd}, and L_{l1d} are the rotor circuit leakage inductances. The relationship between the stator terminal voltages, magnetic flux linkages, and currents is given by

$$\frac{d}{dt}\begin{bmatrix} \psi_a \\ \psi_b \\ \psi_c \end{bmatrix} = \begin{bmatrix} v_a \\ v_b \\ v_c \end{bmatrix} - R_s \begin{bmatrix} i_a \\ i_b \\ i_c \end{bmatrix} \tag{6.7a}$$

$$\frac{d\boldsymbol{\psi}_s}{dt} = \mathbf{v}_s - R_s\mathbf{i}_s. \tag{6.7b}$$

Similarly, the relationship between the rotor field voltage, magnetic flux linkages, and currents is given by

$$\frac{d}{dt}\begin{bmatrix} \psi_{1q} \\ \psi_{2q} \\ \psi_{fd} \\ \psi_{1d} \end{bmatrix} = \begin{bmatrix} 0 \\ 0 \\ v_{fd} \\ 0 \end{bmatrix} - \begin{bmatrix} R_{1q} & 0 & 0 & 0 \\ 0 & R_{2q} & 0 & 0 \\ 0 & 0 & R_{fd} & 0 \\ 0 & 0 & 0 & R_{1d} \end{bmatrix} \begin{bmatrix} i_{1q} \\ i_{2q} \\ i_{fd} \\ i_{1d} \end{bmatrix} \tag{6.8a}$$

$$\frac{d\boldsymbol{\psi}_r}{dt} = \mathbf{v}_r - \mathbf{R}_r\mathbf{i}_r. \tag{6.8b}$$

The dependence of the inductances in (6.1) on θ_r is undesirable since the rotor position changes with time. Hence, the inductances are functions of time, which complicates analysis and has efficiency implications in simulations involving synchronous machines [1]. The method used to eliminate θ_r from (6.1) is to refer all of stator quantities from their stationary reference frame to the rotor's reference frame [54]. Park's transformation may be used to refer stator quantities to the rotor and is given by

$$\begin{bmatrix} x_q \\ x_d \\ x_0 \end{bmatrix} = \frac{2}{3} \begin{bmatrix} \cos(\theta_r) & \cos\left(\theta_r - \frac{2\pi}{3}\right) & \cos\left(\theta_r + \frac{2\pi}{3}\right) \\ \sin(\theta_r) & \sin\left(\theta_r - \frac{2\pi}{3}\right) & \sin\left(\theta_r + \frac{2\pi}{3}\right) \\ \frac{1}{2} & \frac{1}{2} & \frac{1}{2} \end{bmatrix} \begin{bmatrix} x_a \\ x_b \\ x_c \end{bmatrix} \tag{6.9a}$$

$$\mathbf{x}' = \mathbf{T}_p \mathbf{x}. \tag{6.9b}$$

The stator quantities must be referred back to the stator's reference frame to interface a synchronous machine with a larger system model. The inverse of Park's transformation may be used to refer the stator quantities back to the stator reference frame [54] and is given by

$$\begin{bmatrix} x_a \\ x_b \\ x_c \end{bmatrix} = \begin{bmatrix} \cos(\theta_r) & \sin(\theta_r) & 1 \\ \cos\left(\theta_r - \frac{2\pi}{3}\right) & \sin\left(\theta_r - \frac{2\pi}{3}\right) & 1 \\ \cos\left(\theta_r + \frac{2\pi}{3}\right) & \sin\left(\theta_r + \frac{2\pi}{3}\right) & 1 \end{bmatrix} \begin{bmatrix} x_q \\ x_d \\ x_0 \end{bmatrix} \tag{6.10a}$$

$$\mathbf{x} = \mathbf{T}_p^{-1} \mathbf{x}'. \tag{6.10b}$$

Applying Park's transformation to (6.1) yields the synchronous machine magnetic flux linkage equations with the stator quantities referred to the rotor reference frame [43]. The adjusted magnetic flux equations are given by

$$\begin{bmatrix} \boldsymbol{\psi}'_s \\ \boldsymbol{\psi}_r \end{bmatrix} = \begin{bmatrix} \mathbf{L}'_s & \mathbf{L}'_{sr} \\ (\mathbf{L}'_{sr})^T & \mathbf{L}_r \end{bmatrix} \begin{bmatrix} \mathbf{i}'_s \\ \mathbf{i}_r \end{bmatrix}. \tag{6.11}$$

The matrix $\mathbf{L}'_s$ in (6.11) is used to represent the stator self and leakage inductances where the stator quantities have been referred to the rotor's frame of reference. The elements of this matrix are given by

$$\mathbf{L}'_s = \begin{bmatrix} L_{ls} + L_{mq} & 0 & 0 \\ 0 & L_{ls} + L_{md} & 0 \\ 0 & 0 & L_{ls} \end{bmatrix}. \tag{6.12}$$

Similarly, the matrix $\mathbf{L}'_{sr}$ in (6.11) is used to represent the mutual inductances between the stator and the rotor where the stator quantities have been referred to the rotor's frame of reference. The elements of this matrix are given by

$$\mathbf{L}'_{sr} = \begin{bmatrix} L_{mq} & L_{mq} & 0 & 0 \\ 0 & 0 & L_{md} & L_{md} \\ 0 & 0 & 0 & 0 \end{bmatrix}. \tag{6.13}$$

The elements of the inductance matrices in (6.11) demonstrate that the q-axis, d-axis, and zero sequence flux linkages and currents are completely decoupled. As a result, (6.11) may be written as three independent sets of equations, which are given by

$$\begin{bmatrix} \psi_q \\ \psi_{1q} \\ \psi_{2q} \end{bmatrix} = \begin{bmatrix} L_{ls} + L_{mq} & L_{mq} & L_{mq} \\ L_{mq} & L_{l1q} + L_{mq} & L_{mq} \\ L_{mq} & L_{mq} & L_{l2q} + L_{mq} \end{bmatrix} \begin{bmatrix} i_q \\ i_{1q} \\ i_{2q} \end{bmatrix} \tag{6.14a}$$

$$\boldsymbol{\psi}_q = \mathbf{L}_q \mathbf{i}_q; \tag{6.14b}$$

$$\begin{bmatrix} \psi_d \\ \psi_{fd} \\ \psi_{1d} \end{bmatrix} = \begin{bmatrix} L_{ls} + L_{md} & L_{md} & L_{md} \\ L_{md} & L_{lfd} + L_{md} & L_{md} \\ L_{md} & L_{md} & L_{l1d} + L_{md} \end{bmatrix} \begin{bmatrix} i_d \\ i_{fd} \\ i_{1d} \end{bmatrix} \tag{6.15a}$$

$$\boldsymbol{\psi}_d = \mathbf{L}_d \mathbf{i}_d; \text{ and} \tag{6.15b}$$

$$\psi_0 = L_{ls} i_0. \tag{6.16}$$

Applying Park's transformation to (6.7b) yields the stator terminal voltage equations for the synchronous machine with the stator quantities referred to the rotor's frame of reference. The adjusted stator voltage equations are given by

$$\frac{d}{dt}\begin{bmatrix} \psi_q \\ \psi_d \\ \psi_0 \end{bmatrix} = \begin{bmatrix} v_q \\ v_d \\ v_0 \end{bmatrix} + \begin{bmatrix} 0 & -\omega_r & 0 \\ \omega_r & 0 & 0 \\ 0 & 0 & 0 \end{bmatrix} \begin{bmatrix} \psi_q \\ \psi_d \\ \psi_0 \end{bmatrix} - R_s \begin{bmatrix} i_q \\ i_d \\ i_0 \end{bmatrix} \tag{6.17a}$$

$$\frac{d\boldsymbol{\psi}'_s}{dt} = \mathbf{v}'_s + \mathbf{v}_{sv} - R_s\mathbf{i}'_s, \tag{6.17b}$$

where the elements of $\mathbf{v}_{sv}$ are known as the speed voltages [4]. The equations in (6.17a) show that the q and d-axis stator terminal voltage equations are not completely decoupled due to the speed voltages.

The magnetic flux linkage equations given by (6.14b), (6.15b), and (6.16) together with the terminal voltage equations given by (6.8b) and (6.17b) describe the electrical dynamics of the synchronous machine. Additional differential equations are required to model the mechanical dynamics of synchronous machines [4]. The first equation relates the instantaneous rotor angle to the angular frequency of the rotor [43], which is given by

$$\frac{d\theta_r}{dt} = \omega_b\omega_r, \tag{6.18}$$

where ω_b is the base angular frequency of the machine. The second equation gives the relationship between the angular frequency of the rotor and the net torque applied to the shaft of the machine [43], which is given by

$$\frac{d\omega_r}{dt} = \frac{T_e - T_L + D\omega_r}{2H}, \tag{6.19}$$

where H is the inertia constant of the synchronous machine and T_L is the per unit load torque applied to the machine. The $D\omega_r$ term in (6.19) is used to represent any mechanical damping effects, where D is the machine damping factor [4]. T_e is the per unit electromagnetic air gap torque of the machine [43], which is given by

$$T_e = \psi_d i_q - \psi_q i_d. \tag{6.20}$$

6.2 Continuous Dynamic Phasor Model

The synchronous machine equations derived in the previous section may be readily converted to dynamic phasors using the dynamic phasor operator and properties discussed in Section 1.2. Applying the dynamic phasor operator to (6.14b), (6.15b), and (6.16) yields the dynamic phasor form of the magnetic flux linkage equations, which are given by

$$\left\langle \boldsymbol{\psi}_q \right\rangle_k = \mathbf{L}_q \left\langle \mathbf{i}_q \right\rangle_k ; \tag{6.21}$$

$$\left\langle \boldsymbol{\psi}_d \right\rangle_k = \mathbf{L}_d \left\langle \mathbf{i}_d \right\rangle_k ; \text{ and} \tag{6.22}$$

$$\left\langle \psi_0 \right\rangle_k = L_{ls} \left\langle i_0 \right\rangle_k . \tag{6.23}$$

Similarly, applying the dynamic phasor operator to (6.8b) and (6.17b) yields the dynamic phasor form of the terminal voltage equations, which are given by

$$\frac{d \left\langle \boldsymbol{\psi}_r \right\rangle_k}{dt} = \left\langle \mathbf{v}_r \right\rangle_k - jk\omega_0 \left\langle \boldsymbol{\psi}_r \right\rangle_k - \mathbf{R}_r \left\langle \mathbf{i}_r \right\rangle_k ; \text{ and} \tag{6.24}$$

$$\frac{d \left\langle \boldsymbol{\psi}'_s \right\rangle_k}{dt} = \left\langle \mathbf{v}'_s \right\rangle_k + \left\langle \mathbf{v}_{sv} \right\rangle_k - jk\omega_0 \left\langle \boldsymbol{\psi}'_s \right\rangle_k - R_s \left\langle \mathbf{i}'_s \right\rangle_k , \tag{6.25}$$

where the dynamic phasors of the speed voltages are given by

$$\left\langle \mathbf{v}_{sv} \right\rangle_k = \begin{bmatrix} -\sum\limits_{l=-\infty}^{\infty} \left\langle \omega_r \right\rangle_{k-l} \left\langle \psi_d \right\rangle_l \\ \sum\limits_{l=-\infty}^{\infty} \left\langle \omega_r \right\rangle_{k-l} \left\langle \psi_q \right\rangle_l \\ 0 \end{bmatrix} . \tag{6.26}$$

Finally, applying the dynamic phasor operator to (6.18) to (6.20) yields the dynamic phasor form of the mechanical equations, which are given by

$$\frac{d \left\langle \theta_r \right\rangle_k}{dt} = -jk\omega_0 \left\langle \theta_r \right\rangle_k + \omega_b \left\langle \omega_r \right\rangle_k ; \tag{6.27}$$

$$\frac{d \left\langle \omega_r \right\rangle_k}{dt} = \left(\frac{D}{2H} - jk\omega_0 \right) \left\langle \omega_r \right\rangle_k + \frac{\left\langle T_e \right\rangle_k - \left\langle T_L \right\rangle_k}{2H} ; \text{ and} \tag{6.28}$$

$$\left\langle T_e \right\rangle_k = \sum_{l=-\infty}^{\infty} \left(\left\langle \psi_d \right\rangle_{k-l} \left\langle i_q \right\rangle_l - \left\langle \psi_q \right\rangle_{k-l} \left\langle i_d \right\rangle_l \right) . \tag{6.29}$$

The equations given by (6.21) to (6.29) form a complete dynamic phasor model of the synchronous machine in the rotor's frame of reference. This model may be used to simulate a machine connected to an infinite bus or a small subsystem that is also modeled using $qd0$ coordinates [2]. However, this approach cannot be used to model synchronous machines in this work since the components derived in Chapter 3 were not derived for three phase systems and $qd0$ coordinates. Therefore, the dynamic phasor synchronous machine quantities must be interfaced with the network using Park's transformation. The dynamic phasor form of Park's transformation may be obtained by applying the dynamic phasor operator to (6.9b), which yields:

$$\left\langle \mathbf{x}' \right\rangle_k = \sum_{l=-\infty}^{\infty} \left\langle \mathbf{T}_p \right\rangle_{k-l} \left\langle \mathbf{x} \right\rangle_l . \tag{6.30}$$

The equation given by (6.30) demonstrates that the dynamic phasors of the transformation matrix, $\left\langle \mathbf{T}_p \right\rangle_k$, are required to carry out the transformation. However, expressions for $\left\langle \mathbf{T}_p \right\rangle_k$ cannot be obtained using a straightforward application of the dynamic phasor operator since the elements of $\mathbf{T}_p$ are nonlinear functions of θ_r. Instead, the approach demonstrated in Section 3.3 that was used to obtain dynamic phasors for variable frequency sources may also be used to obtain expressions for $\left\langle \mathbf{T}_p \right\rangle_k$. A similar approach has been used to develop a synchronous machine model without Park's transformation, which involves finding the dynamic phasors of the variable inductance matrices, i.e. $\mathbf{L}_s\left(\theta_r\right)$ [27]. Park's transformation may be written as a Fourier series using θ_r as the independent variable as follows:

$$\mathbf{T}_p = \sum_{k=-\infty}^{\infty} \mathbf{C}_k e^{jk\theta_r}. \tag{6.31}$$

The Fourier coefficients, $\mathbf{C}_k$, in (6.31) are given by

$$\mathbf{C}_k = \frac{1}{3} \begin{cases} \begin{bmatrix} 0 & 0 & 0 \\ 0 & 0 & 0 \\ 1 & 1 & 1 \end{bmatrix} & k = 0 \\ \begin{bmatrix} 1 & \alpha & \alpha^* \\ -j & -j\alpha & -j\alpha^* \\ 0 & 0 & 0 \end{bmatrix} & k = 1 \\ \mathbf{0}_{3\times 3} & \text{otherwise,} \end{cases} \tag{6.32}$$

where $\alpha = e^{-j2\pi/3}$. The Fourier series given by (6.32) may be converted to dynamic phasors by simply adding and subtracting the product of the dynamic phasor base frequency and time, $\omega_0 t$, from each exponential basis function. The dynamic phasor-based series of Park's transformation is given by

$$\mathbf{T}_p = \sum_{k=-\infty}^{\infty} \langle \mathbf{T}_p \rangle_k (t)\, e^{jk\omega_0 t}, \tag{6.33}$$

where the dynamic phasors of the transformation matrix are given by

$$\langle \mathbf{T}_p \rangle_k (t) = \frac{e^{jk(\theta_r - \omega_0 t)}}{3} \begin{cases} \begin{bmatrix} 0 & 0 & 0 \\ 0 & 0 & 0 \\ 1 & 1 & 1 \end{bmatrix} & k = 0 \\ \begin{bmatrix} 1 & \alpha & \alpha^* \\ -j & -j\alpha & -j\alpha^* \\ 0 & 0 & 0 \end{bmatrix} & k = 1 \\ \mathbf{0}_{3\times 3} & \text{otherwise.} \end{cases} \tag{6.34}$$

The dynamic phasors of the inverse of Park's transformation, $\langle \mathbf{T}_p^{-1} \rangle_k$, may be derived using the same method and are given by

$$\langle \mathbf{T}_p^{-1} \rangle_k (t) = \frac{e^{jk(\theta_r - \omega_0 t)}}{2} \begin{cases} \begin{bmatrix} 0 & 0 & 2 \\ 0 & 0 & 2 \\ 0 & 0 & 2 \end{bmatrix} & k = 0 \\ \begin{bmatrix} 1 & -j & 0 \\ \alpha & -j\alpha & 0 \\ \alpha^* & -j\alpha^* & 0 \end{bmatrix} & k = 1 \\ \mathbf{0}_{3\times 3} & \text{otherwise.} \end{cases} \tag{6.35}$$

The dynamic phasors for the transformation matrices given by (6.34) and (6.35) are nonlinearly dependent on the instantaneous rotor angle, θ_r. This nonlinear relationship poses a problem since θ_r is an instantaneous time-domain quantity, which is not available in dynamic phasor-based simulations. The approximation used in this work to solve this problem is to assume that θ_r is well represented by its dc component, $\langle \theta_r \rangle_0$.

6.3 Discrete Dynamic Phasor Model

The stator of the synchronous machine is modeled in PSCAD/EMTDC as a set of three current sources, one for each terminal of the machine [1]. The current injection for each source is calculated in each time step using the network voltages from the previous time step and a discretized form of the equations listed in Section 6.1. The current sources are then used in the next time step by the nodal analysis simulation method to update the network voltages. This approach along with the continuous dynamic phasor equations listed in Section 6.2 will be used to obtain a discrete dynamic phasor equivalent of the synchronous machine.

The first step in the synchronous machine update procedure is to use the network voltages from the previous time step as inputs to the model. The network voltages are then referred to the rotor reference frame using Park's transformation as follows

$$\left\langle \mathbf{v}_s' \right\rangle_k [n-1] = \sum_{l=-\infty}^{\infty} \left\langle \mathbf{T}_p \right\rangle_{k-l} [n-1] \left\langle \mathbf{v}_s \right\rangle_l [n-1] \,, \tag{6.36}$$

where the dynamic phasors for Park's transformation in a discrete context are given by

$$\left\langle \mathbf{T}_p \right\rangle_k [n] = \frac{e^{jk\left(\langle \theta_r \rangle_0 [n] - \omega_0 t\right)}}{3} \begin{cases} \begin{bmatrix} 0 & 0 & 0 \\ 0 & 0 & 0 \\ 1 & 1 & 1 \end{bmatrix} & k = 0 \\ \begin{bmatrix} 1 & \alpha & \alpha^* \\ -j & -j\alpha & -j\alpha^* \\ 0 & 0 & 0 \end{bmatrix} & k = 1 \\ \mathbf{0}_{3\times 3} & \text{otherwise.} \end{cases} \tag{6.37}$$

The stator voltages from the previous time step calculated using (6.37) may be used to update the magnetic flux linkages. A difference equation is required since the stator voltage is related to the flux linkages through a differential relationship as shown in (6.25). However, the numerical methods discussed in Chapter 2 cannot be used in this situation since the magnetic flux linkage equations are nonlinear. An explicit method, such as Euler's forward method [34], must be used instead to convert the flux linkage differential equations to difference equations. Applying Euler's method to (6.25) yields the stator flux difference equations, which are given by

$$\left\langle \boldsymbol{\psi}'_s \right\rangle_k [n] = (1 - jk\omega_0 \Delta t) \left\langle \boldsymbol{\psi}'_s \right\rangle_k [n-1] + \Delta t \big(\left\langle \mathbf{v}'_s \right\rangle_k [n-1] + \left\langle \mathbf{v}_{sv} \right\rangle_k [n-1] \\ - R_s \left\langle \mathbf{i}'_s \right\rangle_k [n-1] \big) . \quad (6.38)$$

Similarly, a difference equation for the rotor magnetic flux linkages may be obtained by applying Euler's method to (6.24) as follows:

$$\left\langle \boldsymbol{\psi}_r \right\rangle_k [n] = (1 - jk\omega_0 \Delta t) \left\langle \boldsymbol{\psi}_r \right\rangle_k [n-1] + \Delta t \left(\left\langle \mathbf{v}_r \right\rangle_k [n-1] - \mathbf{R}_r \left\langle \mathbf{i}_r \right\rangle_k [n-1] \right) , \quad (6.39)$$

where the field voltage from the previous time step is used in $\left\langle \mathbf{v}_r \right\rangle_k [n-1]$. The approach used in PSCAD/EMTDC to obtain the field voltage is through an input to the machine, which may be connected to an external field subsystem model [1]. This approach was also used in the dynamic phasor synchronous machine equivalent to model the field subsystem.

The updated currents in the rotor's reference frame may be calculated using (6.21), (6.22), and (6.23) along with the updated values of the magnetic flux linkages from (6.38) and (6.39). Solving for the current vectors in (6.21), (6.22), and (6.23) and replacing continuous quantities with discrete quantities yields:

$$\left\langle \mathbf{i}_q \right\rangle_k [n] = \mathbf{L}_q^{-1} \left\langle \boldsymbol{\psi}_q \right\rangle_k [n] ; \quad (6.40)$$

$$\left\langle \mathbf{i}_d \right\rangle_k [n] = \mathbf{L}_d^{-1} \left\langle \boldsymbol{\psi}_d \right\rangle_k [n] ; \text{ and} \quad (6.41)$$

$$\left\langle i_0 \right\rangle_k [n] = \frac{1}{L_{ls}} \left\langle \psi_0 \right\rangle_k [n] . \quad (6.42)$$

Finally, the stator currents may be referred back to the stator reference frame using the inverse of Park's transformation and the values calculated in (6.40) to (6.42) as follows:

$$\left\langle \mathbf{i}_s \right\rangle_k [n] = \sum_{l=-\infty}^{\infty} \left\langle \mathbf{T}_p^{-1} \right\rangle_{k-l} [n] \left\langle \mathbf{i}'_s \right\rangle_l [n] , \quad (6.43)$$

where the dynamic phasors for the inverse of Park's transformation in a discrete context are given by

$$\left\langle \mathbf{T}_p^{-1} \right\rangle_k [n] = \frac{e^{jk\left(\langle \theta_r \rangle_0 [n] - \omega_0 t\right)}}{2} \begin{cases} \begin{bmatrix} 0 & 0 & 2 \\ 0 & 0 & 2 \\ 0 & 0 & 2 \end{bmatrix} & k = 0 \\ \begin{bmatrix} 1 & -j & 0 \\ \alpha & -j\alpha & 0 \\ \alpha^* & -j\alpha^* & 0 \end{bmatrix} & k = 1 \\ \mathbf{0}_{3\times 3} & \text{otherwise.} \end{cases} \tag{6.44}$$

The stator currents calculated in (6.43) are used as the values for the stator current sources. However, interfacing a model with the network using current sources and values based solely on the previous time step may result in numerical instability [1]. Therefore, the interfacing circuit shown in Section 5.2.3 must be included in the electrical model of the stator. Figure 6.4 illustrates the discrete dynamic equivalent of the stator including the numerical interfacing circuit. The current sources in Figure 6.4 account for both the stator current values given by (6.43) as well as the compensating conductance from the interfacing circuit. The a-phase current source is given by

$$I_{ak} [n] = \langle i_a \rangle_k [n] - G_a \langle v_a \rangle_k [n-1] \, , \tag{6.45}$$

where $\langle i_a \rangle_k [n]$ is the a-phase value calculated using (6.43). The interfacing conductance, G_a, in this case may be selected as a small value relative to the base impedance of the synchronous machine.

The equations describing the mechanical dynamics of the system must also be converted to a discrete representation to complete the discrete dynamic phasor equivalent of the synchronous machine. Applying Euler's method to (6.27) and (6.28) yields the discrete form of the mechanical equations given by

$$\langle \theta_r \rangle_k [n] = (1 - jk\omega_0 \Delta t) \langle \theta_r \rangle_k [n-1] + \Delta t \omega_b \langle \omega_r \rangle_k [n-1] \, ; \text{ and} \tag{6.46}$$

$$\langle \omega_r \rangle_k [n] = \left(1 + \Delta t \left(\frac{D}{2H} - jk\omega_0\right)\right) \langle \omega_r \rangle_k [n-1] + \frac{\Delta t}{2H} \left(\langle T_e \rangle_k [n-1] - \langle T_L \rangle_k [n-1]\right). \tag{6.47}$$

The load torque, T_L, is modeled in PSCAD/EMTDC as an input to the synchronous machine, which may be connected to an external governor and turbine subsystem model [1]. This approach was also used in the dynamic phasor synchronous machine equivalent to model the governor and turbine subsystem.

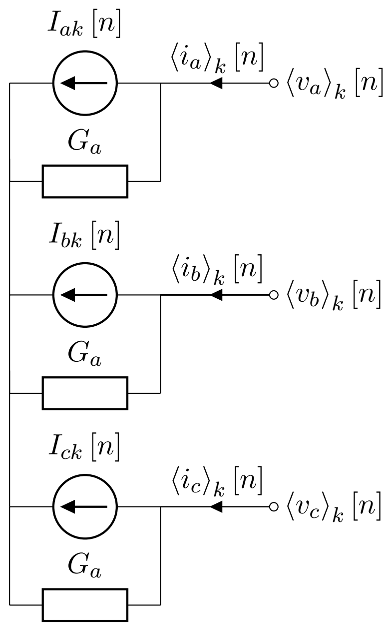

Figure 6.4: Discrete dynamic phasor equivalent of the synchronous machine stator circuit

6.4 Simulation Results

Two systems were used to demonstrate the dynamic phasor synchronous machine model developed in the previous section. The first system is a simple independent generator with a passive load. The synchronous machine in this case selects the electrical frequency for the entire network based on the frequency of the rotor. This system was selected to demonstrate that the synchronous machine model developed in this work is capable of simulating systems with machines where the electrical frequency is not necessarily equal to the base frequency of the dynamic phasor series.

The second system includes a synchronous generator with an infinite bus and a small electrical network, which has been used extensively in literature to demonstrate synchronous machine models [4]. The infinite bus in this configuration is used to represent a large electrical network with an essentially fixed voltage and frequency. This test system was selected to demonstrate that the synchronous machine model can also be used as part of a power system model for system wide studies.

Simulations of both systems were carried out using only the fundamental component for the ac system. The dynamic phasor form of Park's transformation given by (6.30) may be used to obtain a complete set of rotor harmonics with a given set of ac system harmonics. This equation reveals that a complete rotor reference frame model must include the set of harmonics given by $\{0, 1, 2\}$ for an ac system containing only the fundamental component. This observation is supported by previous research, which has shown that the dc component represents the contributions from positive sequence components in the ac system [2]. The first and second harmonics in the rotor reference frame represent the contributions from zero and negative sequence components in the ac system, respectively. Therefore, only the dc component in the rotor reference frame is required for balanced systems, while the higher order harmonics are required to represent imbalance in the ac system.

It should be noted, however, that the simulations in this work were carried out using only the dc component for the rotor reference frame equations. It was not possible to obtain numerically stable simulation results when the first and second harmonics were included in the set of rotor harmonics. The exact cause of the instability is unknown; however, it is likely due to the time step delay and the choice of Euler's method for numerical integration of the rotor differential equations.

6.4.1 Independent Generator

Figure 6.5 illustrates the single line diagram for the first example system that will be used to demonstrate the dynamic phasor synchronous machine model. The load model shown in Figure 6.5 includes two parallel loads, one which models a purely resistive load and the other which models a primarily inductive load. The synchronous machine includes a simple PI feedback controller for the exciter and governor systems. The exciter system is shown in Figure 6.6, which measures the RMS value of the stator terminal voltage using the three phase RMS meter discussed in Section 4.3 and regulates its value using the given reference. The governor system is shown in Figure 6.7, which uses rotor frequency measurements from the machine to regulate the frequency of the machine. Tables 6.1 and 6.2 contains all of the synchronous machine and system parameters used in the simulations respectively. The simulations were carried out using dynamic phasors and PSCAD/EMTDC assuming that all initial conditions, including the rotor frequency, are zero.

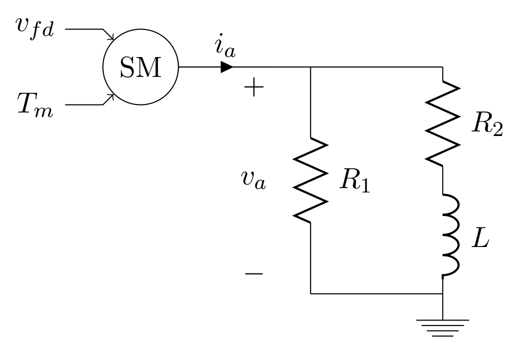

Figure 6.5: Independent synchronous machine with a passive load

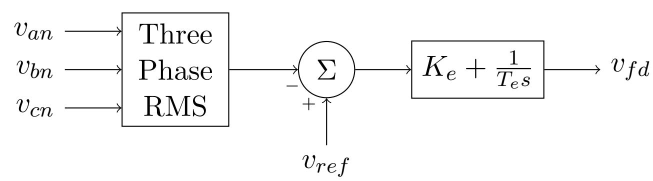

Figure 6.6: Exciter system for the independent synchronous machine

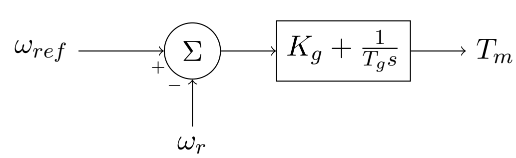

Figure 6.7: Governor system for the independent synchronous machine

Figures 6.8 and 6.9 illustrate the simulation results for the terminal voltage and current of the synchronous machine during start-up transient, respectively. The magnitudes of the dynamic phasors are included along with waveforms obtained from PSCAD/EMTDC. The results demonstrate that the dynamic phasor simulation results accurately capture the envelope of the PSCAD/EMTDC waveforms.

Table 6.1: Synchronous machine model parameters

Parameter	**Value**	**Parameter**	**Value**
Base MVA	1100 MVA		
Base voltage	18 kV		
Base frequency	60 Hz		
L_{mq}	0.91pu	L_{md}	1.66pu
R_s	0.025pu	L_{ls}	0.14pu
R_{1q}	0.00842pu	L_{1q}	0.106pu
R_{2q}	0.0081942pu	L_{2q}	0.0094199pu
R_{fd}	0.006pu	L_{fd}	0.2004pu
R_{1d}	0.0051pu	L_{1d}	0.0437pu
H	1.7 s	D	0

Table 6.2: Independent generator system parameters

Parameter	**Value**	**Parameter**	**Value**
f_0	60 Hz	K_e	25
R_1	10 Ω	T_e	10 ms
R_2	5 Ω	K_g	25
L	23 mH	T_g	10 ms

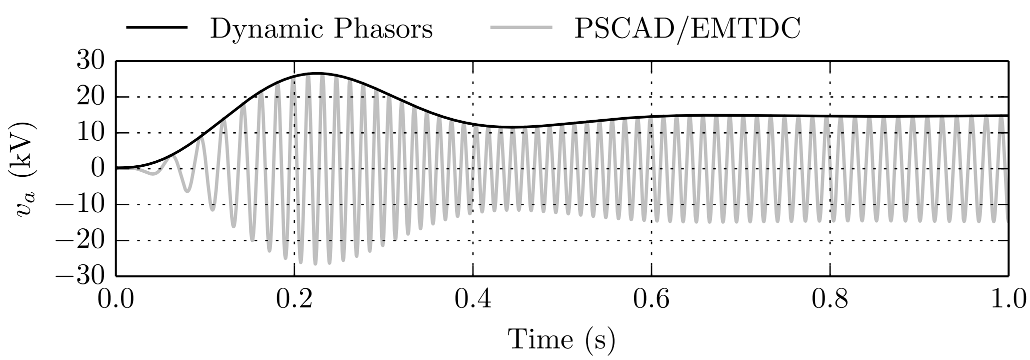

Figure 6.8: Comparison of the stator voltage during start-up transients

Figures 6.10 and 6.11 illustrate the start-up transient simulation results for the rotor frequency and electromagnetic torque of the synchronous machine, respectively. Figure 6.10 illustrates that the rotor frequency results produced by the dynamic phasor simulations are in good agreement with the PSCAD/EMTDC simulation results. Figure 6.11 illustrates that the electromagnetic torque results are in good agreement except near the peak of the initial overshoot at approximately 0.2 s. However, this error was considered negligible given the agreement between the electrical stator quantities.

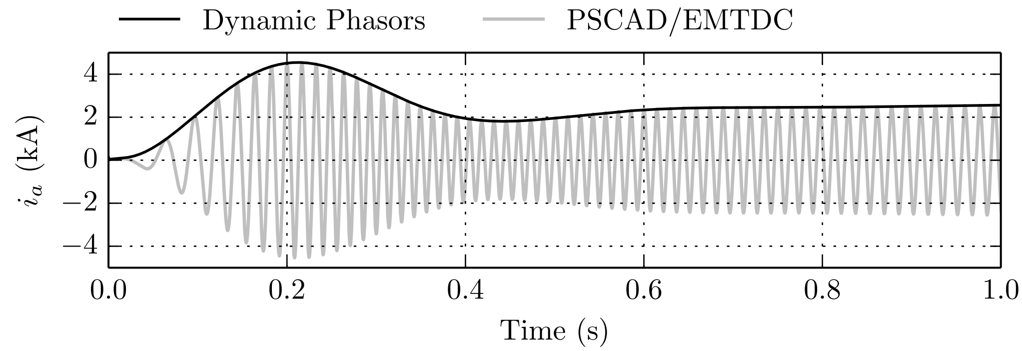

Figure 6.9: Comparison of the stator current during start-up transients

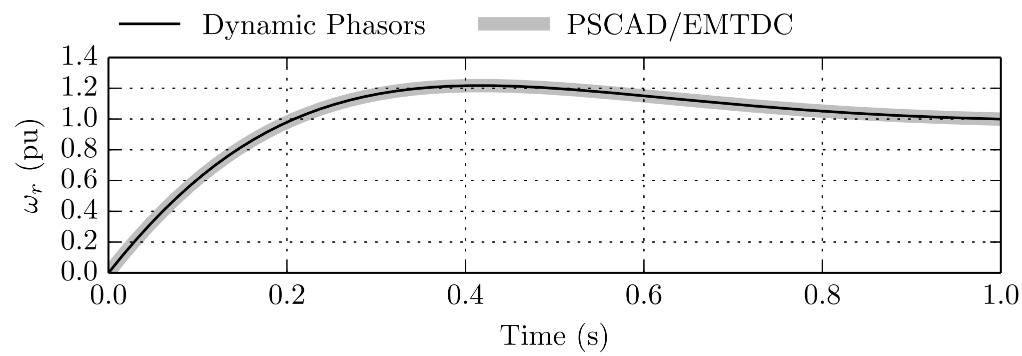

Figure 6.10: Comparison of the rotor frequency during start-up transients

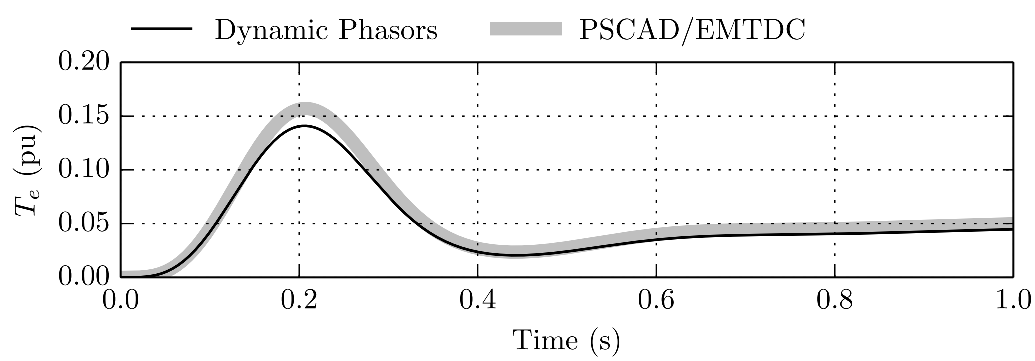

Figure 6.11: Comparison of the electromagnetic torque during start-up transients

Figures 6.12 and 6.13 illustrate the terminal voltage and current waveforms of the synchronous machine reconstructed using dynamic phasors, respectively. The simulation results demonstrate that the PSCAD/EMTDC and dynamic phasor waveforms are in good agreement. Therefore, this shows that the dynamic phasor model of the synchronous machine is capable of capturing behaviour where the electrical frequency of the system is not constant and changes according to the machine dynamics.

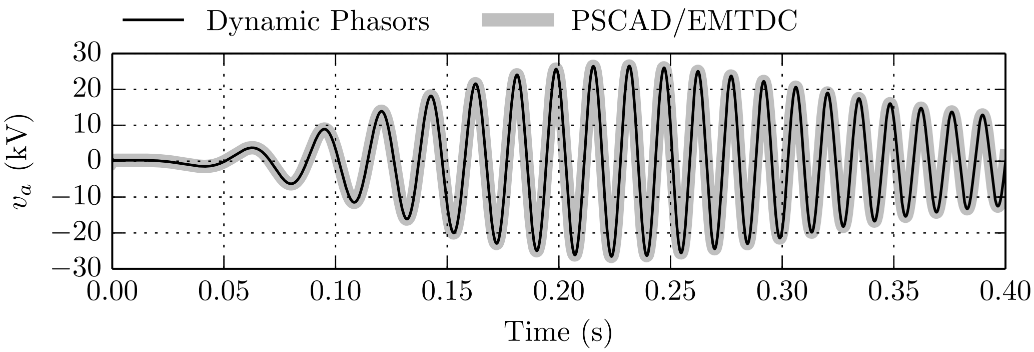

Figure 6.12: Comparison of the stator voltage waveforms during start-up transients

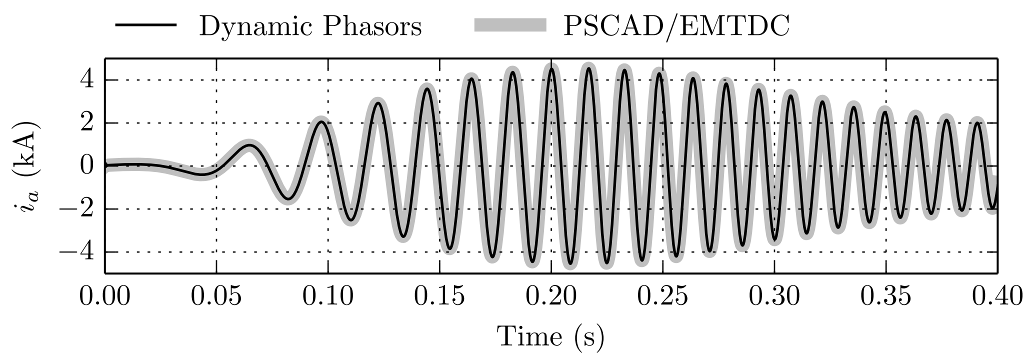

Figure 6.13: Comparison of the stator current waveforms during start-up transients

Figures 6.14 and 6.15 illustrate the simulation results for the terminal voltage and current of the synchronous machine following a balanced three phase fault, respectively. The three phase fault shown in Section 5.5 was applied to the terminals of the machine at 2 s for 0.25 s with a fault resistance of 0.01 Ω. Figure 6.14 illustrates that the terminal voltage waveforms are in good agreement except when the fault is cleared, at which point there are momentary high frequency oscillations of considerable magnitude that are not present in the PSCAD/EMTDC simulations. Figure 6.15 illustrates that the current waveforms are also in good agreement except at the point where the fault is cleared. The oscillations present in the dynamic phasor results are likely numerical and due to the sudden nature of the fault in conjunction with the integration method used to simulate the machine.

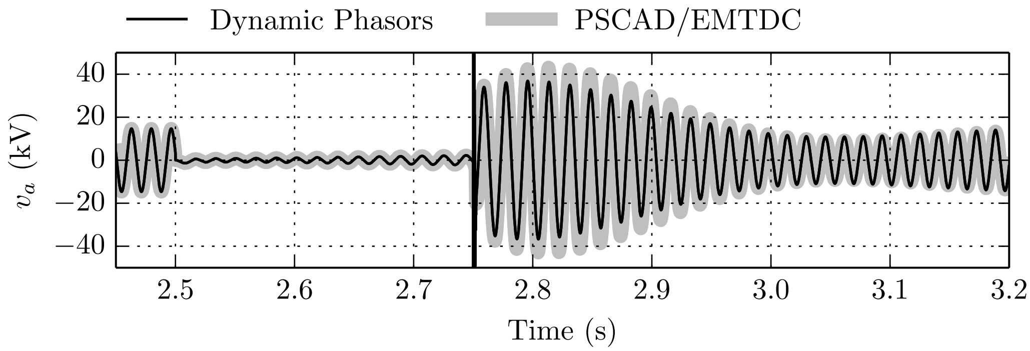

Figure 6.14: Comparison of the stator voltage waveforms following a balanced three phase fault

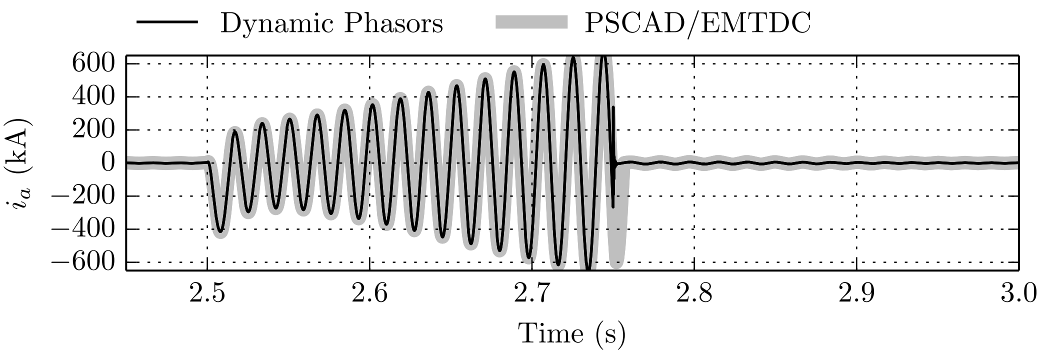

Figure 6.15: Comparison of the stator current waveforms following a balanced three phase fault

Figures 6.16 and 6.17 illustrate the simulation results for the rotor frequency and electromagnetic torque of the synchronous machine following the three phase balanced fault, respectively. Figure 6.16 illustrates that the simulation results for the rotor frequency are in good agreement. Figure 6.17 illustrates that the simulation results for the electromagnetic torque are in good agreement except at the point where the fault is cleared. This disagreement is a result of the problems noted earlier in the stator quantities.

Figures 6.18 to 6.21 illustrate the simulation results for the stator and rotor quantities of the synchronous machine following an unbalanced line-to-line fault. The line-to-line fault shown in Section 5.5 was applied to the terminals of the machine at 2 s for 0.25 s with a fault resistance of 0.01 Ω. The simulation results indicate that the dynamic phasor model does not accurately capture the transient behaviour of the machine during this fault. This behaviour is expected since the rotor was modeled in this work using only the dc component. The first and second harmonics would also be required to accurately model unbalanced faults such as the line-to-line fault used in this test.

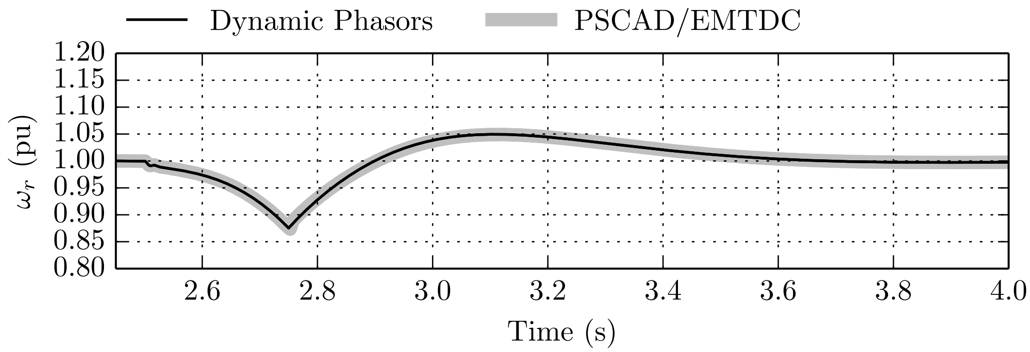

Figure 6.16: Comparison of the rotor frequency following a balanced three phase fault

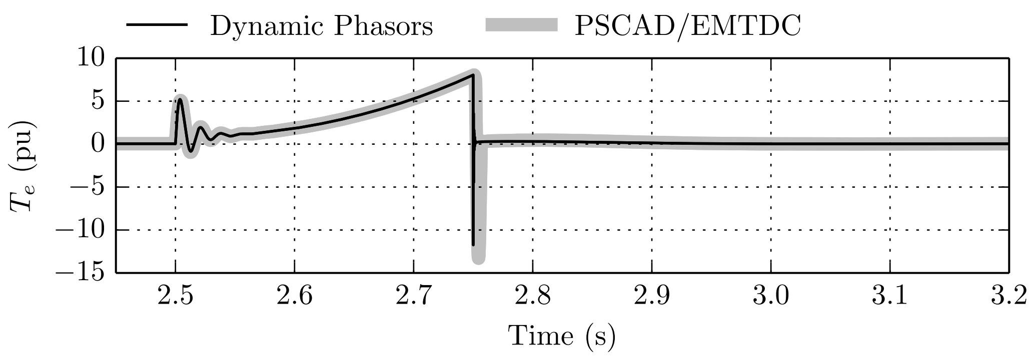

Figure 6.17: Comparison of the electromagnetic following a balanced three phase fault

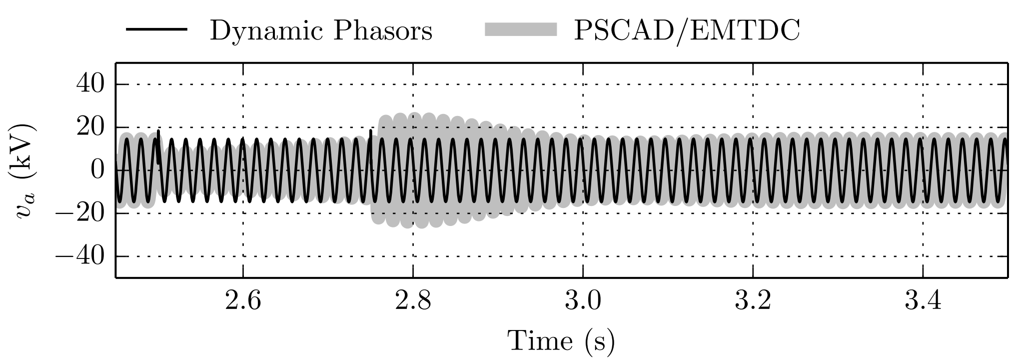

Figure 6.18: Comparison of the stator voltage waveforms following a line-to-line fault

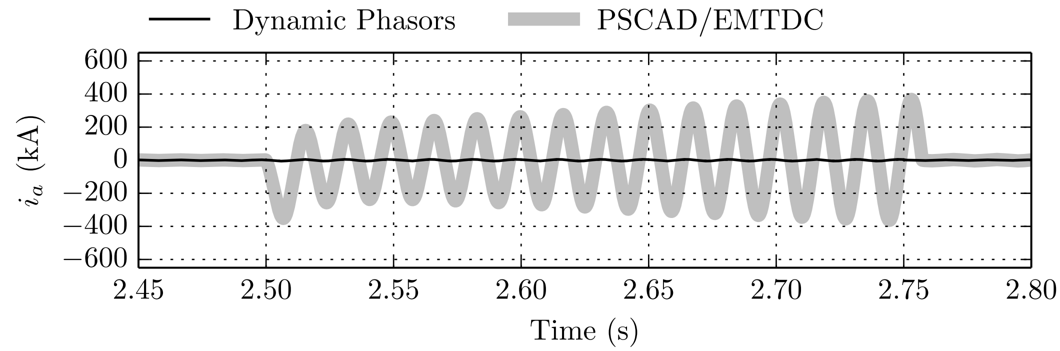

Figure 6.19: Comparison of the stator current waveforms following a line-to-line fault

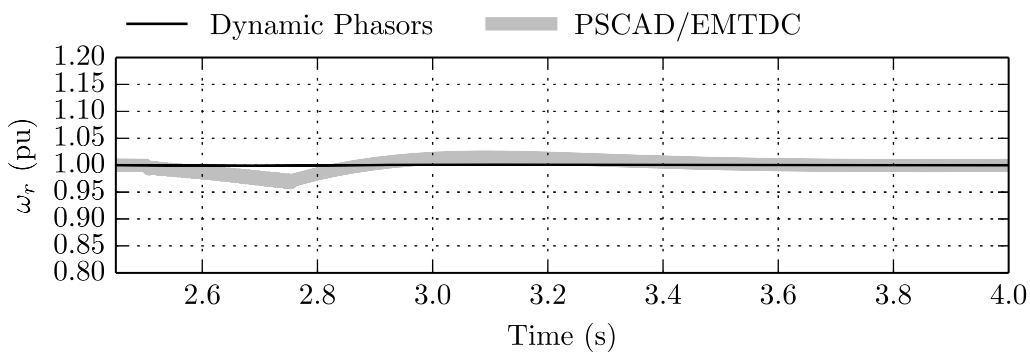

Figure 6.20: Comparison of the rotor frequency following a line-to-line fault

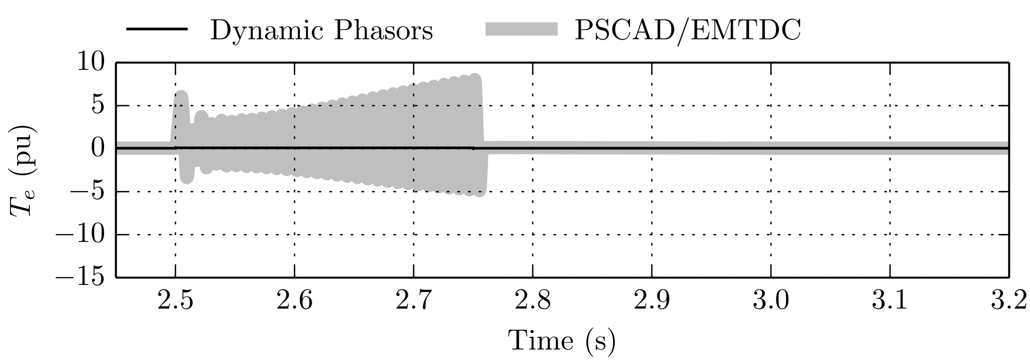

Figure 6.21: Comparison of the electromagnetic torque following a line-to-line fault

6.4.2 Single Machine Infinite Bus

Figure 6.22 illustrates the single line diagram for the second example system that will be used to demonstrate the dynamic phasor synchronous machine model [4]. The exciter and governor were modeled using the simple feedback control systems shown in Figures 6.6

and 6.7 from the previous example. The data given in Table 6.1 from the previous section was used in this section to model the synchronous machine and Table 6.3 contains the system data for this example.

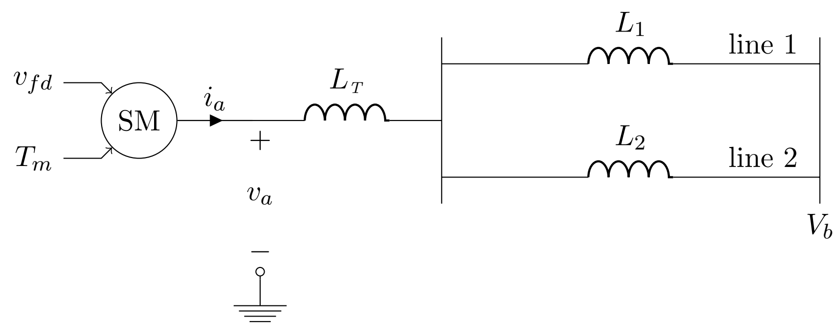

Figure 6.22: Single machine infinite bus system

Table 6.3: Single machine infinite bus system parameters

Parameter	**Value**	**Parameter**	**Value**
f_0	60 Hz	K_e	60
L_T	0.117 mH	T_e	2 ms
L_1	0.391 mH	K_g	50
L_2	0.728 mH	T_g	10 ms
V_b	17.91 kV		

Figures 6.23 and 6.24 illustrate the simulation results for the stator terminal voltage and current following a sudden loss of line 2, respectively. Figure 6.23 illustrates that the terminal voltage appears to be unchanged in both waveforms, except near the point where the line is disconnected. At this point, the dynamic phasor simulation results include the high frequency oscillations that were noted in the previous section. Figure 6.24 illustrates that the stator current waveforms are in good agreement.

Figures 6.25 and 6.26 illustrate the simulation results for the rotor frequency and electromagnetic torque following the sudden loss of line 2, respectively. Figure 6.25 illustrates that rotor frequency waveforms are in good agreement, with a small amount of error while the frequency is recovering from the loss of line 2. Figure 6.26 illustrates that the electromagnetic torque waveforms are in good agreement except near the beginning of the transient. The dynamic phasor results indicate that the high frequency oscillations noted in the terminal voltage waveform are also present in the electromagnetic torque waveform.

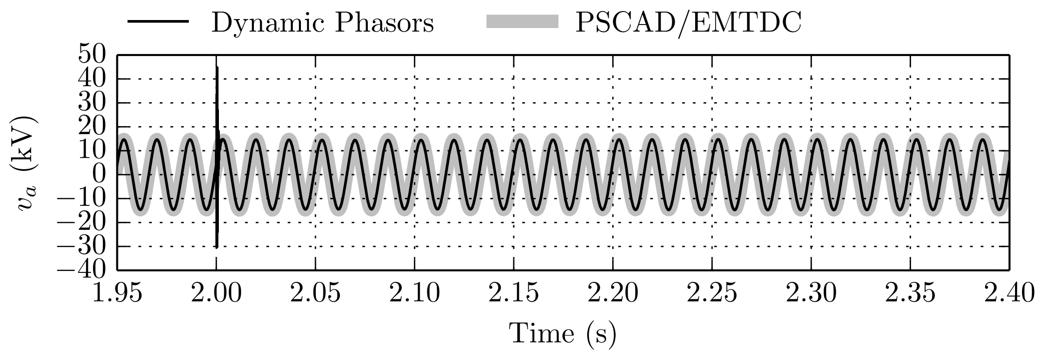

Figure 6.23: Comparison of the stator voltage waveforms following the loss of line 2

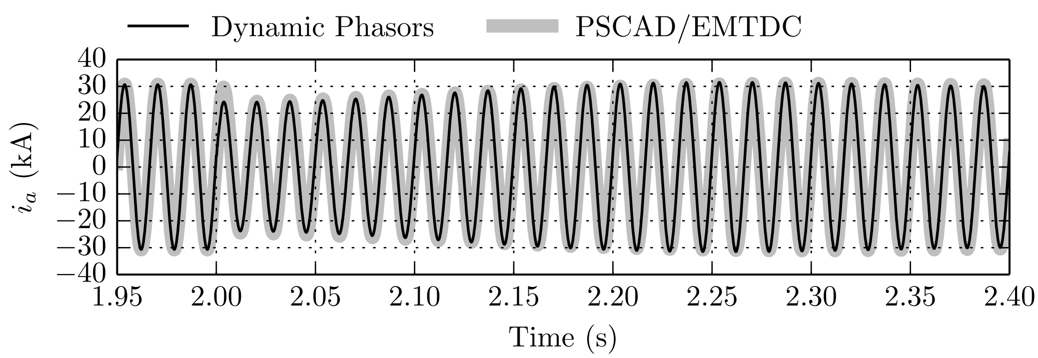

Figure 6.24: Comparison of the stator current waveforms following the loss of line 2

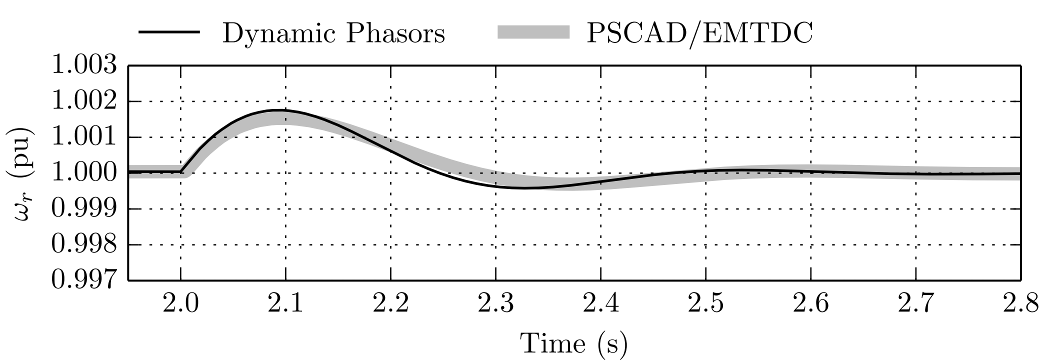

Figure 6.25: Comparison of the rotor frequency following the loss of line 2

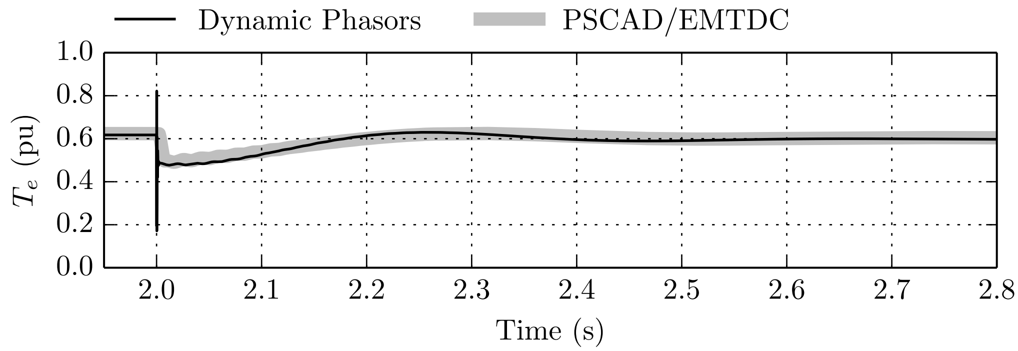

Figure 6.26: Comparison of the electromagnetic torque following the loss of line 2

6.5 Summary

This chapter presented a dynamic phasor-based synchronous machine model for use in the general purpose simulation method discussed in Chapter 3. The dynamic phasor model is based on a complete synchronous machine, including both electrical and mechanical system dynamics. The model presented in this chapter uses Park's transformation to refer all stator variables to the rotor's frame of reference. A dynamic phasor form of Park's transformation and its inverse are presented in this chapter. This approach differs from the methods presented in literature, which generally use space vector formulations to model the synchronous machine.

The continuous dynamic phasor model presented in this chapter is then transformed to a discrete Norton equivalent using the time step delay technique used in programs such as PSCAD/EMTDC. Comparisons of simulations results for two test systems were included in this chapter. The simulation results demonstrate that the dynamic phasor simulations accurately capture the dynamic behaviour of the synchronous machine. The simulation results also demonstrate the limitations of the model, which were based on the limitations of the numerical method used to integrate the stator and rotor differential equations.

Chapter 7

Conclusions, Contributions, and Future Directions

The objective of this thesis was to develop a new general purpose simulation method based on dynamic phasors and conventional power system simulation techniques. Chapter 1 demonstrated that there has been significant research into the application of dynamic phasors in areas such as power electronics, machines, and hybrid modeling. Previous research has demonstrated that dynamic phasors may be used in applications such as improved system modeling and controller design. Chapter 1 also demonstrated that there is a gap in current dynamic phasors research. Previous work has been primarily focused on modeling of specific subsystems and low frequency dynamics. The method developed in this thesis is used to fill this gap through general purpose simulation techniques and provisions for including higher order harmonics.

Chapter 3 presented the foundation for the dynamic phasor-based general purpose simulation method developed in this work. The in-place circuit averaging technique is used to transform circuit models into coupled harmonic equivalent circuits. Simulations of the harmonic equivalents may then be carried out using conventional power system simulation techniques. This method was then extended in Chapters 4 to 6, which present the framework for including more complex subsystems that are essential for power system simulation.

7.1 Contributions and Conclusions

The primary contribution of this thesis is a new general purpose simulation method that addresses the gaps identified in research. Comparisons of dynamic phasor simulation results with PSCAD/EMTDC results throughout this work demonstrate that the general purpose simulation method accurately captures the dynamic behaviour of a wide vareity of components, such as controllers and LCCs. The results also demonstrate that the simulation method developed in this work is capable of modeling both low and high frequency components. Therefore, this method satisfies the original thesis objective of developing a general purpose simulator that is not limited to low frequency simulations.

This thesis makes the following additional contributions to dynamic phasor modeling and simulation research:

1. A review of previous research conducted on dynamic phasor based modeling and simlation.

   The literature review in Chapter 1 demonstrated that there has been significant research conducted in the area of generalized state space averaging and dynamic phasors. This review revealed that dynamic phasors are valuable in obtaining reduced order models of a wide variety of power electronic converters and systems. More importantly, this review revealed that dynamic phasor-based modeling is a powerful tool for identifying the effects of harmonics and system imbalance on components such as machines and converters. Therefore, dynamic phasors offer a number of benefits for power system analysis beyond obtaining average value models of power electronic converters.

2. Development of discrete equivalent models for simple components based on the exponential integrator method.

   Section 3.1 demonstrated that the dynamic phasor operator modifies the inductor and capacitor such that their continuous dynamics include exponential behaviour. Therefore, the exponential method discussed in Section 2.3 was used to obtain discrete dynamic phasor equivalents of the capacitor and inductor. The implication of this contribution is that the capacitor and inductor are more accurately represented using this method than the trapezoidal method.

3. Development of a generalized procedure for deriving discrete dynamic phasor equivalents of composite component and voltage source models.

   Composite components are important for the generalized dynamic phasor based simulation method developed in this work as they reduce the computational burden of simulations. The generalized procedure developed for passive composite components in Section 3.2 is based on a general set of time-domain state space equations, which is then systematically converted to a single discrete dynamic phasor Norton equivalent. This method was then extended to voltage sources with dynamic impedances in Section 3.3. The implication of this contribution is that it reduces program complexity and encourages development of composite models for simulation.

4. Development of a new formal method for modeling variable frequency systems using dynamic phasors.

   Previous research has demonstrated that it is possible to model variable frequency systems using dynamic phasors. However, the methods used are of limited use in general purpose simulation as they require special insight and approximations for each individual subsystem. The method developed in Section 3.3 generalizes the approaches used in previous research for modeling variable frequency systems that does not require modification to the standard dynamic phasor formulation. This method is compatible with any variable frequency system and may be used in the general purpose simulation method developed in this work.

5. Development of a discrete dynamic phasor equivalent for a LCC.

   Comparisons of the dynamic phasor LCC model with PSCAD/EMTDC results in Chapter 5 demonstrate that the model developed in this work accurately captures the dynamic behaviour of LCCs. In particular, the simulation results demonstrate that the dynamic phasor model accurately models the LCC for both low and higher order harmonics. Therefore, this contribution demonstrates that accurate simulation of power electronic systems is possible with the general purpose simulation method developed in this work. The implication of this contribution is that simulation of larger system models that include power electronics, such as the CIGRE benchmark systems, are possible using the method developed in this work.

6. Development of a discrete dynamic phasor equivalent of the synchronous machine.

   Comparisons of the dynamic phasor synchronous machine model with simulation results obtained using PSCAD/EMTDC in Chapter 6 demonstrate that the model developed in this work accurately captures the dynamic behaviour of synchronous machines. In particular, the simulation results demonstrate that the dynamic phasor model developed in this work is capable of accurately simulating the synchronous machine under variable frequency conditions. Therefore, this contribution demonstrates that accurate simulation of electric machines that include mechanical subsystem dynamics is possible with the general purpose simulation method developed in this work. The implication of this contribution is that simulation of phenomena such as SSR is possible using the method developed in this work.

7. Development of a dynamic phasor form of Park's transformation.

   The approach used in Chapter 6 to model synchronous machines is based on conventional methods, which employ Park's transformation to transfer stator quantities to the rotor's frame of reference. Therefore, a dynamic phasor form of Park's transformation was developed in this work using the variable frequency method developed in Section 3.3. The implication of this contribution is that other reference frame transformations may be carried out using dynamic phasors by applying similar methods.

7.2 Limitations and Future Work

This thesis laid the foundation for general purpose dynamic phasor-based simulation of power systems through the development of a systematic simulation method and a set of commonly used models. However, the limitations of the models and methods developed in this work were also identified, which along with development of new system models, provide the foundation for significant future work in this area. Future work in this area includes:

1. Chapter 3 identified that the computational burden of the general purpose simulation method developed in this work increases as the number of harmonics included in simulations increases. This property limits the number of harmonics that may be realistically included in simulations. However, Chapter 3 also identified that computational methods could be applied to the general purpose simulation method to improve efficiency and increase simulation speed. Additional research is necessary to investigate how more advanced computational methods, such as parallel processing, may be applied to the general purpose simulation method.

2. The LCC model developed in Chapter 5 requires the ac side of the converter to be balanced. The simulation results for unbalanced ac faults demonstrated that when this condition is not satisfied, the dynamic phasor model does not accurately capture the dynamic behaviour of the LCC. The balanced ac system assumption is important for both the switching functions and the PLL to operate correctly. Future research must be conducted in this area to improve the LCC and PLL models and enable them to produce accurate results when the ac system is unbalanced.

3. The synchronous machine model developed in Chapter 6 is in theory capable of handling unbalanced ac system conditions. However, the simulation results demonstrated that due to numerical limitations, the synchronous machine model is unable to operate correctly when the ac system is unbalanced. Furthermore, the simulation results also demonstrated that the synchronous machine produces uncharacteristic high frequency numerical oscillations during sudden faults and ac system events. Future research must be conducted in this area to improve the discrete model of the synchronous machine and enable it to produce accurate results for unbalanced ac systems and faults.

   The synchronous machine model developed in Chapter 6 also does not take into account more complex behaviour such as multi-mass rotor models [1] and magnetic saturation [4]. Additional research is necessary in this area to enhance the synchronous machine model and take into account advanced components such as saturation.

4. Power systems include many additional components whose models were not addressed in this work. Components such as transmission lines and transformers include complicated behaviour, such as frequency-dependence and magnetic saturation, that pose challenging research questions. Significant future work must be conducted to expand the set of models that may be included in the simulation method developed in this work.

References

[1] N. Watson and J. Arrillaga, *Power Systems Electromagnetic Transients Simulation*, 1st ed., ser. IET Power and Energy Series. The Institution of Engineering and Technology, 2003, vol. 39.

[2] T. H. Demiray, "Simulation of power system dynamics using dynamic phasor models," Ph.D. dissertation, Swiss Federal Institute of Technology, 2008.

[3] C. Karawita, "HVDC interaction studies using small signal stability assessment," Ph.D. dissertation, University of Manitoba, 2009.

[4] P. Kundur, *Power System Stability and Control*, ser. EPRI Power System Engineering Series. McGraw Hill, Inc., 1994.

[5] R. C. Dorf and J. A. Svoboda, *Introduction to Electric Circuits*, 7th ed. John Wiley & Sons, Inc., 2006.

[6] V. Venkatasubramanian, H. Schattler, and J. Zaborszky, "Fast time-varying phasor analysis in the balanced three-phase large electric power system," *IEEE Transactions on Automatic Control*, vol. 40, no. 11, pp. 1975–1982, November 1995.

[7] S. Henschel, "Analysis of electromagnetic and electromechanical power system transients with dynamic phasors," Ph.D. dissertation, University of British Columbia, February 1999.

[8] S. R. Sanders, J. M. Noworolski, X. Z. Liu, and G. C. Verghese, "Generalized averaging method for power conversion circuits," *IEEE Transactions on Power Electronics*, vol. 6, no. 2, pp. 251–259, April 1991.

[9] J. Mahdavi, A. Emaadi, M. Bellar, and M. Ehsani, "Analysis of power electronic converters using the generalized state-space averaging approach," *IEEE Transactions on Circuits and Systems - I: Fundamental Theory and Applications*, vol. 44, no. 8, pp. 767–770, August 1997.

[10] V. A. Caliskan, G. C. Verghese, and A. M. Stankovic, "Multifrequency averaging of dc/dc converters," *IEEE Transactions on Power Electronics*, vol. 14, no. 1, pp. 124–133, January 1999.

[11] A. Emadi, "Modeling and analysis of multiconverter dc power electronic systems using the generalized state-space averaging method," *IEEE Transactions on Industrial Electronics*, vol. 51, no. 3, pp. 661–668, June 2004.

[12] ——, "Modeling of power electronic loads in ac distribution systems using the generalized state-space averaging method," *IEEE Transactions on Industrial Electronics*, vol. 51, no. 5, pp. 992–1000, October 2004.

[13] Z. Ye, P. K. Jain, and P. C. Sen, "Modeling of high frequency resonant inverter system in phasor domain for fast simulation and control design," in *Proc. 2008 IEEE Power Electronics Specialists Conference*, pp. 2090–2096.

[14] X. Guo, Z. Lu, B. Wang, X. Sun, L. Wang, and J. M. Guerrero, "Dynamic phasors-based modeling and stability analysis of droop-controlled inverters for microgrid applications," *IEEE Transactions on Smart Grid*, vol. 5, no. 6, pp. 2980–2987, November 2014.

[15] P. Mattavelli, G. C. Verghese, and A. M. Stankovic, "Phasor dynamics of thyristor-controlled series capacitor systems," *IEEE Transactions on Power Systems*, vol. 12, no. 3, pp. 1259–1267, August 1997.

[16] P. Mattavelli, A. M. Stankovic, and G. C. Verghese, "SSR analysis with dynamic phasor model of thyristor-controlled series capacitor," *IEEE Transactions on Power Systems*, vol. 14, no. 1, pp. 200–208, February 1999.

[17] A. Stankovic, P. Mattavelli, V. Caliskan, and G. Verghese, “Modeling and analysis of FACTS devices with dynamic phasors,” in *Proc. 2000 IEEE Power Engineering Society Winter Meeting*, vol. 2, pp. 1440–1446.

[18] P. Stefanov and A. Stankovic, “Modeling of UPFC operation under unbalanced conditions with dynamic phasors,” *IEEE Transactions on Power Systems*, vol. 17, no. 2, pp. 395–203, May 2002.

[19] Q. Qi, C. Yu, C. K. Wai, and Y. Ni, “Modeling and simulation of a STATCOM system based on 3-level NPC inverter using dynamic phasors,” in *Proc. 2004 IEEE Power Engineering Society General Meeting*, vol. 2, pp. 1559–1564.

[20] S. Gomes, N. Martins, and A. Stankovic, “Improved controller design using new dynamic phasor models of SVC’s suitable for high frequency analysis,” in *Proc. 2006 IEEE PES Transmission and Distribution Conference and Exhibition*, pp. 1436–1444.

[21] A. Yazdani and R. Iravani, “A generalized state-space averaged model of the three-level NPC converter for systematical dc-voltage-balancer and current-controller design,” *IEEE Transactions on Power Delivery*, vol. 20, no. 2, pp. 1105–1114, April 2005.

[22] H. Zhu, Z. Cai, H. Liu, Q. Qi, and Y. Ni, “Hybrid-model transient stability simulation using dynamic phasors based HVDC system model,” *Electric Power Systems Research*, vol. 76, no. 6–7, pp. 582–591, April 2006.

[23] M. Hannan, A. Mohamed, A. Hussain, and M. Al-Dabbagh, “Power quality analysis of STATCOM using dynamic phasor modeling,” *Electric Power Systems Research*, vol. 79, no. 6, pp. 993–999, June 2009.

[24] E. Zhijun, D. Fang, F. Chan, and S. Yuan, “Hybrid simulation of power systems with SVC dynamic phasor model,” *International Journal of Electrical Power and Energy Systems*, vol. 31, no. 5, pp. 175–180, June 2009.

[25] F. C. Jusan, S. Gomes, and G. N. Taranto, "SSR results obtained with a dynamic phasor model of SVC using modal analysis," *International Journal of Electrical Power and Energy Systems*, vol. 32, no. 6, pp. 571–582, July 2010.

[26] A. Stankovic, B. Lesieutre, and T. Aydin, "Modeling and analysis of single-phase induction machines with dynamic phasors," *IEEE Transactions on Power Systems*, vol. 14, no. 1, pp. 9–14, February 1999.

[27] A. M. Stankovic and T. Aydin, "Analysis of asymmetrical faults in power systems using dynamic phasors," *IEEE Transactions on Power Systems*, vol. 15, no. 3, pp. 1062–1068, August 2000.

[28] A. M. Stankovic, S. R. Sanders, and T. Aydin, "Dynamic phasors in modeling and analysis of unbalanced polyphase machines," *IEEE Transactions on Energy Conversion*, vol. 17, no. 1, pp. 107–113, March 2002.

[29] E. Delaleau and A. Stankovic, "Modeling and simulation of the induction motor with position-dependent load torque," in *Proc. 2003 IEEE Conference on Decision and Control*, vol. 6, pp. 6212–6217.

[30] A. Coronado-Mendoza and J. A. Dominguez-Navarro, "Dynamic phasors modeling of inverter fed induction generator," *Electric Power Systems Research*, vol. 107, pp. 68–76, February 2014.

[31] Y. Shujun, B. Mingran, H. Ya'nan, H. Minxiao, H. Junxian, and W. Lei, "Modeling for VSC-HVDC electromechanical transient based on dynamic phasor method," in *Proc. 2013 IET Renewable Power Generation Conference*, pp. 1–4.

[32] C. Liu, A. Bose, and P. Tian, "Modeling and analysis of HVDC converter by three-phase dynamic phasor," *IEEE Transactions on Power Delivery*, vol. 29, no. 1, pp. 3–12, February 2014.

[33] R. Shintaku and K. Strunz, "Branch companion modeling for diverse simulation of electromagnetic and electromechanical transients," *Electric Power Systems Research*, vol. 77, no. 11, pp. 1501–1505, September 2007.

[34] R. L. Burden and J. D. Faires, *Numerical Analysis*, 7th ed. Wadsworth Group, 2001.

[35] H. Saadat, *Power System Analysis*, 3rd ed. PSA Publishing, 2010.

[36] H. Dommel, “Digital computer solution of electromagnetic transients in single-and multiphase networks,” *IEEE Transactions on Power Apparatus and Systems*, vol. PAS-88, no. 4, pp. 388–399, April 1969.

[37] N. Watson and G. Irwin, “Electromagnetic transient simulation of power systems using root-matching techniques,” *IEE Proceedings - Generation, Transmission and Distribution*, vol. 145, no. 5, pp. 481–486, September 1998.

[38] A. H. Al-Mohy and N. J. Higham, “Computing the action of the matrix exponential with an application to exponential integrators,” *SIAM Journal on Scientific Computing*, vol. 33, no. 2, pp. 488–511, 2011.

[39] K. Ogata, *Modern Control Engineering*, 5th ed. Pearson Education, Inc., 2010.

[40] N. R. Watson and G. D. Irwin, “Accurate and stable electromagnetic transient simulation using root-matching techniques,” *International Journal of Electrical Power and Energy Systems*, vol. 21, no. 3, pp. 225–234, March 1999.

[41] D. Maksimovic, A. M. Stankovic, V. J. Thottuvelil, and G. C. Verghese, “Modeling and simulation of power electronic converters,” *Proceedings of the IEEE*, vol. 89, no. 6, pp. 898–912, June 2001.

[42] J. M. Noworolski and S. R. Sanders, “Generalized in-place circuit averaging,” in *Proc. 1991 Applied Power Electronics Conference and Exposition*, pp. 445–451.

[43] P. Krause, O. Wasynczuk, S. Sudhoff, and S. Pekarek, *Analysis of Electric Machinery and Drive Systems*, 3rd ed., ser. IEEE Press Series on Power Engineering. John Wiley & Sons, Inc., 2013.

[44] N. Mohan, T. M. Undeland, and W. P. Robbins, *Power electronics: converters, applications, and design*, 3rd ed. John Wiley & Sons, Inc., 2003.

[45] *PSCAD/EMTDC User's Manual*, Manitoba HVDC Research Center, Winnipeg, MB, Canada, 2010.

[46] J. G. Kassakian, M. F. Schlecht, and G. C. Verghese, *Principles of Power Electronics*. Addison-Wesley Publishing Company, Inc., 1991.

[47] A. Gole and V. Sood, "A static compensator model for use with electromagnetic transients simulation programs," *IEEE Transactions on Power Delivery*, vol. 5, no. 3, pp. 1398–1407, July 1990.

[48] M. Daryabak, S. Filizadeh, J. Jatskevich, A. Davoudi, M. Saeedifard, V. Sood, J. Martinez, D. Aliprantis, J. Cano, and A. Mehrizi-Sani, "Modeling of LCC-HVDC systems using dynamic phasors," *IEEE Transactions on Power Delivery*, vol. 29, no. 4, pp. 1989 – 1998, August 2014.

[49] A. Araujo, H. Dommel, and J. Marti, "Simultaneous solution of power and control system equations," *IEEE Transactions on Power Systems*, vol. 8, no. 4, pp. 1483–1489, November 1993.

[50] W. Gang, L. Zhikeng, L. Haifeng, L. Xiaolin, and F. Chuang, "Modeling of the HVDC convertor using dynamic phasor under asymmetric faults in the ac system," in *Proc. 2009 International Conference on Sustainable Power Generation and Supply*, pp. 1–5.

[51] H. Sun, X. Yang, X. Wang, and J. Sun, "Improved dynamic phasor model of HVDC system for subsynchronous oscillation study," in *Proc. 2011 International Conference on Electric Utility Deregulation and Restructuring and Power Technologies*, pp. 485–489.

[52] L. Gyugyi and B. Pelly, *Static Power Frequency Changers*. John Wiley & Sons, Inc., 1976.

[53] S. Chiniforoosh, J. Jatskevich, A. Yazdani, V. Sood, V. Dinavahi, J. Martinez, and A. Ramirez, "Definitions and applications of dynamic average models for analysis of power systems," *IEEE Transactions on Power Delivery*, vol. 25, no. 4, pp. 2655–2669, October 2010.

[54] R. Park, "Two-reaction theory of synchronous machines generalized method of analysis - part I," *Transactions of the American Institute of Electrical Engineers*, vol. 48, no. 3, pp. 716–727, July 1929.